Università degli Studi di Napoli Federico II

Dottorato di Ricerca
in Ingegneria Strutturale e Rischio Sismico

in co-tutorship with

Université Paris-Saclay

Ecole Doctorale
Sciences mécaniques et énergétiques, matériaux et géosciences

Unité de recherche Lab. Quartz, ISAE Supméca

THESIS FOR THE DEGREE OF DOCTOR OF PHILOSOPHY

Hysteretic Responses of Connections in Timber Structures: Classification, Phenomenological Modeling and Identification

by
AGNESE SPEDICATO

Advisors: Prof. Luciano Rosati (Università degli Studi di Napoli)
Prof. Jean-Luc Dion (ISAE Supméca)

Tutors: Nicolò Vaiana (Università degli studi di Napoli)
Stefania Lo Feudo (ISAE Supméca)

PhD Thesis

université PARIS-SACLAY

isae supméca

Université Paris-Saclay

Ecole Doctorale n.579
Sciences mécaniques et énergétiques, matériaux et géosciences
Unité de recherche Lab. Quartz, ISAE Supméca

et préparée en cotutelle avec

Università degli Studi di Napoli Federico II
Dottorato di Ricerca
in Ingegneria Strutturale e Rischio Sismico

THÈSE DE DOCTORAT

Hysteretic Responses of Connections in Timber Structures: Classification, Phenomenological Modeling and Identification

Présentée et soutenue publiquement le __ Avril 2025, par

Agnese SPEDICATO

DIRECTEURS: Prof. Jean-Luc DION (ISAE Supméca)
Prof. Luciano ROSATI (Università degli Studi di Napoli)

TUTORS: Stefania LO FEUDO (ISAE Supméca)
Nicolò VAIANA (Università degli studi di Napoli)

RAPPORTEURS:

Emmanuel FOLTETE	Professeur des Universités	Université Bourgogne Franche-Comté
Antonio MADEO	Professore Associato	Università della Calabria

MEMBRES DU JURY:

_____
_____
_____
_____







La borsa di dottorato è stata cofinanziata con risorse del
Programma Operativo Nazionale Ricerca e Innovazione 2014-2020, risorse FSE REACT-EU
Azione IV.4 “Dottorati e contratti di ricerca su tematiche dell’innovazione”
e Azione IV.5 “Dottorati su tematiche Green”

Hysteretic Responses of Connections in Timber Structures: Classification, Phenomenological Modeling and Identification

Ph.D. Thesis presented
in partial fulfillment of the requirements of the Degree of Doctor of Philosophy
in Ingegneria Strutturale, Geotecnica e Rischio Sismico
at Università degli Studi di Napoli Federico II

and

in partial fulfillment of the requirements of the Degree of Doctor of Philosophy
in Sciences mécaniques et énergétiques, matériaux et géosciences
at Université Paris-Saclay
by

Agnese Spedicato

April 2025

Approved as to style and content by

_____

Prof. Luciano Rosati, Advisor

_____

Prof. Jean-Luc Dion, Co-advisor

_____

Nicolò Vaiana and Stefania Lo Feudo, Tutors

Università degli Studi di Napoli Federico II

Ph.D. Program in Ingegneria Strutturale, Geotecnica e Rischio Sismico

XXXVII cycle - Chairman: Prof. Iunio Iervolino



www.dist.unina.it/dottorati-di-ricerca/dottorati

Université Paris - Saclay

Ph.D. Program in Sciences mécaniques et énergétiques, matériaux et géosciences (ED 579)

Chairman: Benoit Florina

Unité de recherche Lab. Quartz, ISAE Supméca



www.en.isae-supmeca.fr/research/research-at-supmeca-2/

Candidate's declaration

I hereby declare that this thesis submitted to obtain the academic degree of Philosophiæ Doctor (Ph.D.) in Ingegneria Strutturale, Geotecnica e Rischio Sismico is my own unaided work, that I have not used other than the sources indicated, and that all direct and indirect sources are acknowledged as references.

Parts of this dissertation have been published in international journals and/or conference articles (see list of the author's publications at the end of the thesis).

Napoli, February 3, 2025



Agnese Spedicato

Abstract

Timber structures are gaining widespread recognition as sustainable and innovative solutions for modern construction. Their environmental benefits, excellent mechanical properties, and versatility make them ideal for various applications. However, the dynamic performance of timber elements, particularly under seismic loads, remains a key challenge due to the nonlinear behavior of connections, which strongly influences the structural response.

This research focuses on understanding and simulating the dynamic behavior of timber panels and their metallic connections, such as hold-downs and angle brackets, under seismic excitation. These connections govern critical parameters like stiffness, ductility, and energy dissipation, making their accurate representation essential for reliable structural analysis. Despite existing models, the complexity of nonlinear phenomena, such as pinching, degradation, and asymmetry in hysteresis loops, motivates further research to improve accuracy and applicability.

The original contributions of this thesis include: (i) a detailed calibration of the Vaiana-Rosati hysteresis model (VRM) to experimental data, enabling the accurate simulation; (ii) the application of optimization techniques, such as genetic algorithms, to systematically identify model parameters; (iii) a comprehensive simulation of the dynamic response of a Cross-Laminated Timber (CLT) panel under vertical and horizontal loads, capturing its three degrees of freedom (vertical and horizontal displacement, and rigid rotation).

This work bridges the gap between experimental observations and advanced numerical modeling of timber structures in seismic areas. The findings provide actionable insights for improving design and analysis methodologies, ultimately enhancing the performance and safety of timber buildings in earthquake-prone regions.

Keywords: Timber, Connections, Hysteresis, Optimization, Nonlinear dynamics

Resumé en français

Les structures en bois sont de plus en plus reconnues comme des solutions durables et innovantes pour la construction moderne. Leurs avantages environnementaux, leurs excellentes propriétés mécaniques et leur polyvalence les rendent idéales pour diverses applications. Cependant, les performances dynamiques des éléments en bois, en particulier sous des charges sismiques, restent un défi majeur en raison du comportement non linéaire des connexions, qui influence fortement la réponse structurelle.

Cette recherche se concentre sur l'analyse et la simulation du comportement dynamique des panneaux en bois et de leurs connexions métalliques, telles que les hold-downs et les équerres, soumis à des excitations sismiques. Ces connexions déterminent des paramètres essentiels tels que la rigidité, la ductilité et la dissipation d'énergie, rendant leur représentation précise indispensable pour une analyse structurelle fiable. Malgré les modèles existants, la complexité des phénomènes non linéaires, tels que le pinching, la dégradation et l'asymétrie dans les boucles d'hystérésis, justifie des recherches supplémentaires pour améliorer la précision et l'applicabilité.

Les contributions originales de cette thèse incluent : (i) une calibration détaillée du modèle d'hystérésis Vaiana-Rosati (VRM) à partir de données expérimentales, permettant une simulation précise du comportement non linéaire des assemblages des structures en bois ; (ii) l'application de techniques d'optimisation, telles que les algorithmes génétiques, pour identifier systématiquement les paramètres du modèle ; (iii) une simulation complète de la réponse dynamique d'un panneau en bois lamellé-croisé (CLT) soumis à des charges verticales et horizontales, prenant en compte ses trois degrés de liberté (déplacement vertical et horizontal et rigide rotation).

Ce travail comble le fossé entre les observations expérimentales et la modélisation numérique avancée des structures en bois dans les zones sismiques. Les résultats fournissent des recommandations utiles pour améliorer les méthodes de conception et d'analyse, renforçant la sécurité et les performances des bâtiments en bois dans les régions sujettes aux tremblements de terre.

Keywords : Bois, Assemblages, Hystérésis, Optimisation, Dynamique non linéaire

Sintesi in lingua italiana

Le strutture in legno stanno ottenendo un ampio riconoscimento come soluzioni sostenibili e innovative per l'edilizia moderna. I vantaggi ambientali, le eccellenti proprietà meccaniche e la versatilità le rendono ideali per numerose applicazioni. Tuttavia, il comportamento dinamico degli edifici in legno, in particolare sotto carichi sismici, rimane una sfida chiave a causa della natura non lineare dei collegamenti, che influisce in modo significativo sulla risposta strutturale.

Questa ricerca si concentra sullo studio e la simulazione del comportamento dinamico di pannelli in legno e dei loro collegamenti metallici, come hold-downs e angolari, sottoposti ad azioni sismiche. Tali collegamenti determinano parametri fondamentali come rigidezza, duttilità e dissipazione di energia, rendendo necessaria una rappresentazione accurata per un'analisi strutturale affidabile. Nonostante i modelli esistenti, la complessità dei fenomeni non lineari, come pinching, degradazione e asimmetria nei cicli isteretici, motiva ulteriori ricerche per migliorare precisione e applicabilità.

I contributi originali di questa tesi includono: (i) una calibrazione dettagliata del modello isteretico Vaiana-Rosati (VRM) su dati sperimentali, per simulare accuratamente il comportamento non lineare delle strutture in legno; (ii) l'applicazione di tecniche di ottimizzazione, come algoritmi genetici, per identificare sistematicamente i parametri del modello; (iii) una simulazione completa della risposta dinamica di un pannello in Cross-Laminated Timber (CLT) sottoposto a carichi verticali e orizzontali, considerando i suoi tre gradi di libertà (spostamento verticale e orizzontale e rotazione rigida).

Questo lavoro colma il divario tra osservazioni sperimentali e modellazione numerica avanzata delle strutture in legno in aree sismiche. I risultati forniscono indicazioni utili per migliorare i metodi di progettazione e analisi, aumentando la sicurezza e le prestazioni degli edifici in legno in zone a rischio sismico.

Parole chiave: Legno, Connessioni, Isteresi, Ottimizzazione, Dinamica non lineare

Contents

Abstract i
Resumé en français ii
Sintesi in lingua italiana iii
Acknowledgements vii
List of Acronyms ix
List of Figures xvii
List of Tables xx
List of Symbols xxii

1 Introduction **1**

2 Timber Structures in Seismic Areas **5**
2.1 Summary of Chapter 2 5
2.2 Timber as Building Material 5
2.3 Typologies of Timber Structures 7
2.4 Typologies of Timber Connections 9
2.4.1 Experimental behavior of timber joints 12
2.5 Conclusion of Chapter 2 42

3 The Vaiana-Rosati Hysteretic Model **43**
3.1 Summary of Chapter 3 43
3.2 Introduction 44
3.3 The Analytical Formulation of the Vaiana-Rosati Model 47
3.3.1 VRM: reformulated version (VRM+A) 47

3.4 The Differential Reformulation of the Vaiana-Rosati Model (VRM+D) 56
3.5 Calibration Methods and Parameter Identifications 61
3.5.1 Sensitivity Analysis 62
3.5.2 Parameter Identification 63
3.5.3 Optimization Methods for Parameter Identification 66
3.5.4 Application of Optimization Methods 70
3.6 Conclusion of Chapter 3 77

4 Simulation of Experimental Hysteretic Loops 83
4.1 Summary of Chapter 4 83
4.2 Introduction 84
4.3 Overview of Selected Experimental Hysteretic Loops 84
4.4 Simulation Methodology 86
4.5 Results of Simulations and Discussion 88
4.5.1 Application of Optimization Methods 95
4.6 Conclusions of Chapter 4 101

5 Dynamic Behavior of a Timber Panel 107
5.1 Summary of Chapter 5 107
5.2 Dynamic Behavior of a CLT panel 108
5.3 Test Procedure and Experimental Data 111
5.3.1 Hold–downs in axial direction 112
5.4 Mathematical Model for the Nonlinear Dynamic Analysis 116
5.4.1 Numerical implementation 118
5.5 Results of Numerical Analysis and Discussion 129
5.6 Practical Implications of the Study 135
5.7 Conclusions of Chapter 5 137

6 Conclusions 139

Bibliography 149

Author's publications 151

Acknowledgements

The research presented in this dissertation has been supported by the Italian Ministry of University and Research (MUR) and was co-funded with resources from the National Operational Program Research and Innovation 2014-2020, ESF REACT-EU resources. Action IV.4 "PhDs and research contracts on innovation themes" and Action IV.5 "Doctorates on Green themes".

This work was conducted as part of a co-tutorship agreement between Università Federico II di Napoli and Université Paris-Saclay, which offered the invaluable opportunity to spend one year in the Laboratory of Quartz at ISAE Supméca.

Additionally, a six-month internship was completed at Rubner Holzbau in Bressanone, Italy, where practical applications and insights related to timber structures were explored.

The contributions of all hosting institutions and research environments, as well as the support provided through funding programs, have been instrumental in completing this work.

List of Acronyms

The following acronyms are used throughout the thesis.

CLT	Cross-Laminated Timber
CNC	Computerized Numerical Control
LVL	Laminated Veneer Lumber
BMF	Board Measured Foot
VRM	Vaiana-Rosati Model
BWM	Bouc-Wen Model
GA	Genetic Algorithm
PSO	Particle Swarm Optimization
ASME	American Society of Mechanical Engineers
AB	Angle Brackets
HD	Hold-downs
CEM	Chang's Explicit Method
NLTHA	Non-linear Time History Analysis

List of Figures

2.1 Tension-Strain diagram characteristic of timber, in compression and tension. The scheme is adapted from the book of A. H. Buchanan[15]. 7

2.2 Difference between post-and-beam building system and timber framing. 8

2.3 Examples of different typologies of timber structures: (a) post-and-beam building, made by Zuber Construction in Shiner, Texas [71]; (b) log house made by Tender Company in Tudu, Estonia [58]; (c) CLT multistorey building design by Tallwood Architects in Coyhaique, Chile [54]; (d) glulam building *In'Cube Danone Research & Innovation Center*, design by Arte Charpentier Architects, in Gif-sur-Yvette, France [51]. 10

2.4 Typical force-displacement loops for different load levels of a timber joint under a cyclic load. The scheme is adapted from the paper of A. Ceccotti [18]. 13

2.5 Scheme of the typical hysteresis behavior of a timber connection with metallic fasteners when subjected to a cyclic load with increasing amplitude. The scheme is reproduced from the book of M. Piazza, R. Modena, and R. Tomasi in [50]. 14

2.6 Scheme of limiting curves proposed in the VRM: (a) *S1*, (b) *S2*, (c) *S3*, (d) *S4*. 15

2.7 Loading protocol for shear loading on the angle bracket tested by Cao et al. in [16] and scheme of the test set-up 17

2.8 (a) Experimental loop exhibited by the angle bracket and (b) its backbone curve. 17
2.9 Limiting curves for each hysteresis loop 18
2.10 Loading protocol for shear loading on the angle bracket tested by Gavric et al. in [30] and scheme of the test set-up 19
2.11 (a) Experimental loop exhibited by the angle bracket and (b) its backbone curve. 19
2.12 Limiting curves for each hysteresis loop 20
2.13 Loading protocol for shear loading on the hold-down tested by Gavric et al. in [30] and scheme of the test set-up 23
2.14 (a) Experimental loop exhibited by the hold-down and (b) its backbone curve. 23
2.15 Limiting curves for each hysteresis loop 24
2.16 Loading protocol for shear loading on the hold-down tested by Li, Wanh, He in [40] and scheme of the test set-up 26
2.17 (a) Experimental loop exhibited by the hold-down and (b) its backbone curve. 26
2.18 Limiting curves for each hysteresis loop 27
2.19 Loading protocol for shear loading on the T-connection tested by Ajavakom, Ng, and Ma in [7] and scheme of the test set-up 30
2.20 (a) Experimental loop exhibited by the hold-down and (b) its backbone curve. 30
2.21 Limiting curves for each hysteresis loop 31
2.22 Loading protocol for shear loading on the beam-to-pillar connection tested by Fairweather in [28] and scheme of the test set-up . . 33
2.23 (a) Experimental loop exhibited by the hold-down and (b) its backbone curve. 33
2.24 Limiting curves for each hysteresis loop 34
2.25 Loading protocol for shear loading on the Single-share nail connection tested by Lim in [41] and scheme of the test set-up 37
2.26 (a) Experimental loop exhibited by the hold-down and (b) its backbone curve. 37
2.27 Limiting curves for each hysteresis loop 38

2.28 Loading protocol for shear loading on the Single-share nail connection tested by Dong et al. in [26] and scheme of the test set-up 39

2.29 (a) Experimental loop exhibited by the hold-down and (b) its backbone curve. 39

2.30 Limiting curves for each hysteresis loop 40

3.1 Simulation of the experimental hysteresis loop of a timber connection tested by Yang et al. [72], using: (a) the Bouc-Wen Model and (b) the Dolan Model. 46

3.2 Generalized loading f^+ and unloading curves f^-, upper and lower limit curves c_u and c_l. 48

3.3 Illustration of the generalized tangent stiffness function k_t corresponding to the loading (a) and unloading (b) phases of the hysteresis loop shown in Figure 3.2. 51

3.4 Illustration of the generalized work function W corresponding to the loading (a) and unloading (b) phases of the hysteresis loop shown in Figure 3.2. 55

3.5 Influence of Vaiana-Rosati Model parameters on the shape of the hysteresis loop 64

3.6 Example of the iteration process of the Nelder-Mead simplex method on a two-dimensional simplex. 69

3.7 Example of the operation process of the genetic algorithm. 70

3.8 Flowchart of the optimization process of hysteresis model parameters. 75

3.9 Examples of the optimized hysteresis loops, comparing the experimental loops with the simulated one using the *fminsearch* and Genetic Algorithms. 76

4.1 Simulation of the first cycle of the experimental hysteresis loops using the VRM: (a) angle bracket and (b) hold-down tested by Gavric et al.[30], (c) beam-to-pillar connection tested by Fairweather [28] and (d) single shear wall tested by Dong et al. [26] 88

4.2 Simulation of the experimental hysteresis loops using the VRM: (a) angle bracket and (b) hold-down tested by Gavric et al.[30], (c) beam-to-pillar connection tested by Fairweather [28] and (d) single shear wall tested by Dong et al. [26] 90
4.3 Comparison of the dissipated energy per cycle between the experimental hysteresis loop and the simulated one by the use of the VRM: (a) angle bracket and (b) hold-down tested by Gavric et al.[30], (c) beam-to-pillar connection tested by Fairweather [28] and (d) single shear wall tested by Dong et al. [26] 92
4.4 Variation of the k_b parameter in function of the dissipated energy in the case of the simulated hysteretic loop of the angle bracket tested by Gavric et al.[30] 96
4.5 Variation of the f_0 parameter in function of the dissipated energy in the case of the simulated hysteretic loop of the angle bracket tested by Gavric et al.[30] 96
4.6 Variation of the α parameter in function of the dissipated energy in the case of the simulated hysteretic loop of the angle bracket tested by Gavric et al.[30] 96
4.7 Variation of the β_1 parameter in function of the dissipated energy in the case of the simulated hysteretic loop of the angle bracket tested by Gavric et al.[30] 97
4.8 Variation of the β_2 parameter as a function of the dissipated energy in the case of the simulated hysteretic loop of the angle bracket tested by Gavric et al.[30] 97
4.9 Variation of the γ_1 parameter in function of the dissipated energy in the case of the simulated hysteretic loop of the angle bracket tested by Gavric et al.[30] 97
4.10 Variation of the γ_2 parameter in function of the dissipated energy in the case of the simulated hysteretic loop of the angle bracket tested by Gavric et al.[30] 98
4.11 Variation of the γ_3 in function of the dissipated energy in the case of the simulated hysteretic loop of the angle bracket tested by Gavric et al.[30] 98

4.12 Comparison between the experimental angle bracket hysteresis loop tested by Gavric et al.[30] and the loops simulated by manually calibrating the VRM and using the genetic algorithm: (a) Cycle 1; (b) Cycle 2. 100

4.13 Comparison between the experimental angle bracket hysteresis loop tested by Gavric et al.[30] and the loops simulated by manually calibrating the VRM and using the genetic algorithm: (a) Cycle 3; (b) Cycle 4; (c) Cycle 5; (d) Cycle 6. 101

4.14 Variation of the k_b parameter as a function of the dissipated energy for the simulated hysteretic loop of the angle bracket (tested by Gavric et al.[30]) and the GA-optimized procedure. 102

4.15 Variation of the f_0 parameter as a function of the dissipated energy for the simulated hysteretic loop of the angle bracket (tested by Gavric et al.[30]) and the GA-optimized procedure. 102

4.16 Variation of the α parameter as a function of the dissipated energy for the simulated hysteretic loop of the angle bracket (tested by Gavric et al.[30]) and the GA-optimized procedure. 104

4.17 Variation of the β_1 parameter as a function of the dissipated energy for the simulated hysteretic loop of the angle bracket (tested by Gavric et al.[30]) and the GA-optimized procedure. 104

4.18 Variation of the β_2 parameter as a function of the dissipated energy for the simulated hysteretic loop of the angle bracket (tested by Gavric et al.[30]) and the GA-optimized procedure. 104

4.19 Variation of the γ_1 parameter as a function of the dissipated energy for the simulated hysteretic loop of the angle bracket (tested by Gavric et al.[30]) and the GA-optimized procedure. 105

4.20 Variation of the γ_2 parameter as a function of the dissipated energy for the simulated hysteretic loop of the angle bracket (tested by Gavric et al.[30]) and the GA-optimized procedure. 105

4.21 Variation of the γ_3 parameter as a function of the dissipated energy for the simulated hysteretic loop of the angle bracket (tested by Gavric et al.[30]) and the GA-optimized procedure. 105

5.1 CLT Panel connected to the foundation with n.2 hold-downs and n.4 angle bracket and subjected to vertical (F_v) and horizontal (F_h) loads. 109
5.2 General deflection modes of a timber structure: (a) sliding, (b) rigid rocking, (c) shear distortion, and (d) flexural deformation. . . 110
5.3 Loading protocol for axial loading on the hold-down tested by Gavric et al. in [30] and scheme of the test set-up 112
5.4 Experimental loop exhibited by the hold-down when loaded in axial direction. 113
5.5 Simulation of the experimental hysteresis loop of the hold-down tested by Gavric et al. [30] in the axial direction by using the VRM: (a) first cycle and (b) complete loop. 115
5.6 Mathematical Model with selected generalized coordinates. 117
5.7 Scheme of elastic stiffness variation in hold-downs according to the displacement sign, where the elastic force is $F_e = k_e u_1$, with k_e elastic stiffness. 119
5.8 Applied generalized external forces for the three degrees of freedom: (a) constant load along x_1, (b) harmonic force with increasing amplitude along x_2, and (c) null rotation along θ_3. 125
5.9 Hysteretic Forces at P_1 and P_2 base points: (a) in hold-downs (axial direction) and (b) angle brackets (shear direction). 127
5.10 Comparison of dissipated energy in hysteresis springs in points P_1 and P_2, with tests on single connections: (a) the case of hold-downs (HD), and (b) the case of angle brackets (AB). 127
5.11 Total Hysteretic Force in the System: (a) axial direction (hold-downs), and (b) shear direction (angle brackets). Comparison between the experimental hysteresis loops and the analytical prediction using the VRM. 128
5.12 Time history of the (a) displacement u_1 and (b) acceleration $\ddot{u}_1$ related to the Center of Gravity along direction x_1. 130
5.13 Time history of the (a) displacement u_2 and (b) acceleration $\ddot{u}_2$ related to the Center of Gravity along direction x_2. 130
5.14 Time history of the (a) rotation θ_3 and (b) rotational acceleration $\ddot{\theta}_3$ related to the Center of Gravity about x_3 axis. 131

5.15 Time history of displacement at the base points P_1 and P_2: (a) $u_1^{P_1}$ displacement of point P_1 along x_1 direction, (b) $u_2^{P_1}$ displacement of point P_1 along x_2 direction, (c) $u_1^{P_2}$ displacement of point P_2 along x_1 direction, and (d) $u_2^{P_2}$ displacement of point P_2 along x_2 direction. 132
5.16 Accuracy of Chang explicit method as a function of the time step chosen: $\Delta t = 0.01 - 0.001 - 0.0001$ s in (a) displacement u_1, (b) displacement u_2, and (c) rotation θ_3 recorder at the center of mass G. 134
5.17 Accuracy of Chang explicit method as a function of the time step chosen: $\Delta t = 0.001 - 0.0001s$ in computing the Hysteretic Force (a) with axial displacements u_1 (hold-downs), and (b) lateral displacements u_2 (angle brackets). 135

List of Tables

2.1 Features of Angle Bracket Connection. 22
2.2 Features of Hold-Down Connection. 28
2.3 Features of Beam-to-Pillar Connection. 35
2.4 Features of Single Shear Nail Connection. 41

3.1 Summary of Vaiana-Rosati Model parameters and their roles for hysteresis loop shape. 65
3.2 VRM Parameters used as initial values and optimized by *fminsearch* and Genetic Algorithm to simulate the hysteresis loop in Figure 3.9a. 78
3.3 Comparison between *fminsearch* and Genetic Algorithm to simulate the hysteresis loop in Figure 3.9a. 78
3.4 VRM Parameters used as initial values and optimized by *fminsearch* and Genetic Algorithm to simulate the hysteresis loop in Figure 3.9b. 79
3.5 Comparison between *fminsearch* and Genetic Algorithm to simulate the hysteresis loop in Figure 3.9b. 79
3.6 VRM Parameters used as initial values and optimized by *fminsearch* and Genetic Algorithm to simulate the hysteresis loop in Figure 3.9c. 80
3.7 Comparison between *fminsearch* and Genetic Algorithm to simulate the hysteresis loop in Figure 3.9c. 80

3.8 VRM Parameters used as initial values and optimized by *fminsearch* and Genetic Algorithm to simulate the hysteresis loop in Figure 3.9d. 81
3.9 Comparison between *fminsearch* and Genetic Algorithm to simulate the hysteresis loop in Figure 3.9d. 81

4.1 Initial set of VRM parameters adopted for simulating the first cycles of the experimental hysteresis loops shown in Figure 4.1 . . 87
4.2 Final set of VRM parameters adopted for simulating the experimental hysteresis loops shown in Figures 4.2 changed as a function of the generalized work. 89
4.3 Comparison of the dissipated energy per cycle between the experimental hysteresis loops and the simulated one shown in Figures 4.2. 93
4.4 Comparison of the dissipated energy per cycle between the experimental hysteresis loop of the angle bracket tested by Gavric et al.[30] and the simulated loop by calibrating the VRM manually (W_{sim}) and by using an optimization technique, the Genetic Algorithm (W_{opt}). 103

5.1 Mechanical properties of CLT panel tested by Gavric et al. in [30]. 111
5.2 Initial set of VRM parameters adopted for simulating the first cycles of the experimental hysteresis loops shown in Figure 5.5a . . 116
5.3 Final set of VRM parameters adopted for simulating the experimental hysteresis loops shown in Figures 5.5b changed as a function of the generalized work. 116
5.4 Flowchart with steps for implementing the NLTH of a CLT panel with hysteretic connections under combined vertical and horizontal loading. 120
5.5 Computational time required to make the NLTHA with different time steps. 135

List of Symbols

The following symbols are used within the thesis

c^+	Generalized loading curve
c^-	Generalized unloading curve
c_l	Generalized lower curve
c_u	Generalized upper curve
f	Generalized force
f^+	Generalized loading force
f^-	Generalized unloading force
f_0	VRM parameter
f_e	Generalized elastic force
f_{hyst}	Hysteretic force
f_P	Generalized force of generic point P
k_t^+	Generalized positive stiffness
k_t^-	Generalized negative stiffness
k_b	VRM parameter
k_e	Generalized elastic stiffness

OF	Objective Function in optimization process
t	Time
u	Displacement
u_P	Generalized displacement of generic point P
W	Generalized work performed by the generalized force f
W^+	Generalized work performed by the generalized force f^+
W^-	Generalized work performed by the generalized force f^-
α	VRM parameter
β_1	VRM parameter
β_2	VRM parameter
ϵ	Strain
γ_1	VRM parameter
γ_2	VRM parameter
γ_3	VRM parameter
σ	Stress

Chapter 1

Introduction

Timber, a renewable and versatile material, has gained increasing recognition as a sustainable and innovative solution for the construction industry. Its appeal extends beyond its aesthetic qualities, encompassing significant environmental advantages and mechanical properties that position it as a key material for the future of sustainable construction. Compared to traditional materials like concrete and steel, timber boasts a much lower carbon footprint. While the production of concrete and steel involves energy-intensive processes with substantial greenhouse gas emissions, timber serves as a natural carbon sink, storing carbon dioxide absorbed during the tree's growth. Studies, such as those conducted by Pomponi et al. [35], highlight that substituting timber for conventional materials in building systems can lead to substantial reductions in embodied carbon, aligning with global efforts to combat climate change. This environmental benefit, combined with its lightness and high structural performance, makes timber a competitive material for sustainable development.

The construction sector is one of the largest contributors to global CO_2 emissions, accounting for nearly 40% of energy-related emissions worldwide [23]. International initiatives, such as the European Green Deal [27] and the United Nations Sustainable Development Goals (SDGs) [46], emphasize the urgent need to reduce greenhouse gas emissions and transition toward sustainable construction practices. For instance, the European Green Deal targets climate neutrality by 2050, with interim goals like reducing emissions by 55% by 2030. Similarly, the Paris Agreement unites nations worldwide to limit global warming to below 2°C, preferably 1.5°C, above pre-industrial levels [21]. Within this framework, timber has emerged as a frontrunner in the global push toward low-carbon construction. Advanced timber technologies, including Cross-Laminated Timber (CLT) and hybrid systems, demonstrate the material's adaptability to modern architectural and structural demands.

Beyond environmental considerations, timber's application in construction is especially pertinent in areas prone to seismic activity. Its low weight reduces seismic forces, while its ductility and energy-dissipation capacity, particularly in its connections, enhance structural resilience during earthquakes [50]. These connections, however, introduce unique challenges. Timber connections exhibit complex hysteretic behaviors under cyclic loading, including pinching, stiffness degradation, and asymmetric loops. These nonlinear phenomena significantly impact the overall performance of timber structures, complicating their analysis and design for seismic applications.

To address these challenges, researchers have developed mathematical models to simulate the hysteretic behavior of timber connections under dynamic loads [26]. These models, such as the Bouc-Wen [12, 13, 70] and Dolan models [25], provide a basis for understanding structural responses but often involve complex parameterization with limited physical or geometric significance . Such complexities hinder the calibration of experimental loops and reduce the adaptability of these models to varying hysteresis behaviors. This limitation is particularly evident in timber connections, where hysteresis loop shapes vary significantly depending on the connection type. This thesis seeks to advance the understanding of the dynamic behavior of timber structures, focusing on their hysteretic connections under cyclic and seismic loads. The first objective is to classify the hysteresis loops associated with the principal categories of timber connections based on experimental campaigns. Following this, the thesis will utilize the Vaiana-Rosati Model (VRM) [65, 67, 66, 68, 61], a phenomenological hysteresis model, to simulate these experimental loops. The VRM is selected for its capacity to simulate diverse loop shapes (e.g., symmetric, asymmetric, pinched, and degraded) using a set of parameters with clear physical and geometric interpretations. To enhance the model's robustness, this study implements an automated optimization procedure to precisely identify the parameters, minimizing computational effort and improving reliability.

The culmination of this work is the analysis of the dynamic behavior of a CLT panel, where connections (angle brackets and hold-downs) are modeled using the VRM. By numerically simulating an experimental test, this study investigates the nonlinear dynamic response of the panel under combined vertical and horizontal loads. The numerical experiments reveal the interplay between displacement, rotation, energy dissipation, and computational efficiency, offering valuable insights for the design and optimization of timber structures in seismic regions. The findings aim to contribute to safer, more resilient timber construction and support global sustainability goals.

The thesis is structured as follows.

Chapter 2 begins by exploring the properties of timber as a building material, emphasizing its sustainability, lightness, and aesthetic appeal. It also examines

the advantages of using timber in the context of carbon footprint reduction compared to traditional materials such as concrete and steel. The chapter then reviews different structural typologies used globally, with a focus on the specific challenges and opportunities presented by timber structures in seismic regions. The chapter concludes with an in-depth discussion on the role of connections in timber construction, introducing their fundamental mechanical behavior and the importance of understanding hysteresis loops as a key feature in the dynamic performance of these systems.

Chapter 3 focuses on mathematical models of hysteresis, beginning with an overview of well-established models like the Bouc-Wen and Dolan models, and discussing their limitations when applied to timber connections. This chapter highlights the critical challenges posed by these models, such as the lack of physical interpretability of parameters and difficulty in adapting to the diverse hysteresis behaviors observed in timber connections. To address these issues, the VRM is introduced as a versatile and robust alternative, capable of simulating symmetric, asymmetric, pinched, and degrading hysteresis loops. This chapter also includes sensitivity analyses and parameter identification procedures by using different optimization methods to ensure the robustness and reliability of the model.

Chapter 4 builds on the theoretical groundwork established in the previous chapters by applying the VRM to experimental data of timber connections. The chapter provides a detailed classification of hysteresis loops for different connection types based on experimental campaigns from the literature. By simulating these loops with the VRM, the chapter evaluates its accuracy and flexibility while also identifying potential challenges and limitations. Proposed solutions and future directions are discussed to further enhance the model's applicability and reliability in simulating timber connections under dynamic loading conditions.

Chapter 5 extends the analysis to a practical application by conducting a dynamic study of a Cross-Laminated Timber (CLT) panel. This chapter investigates the nonlinear dynamic response of the panel, which is connected to the foundation through angle brackets and hold-downs. Using numerical simulations, the chapter examines the interactions between displacement, rotation, and energy dissipation, providing insights into the seismic performance of timber panels. The findings demonstrate the potential of the VRM to simulate complex structural behavior under dynamic loading and offer guidance on optimizing timber structures for seismic applications.

Chapter 6 synthesizes the key findings from the thesis and reflects on their broader implications for the timber construction industry. It discusses the contributions made to understanding the dynamic behavior of timber connections and structures, as well as their significance in advancing sustainable construction practices in seismic areas. The chapter also outlines potential areas for future

research, including the further development of hysteresis models, experimental validation of dynamic responses, and the application of these findings to real-world timber structures.

This work aims to contribute to the body of knowledge on the seismic behavior of timber structures and enhance the reliability of their design and analysis under real-world conditions. By combining analytical and numerical approaches, this research investigates the dynamic response of timber connections and structures under cyclic and seismic loads, focusing on the complexities of their hysteretic behavior. This thesis ultimately seeks to bridge the gap between timber's recognized environmental benefits and its performance in challenging seismic conditions. By advancing our understanding of timber structures, the findings will not only address critical challenges in their seismic design but also support the global shift toward sustainable construction practices—further solidifying timber's role as a cornerstone of eco-conscious and resilient building solutions.

Chapter 2

Timber Structures in Seismic Areas

2.1 Summary of Chapter 2

This chapter will explore the key characteristics of timber as a structural material and examine various typologies of timber buildings and connections [50, 14, 53]. The focus is particularly on metallic connections, such as angle brackets, hold-downs, beam-to-pillar connections, and in-plane screwed joints between timber panels, which play a crucial role in ensuring the structural resilience of timber buildings under dynamic loads, particularly seismic events. Hysteresis loops generated by these connections, taken from experimental campaigns conducted by researchers in the scientific literature [16, 30, 40, 7, 28, 72, 26, 41], will be analyzed in detail. Each loop will be studied by examining both the envelope and limiting curves, providing insights into the ductile capacity and energy dissipation potential of these connections during seismic events. These analyses emphasize the critical role of connection design in achieving effective energy dissipation and ensuring structural safety in timber structures subjected to earthquakes.

2.2 Timber as Building Material

Timber is one of humankind's oldest building materials and has grown in popularity in recent decades due to its sustainability, versatility, and aesthetic appeal. Throughout history, timber has been used for various construction purposes, ranging from basic shelters to intricate architectural marvels. The inherent

properties of timber make it an attractive choice for construction in seismic areas, where resilience and flexibility are essential. As an exceptional action, the seismic action requests structures to react beyond the limits of their usual behavior. In this way, it is possible to underline the pros and cons of the structures and highlight whose features can be implemented to have a positive behavior and maintain the structures in security. For these reasons, it is not enough to base the design process on experience data. Instead, these last need to be achieved through experimental and analytical test results on timber elements, joints, and structures[50, 14, 53].

In general, timber is commonly considered more efficient for its response in seismic conditions due to its lightness, excellent deformability, and flexibility than reinforced concrete. The resistance-mass ratio is about the same as steel and five times greater than reinforced concrete. On the other hand, timber does have a brittle failure behavior in the case of parallel and perpendicular tension to the grain structure, which can cause instability problems and overcome elastic behavior. Moreover, timber has greater stiffness and strength along the grain direction than the transverse one, with a reduction of about 90% of resistance when the stress changes from the parallel to the perpendicular direction (Figure 2.1). In addition, timber has a ductile compression behavior over the elastic limit but a brittle one in tension. Focusing on the natural structure of the material can help us understand its behavior better. In the case of compression parallel to the grain, the collapse arrives when fibers lose their stability, bending on themself. Later, the collapse resulting in the compression perpendicular to the grain is due to lateral crushing of woody cells, followed by an extended phase of pseudo-elastic deformation. In the case of tension, the response of timber is elastic and brittle, and the resistance depends on the inclination of the force in confronting the grain. When the stress is parallel to the grain, timber has a better resistance because longitudinal fibers can stretch until the timber textile reaches the fracture. On the contrary, when tension is perpendicular to the grain, collapse is highly brittle because it involves the detachment of internal wood walls [50, 15, 45].

In the case of dynamic and seismic events, structures must provide overall ductility because the oscillatory shape of the action brings the structure into the plastic field, creating hysteretic loops. This situation is heavy for every material typology, degrading their mechanical capability and ductility. However, relating to the quality and typology of hysteresis loops, the structure can dissipate energy when a dynamic event occurs. Timber cannot react well to these events and dissipate energy, so timber is usually associated with other materials, especially steel. Connections are the collaboration area in which timber and steel coexist; to them, the task is dissipating energy and giving the plastic answer during a dynamic event [52].

The specific answer of timber building during seismic excitation is strictly

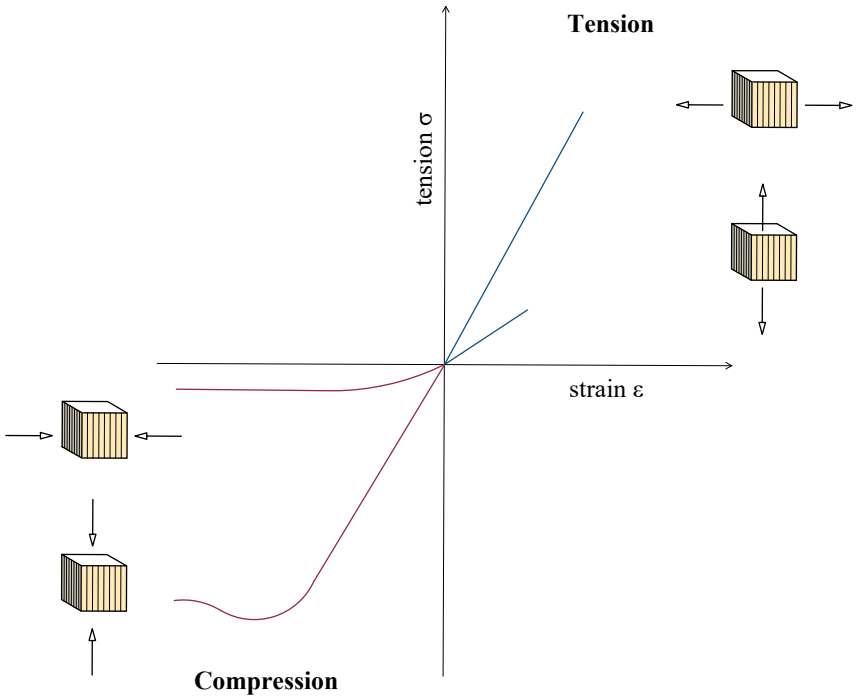


Figure 2.1. Tension-Strain diagram characteristic of timber, in compression and tension. The scheme is adapted from the book of A. H. Buchanan[15].

related to the design choices regarding the typology of structures and specific connections. For these reasons, it is useful to overview the widespread typologies of timber structures and their connections before analyzing their specific hysteretic behavior.

2.3 Typologies of Timber Structures

Timber structures include a diverse array of typologies reflecting the rich history and ongoing innovation within the construction industry. From traditional timber framing and log construction to modern engineered wood products like Cross-Laminated Timber (CLT) and glued laminated timber (glulam), the ver-

satility of timber as a building material is evident. Each typology offers unique advantages and characteristics, meeting various architectural styles, structural requirements, and sustainability goals [53].

Timber framing is one of the oldest and most traditional layouts of timber construction. It involves using large timber members, typically beams and columns, assembled into a framework using traditional mortise and tenon or dovetail joints.

Post-and-beam construction is similar to timber framing but typically involves fewer members and more straightforward joinery. The picture in Figure 2.3a shows an example of this typology. It consists of vertical timber posts supporting horizontal beams, forming a structural framework that can be infilled with various materials such as timber panels, glass, or masonry. Moreover, in this case, timber beams are connected using metal brackets and steel plates (Figure 2.2).

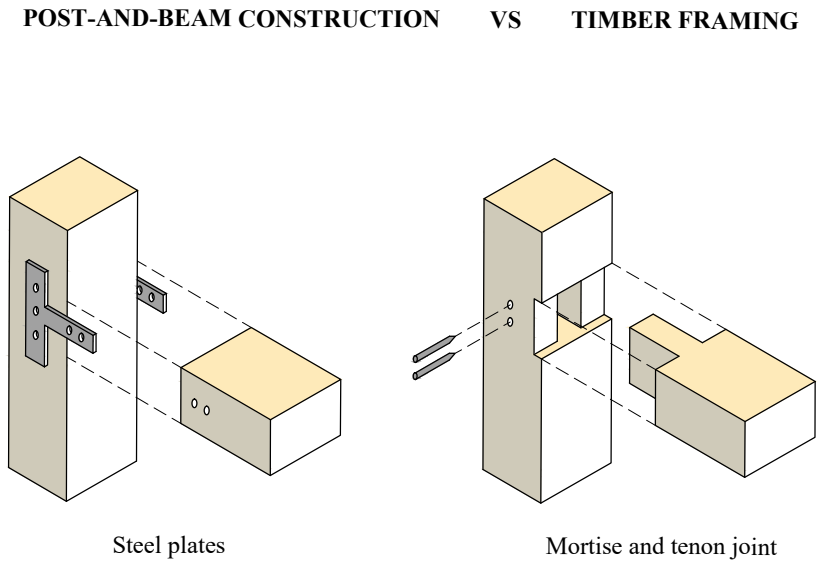


Figure 2.2. Difference between post-and-beam building system and timber framing.

Log construction utilizes whole logs or milled logs stacked horizontally to form walls. This traditional construction method is commonly associated with

rustic or log cabin-style buildings and offers excellent thermal insulation. An example of this building is shown in Figure 2.3b.

CLT is a modern engineered wood product consisting of multiple layers of timber boards glued together at right angles. CLT panels are well-known for their strength, stability, and fire resistance, making them suitable for a wide range of building applications, including walls, floors, and roofs. CLT construction allows for rapid assembly and can be prefabricated off-site for efficient on-site installation. Nowadays, multistorey buildings in CLT technology are spreading worldwide, and Figure 2.3c shows a design example.

Glued laminated timber is another engineered wood product made by bonding multiple layers of timber together with structural adhesives. Glulam beams and columns offer superior strength and flexibility compared to solid timber members, allowing for longer spans and more complex architectural designs. Glulam is commonly used in large-scale commercial and institutional buildings as well as residential structures. Figure 2.3d shows an innovative research building project made by glulam and CLT technology.

Timber hybrid structures combine timber with other materials such as steel, concrete, or glass to capitalize on the unique properties of each material. Hybrid structures take advantage of the sustainability and aesthetics of wood while benefiting from the strength, durability, or transparency of other materials. This approach allows for innovative design solutions that meet specific functional, aesthetic, and structural requirements.

These are just a few examples of the widespread typologies of timber structures. The versatility and adaptability of timber as a building material continue to inspire architects, engineers, and builders to push the boundaries of design and construction, creating sustainable, resilient, and visually stunning buildings and structures worldwide.

2.4 Typologies of Timber Connections

During the timber structures project, the decision about the type of joints depends on the typology of the structure chosen and the mechanic characteristics requested. There are three main types of joints: traditional, metallic, and adhesive, each offering distinct advantages and considerations. Traditional joints, also known as carpentry joints, are used mostly in traditional timber buildings, such as timber framing. They are made of cut surfaces, and the connection is characterized by stress transmission thanks to the touch between the various connected surfaces. Nowadays, traditional joints are chosen in the case of small buildings where there is a possibility of transmitting compressive stresses easily. Still, the end parts of wood elements are cut with CNC (Computerized Numerical Control)



(a)



(b)



(c)



(d)

Figure 2.3. Examples of different typologies of timber structures:
(a) post-and-beam building, made by Zuber Construction in Shiner, Texas [71];
(b) log house made by Tender Company in Tudu, Estonia [58];
(c) CLT multistorey building design by Tallwood Architects in Coyhaique, Chile [54];
(d) glulam building *In'Cube Danone Research & Innovation Center*, design by Arte Charpentier Architects, in Gif-sur-Yvette, France [51].

machines, and additional metal connectors are introduced [50].

Metallic joints, on the other hand, dominate timber connections, offering a multitude of fastening options, including nails, screws, bolts, rings, and metal plates. The choice of fastener depends on the specific requirements of the connection. In general, metallic joints can be categorized into flexible and rigid connections. Flexible connections permit relative rotation between connected elements, realizing the scheme of a hinge, although it is hard to challenge in practice due to concerns like embedment strength. Conversely, rigid connections ensure simultaneous and rigid rotation of connected elements, often realized through metal plates and fasteners. The use of metallic fasteners is useful for reacting to shear stress, and the ductility of the joint is guaranteed by the number of metallic elements chosen, their inclination in the timber elements, and their slenderness. In the case of modern timber structures, particularly for multi-story buildings, two typologies of connections play a crucial role in achieving global ductility: angle brackets and hold downs. They connect floors or foundations to vertical elements, and the choice between angle brackets and hold-downs depends on which kind of stress the connection supports: shear for angle brackets or tensile stress for hold-downs.

Despite the versatility of metallic joints, timber connections are susceptible to localized brittleness issues due to stress concentration induced by individual connectors, leading to perpendicular tensile stresses and brittle fracture. Consequently, designing beam-column connections capable of dissipating energy and exhibiting ductility becomes imperative. This approach aligns with the resistance hierarchy of elements, as stipulated by European and Italian regulations [1, 5], wherein certain elements and zones are designated to undergo controlled inelastic deformation, ensuring a controlled collapse mechanism while preserving other structural zones in the elastic range and damage-free state. Regulations provide quantitative guidelines for determining the resistance of connections, often based on theoretical frameworks such as Johansen's theory (1949) [37]. These guidelines offer valuable insights into connections' structural integrity and load-bearing capacity, aiding designers in ensuring compliance with safety standards and structural requirements. However, despite the precision afforded by these numerical assessments, determining the ductility level of connections remains challenging, as it necessitates empirical validation through experimental testing. Moreover, experimental testing is a crucial tool for providing valuable insights into their deformation behavior, load-carrying capacity beyond the elastic limit, and ability to withstand cyclic loading, like in the case of seismic events. Through experimental tests, engineers can subject connections to realistic loading conditions, observing their response under different levels of stress and deformation. This empirical data enables the characterization of connection ductility, informing design decisions and ensuring timber buildings' structural robustness and resilience. By

integrating theoretical analyses and experimental validation, designers can develop connections that meet regulatory requirements for strength and exhibit the necessary ductility to withstand unexpected loading scenarios and ensure the safety and longevity of timber structures.

2.4.1 Experimental behavior of timber joints

Studying the experimental behavior of connections is a key way to understand if the timber structure can dissipate energy during a dynamic action, such as wind or earthquake, and if it can survive without serious damage. In addition, experimental studies can provide valuable data to refine design methodologies, improve structural details, and validate analytical models and numerical simulations, ensuring their accuracy and reliability in predicting the behavior of timber structures under dynamic loading conditions. During cyclic tests, a connection is subjected to increasing and decreasing loads, typically at varying frequencies and amplitudes. Hysteresis behavior refers to the relationship between the applied load and the resulting deformation of a material or structure. In the context of cyclic testing, hysteresis loops are graphical representations of this relationship, illustrating the energy dissipated by the material or connection as it undergoes cyclic loading. These loops are typically plotted on a graph with force or moment on the vertical axis and displacement or rotation on the horizontal axis. Figure 2.4 shows a typical hysteretic loop of a timber joint under a cyclic load. The shape and size of hysteresis loops provide valuable insights into the mechanical behavior of the connection. A wide loop suggests significant energy dissipation and ductility, suggesting the connection can absorb and dissipate energy effectively without excessive deformation or damage. In contrast, a narrow loop suggests limited energy dissipation and stiffness, indicating that the connection may be prone to fatigue failure or brittle behavior under cyclic loading.

In the case of timber connections, the hysteresis behavior is complicated and diversified compared to other traditional materials, such as concrete or steel. Several factors influence the hysteretic loop shape of timber connections, such as the type of connection (e.g., traditional, metal fasteners, adhesive), the configuration in terms of geometry and orientation, and the characteristics of the timber material (e.g., species, moisture content, grain orientation). The schematic response of a timber connection subjected to a cyclic load with increasing amplitude is illustrated in Figure 2.4. This figure plots the hysteresis force f_{hyst} against the displacement u, where u is an increasing function of time t. In general, it is possible to say that during the first loading cycle, the graph can give information on the stiffness and post-elastic deformation of the undamaged connection. As the loading and unloading phases gradually take place, pinching and degradation phenomena usually occur. Pinching is referred to the characteristic reduction of

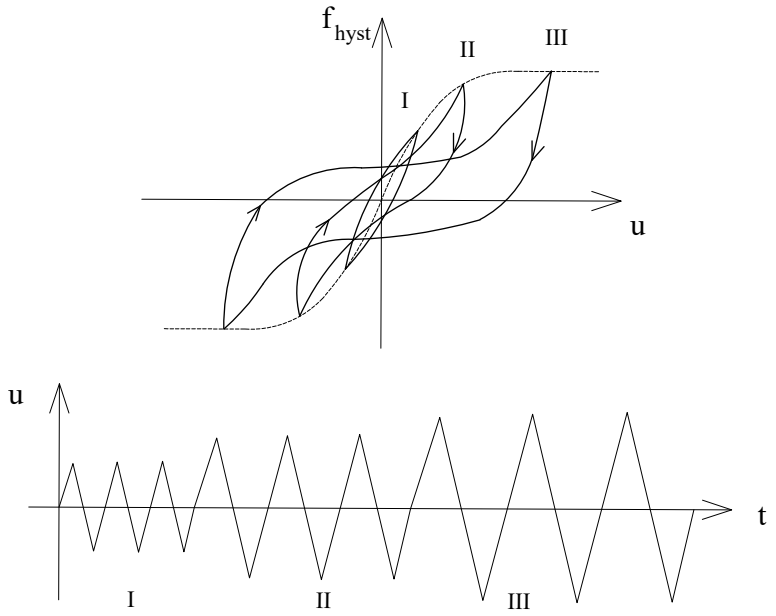


Figure 2.4. Typical force-displacement loops for different load levels of a timber joint under a cyclic load. The scheme is adapted from the paper of A. Ceccotti [18].

the central part of the hysteretic loop. It often occurs due to the gradual shift or displacement of metal fasteners within their respective holes in the timber elements. As cyclic loading continues, the repeated movement and deformation of the connection can lead to frictional forces and wear between the metal elements and surrounding timber material. This frictional interaction can alter the distribution of stresses and strains along the connection interface. On the other hand, the degradation phenomenon is related to strength and stiffness reduction due to the gradual deterioration or loss of mechanical properties. This phenomenon usually occurs in the cyclic load's final phases before the connection collapses. In research studies, it is usual to describe the hysteresis behavior introducing the backbone curve, also known as the skeleton or envelope curve. This curve can capture essential features such as the variation of stiffness and strength during loading history, allowing researchers to analyze and compare the performance of different designs, materials, or loading scenarios [26, 16, 56, 8]. Another way to

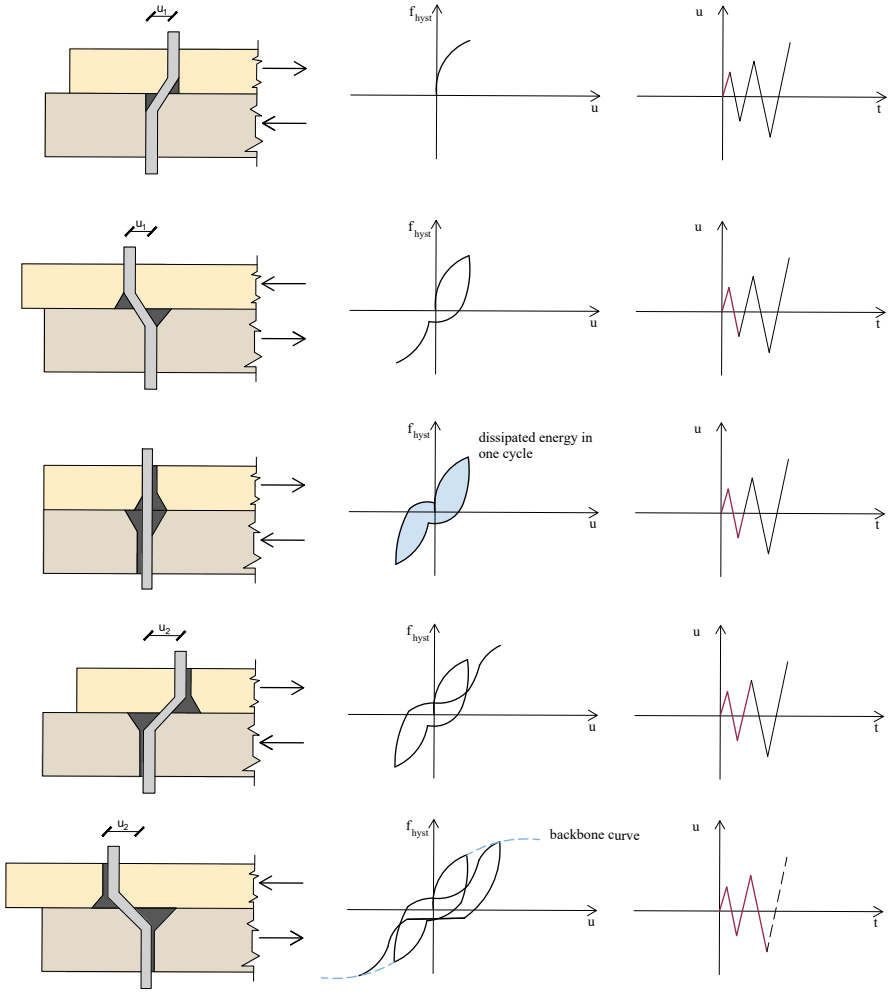


Figure 2.5. Scheme of the typical hysteresis behavior of a timber connection with metallic fasteners when subjected to a cyclic load with increasing amplitude. The scheme is reproduced from the book of M. Piazza, R. Modena, and R. Tomasi in [50].

analyze how the hysteresis behavior changes and classify the different loop shapes is by using the limiting curves, following the approach proposed by Vaiana and Rosati [63]. In this way, it is possible to classify hysteresis loop shapes into four categories:

- *S1*, when two straight lines delimit hysteresis loop;
- *S2*, when two curves with no inflection point delimit the hysteresis loop;
- *S3*, when two curves with one inflection point delimit the hysteresis loop;
- *S4*, when two curves with two inflection points delimit the hysteresis loop.

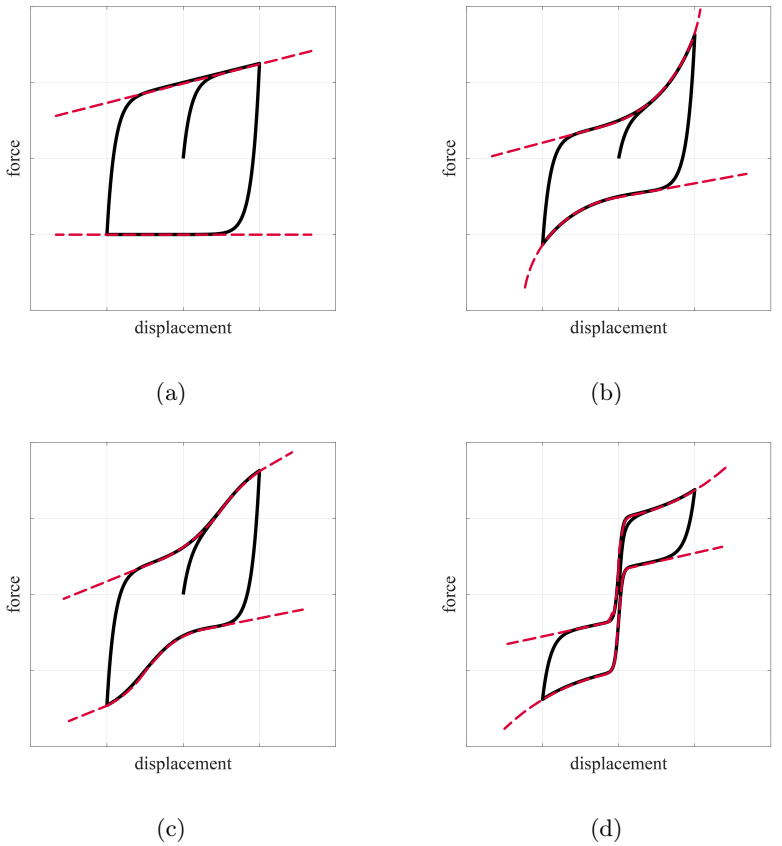


Figure 2.6. Scheme of limiting curves proposed in the VRM: (a) *S1*, (b) *S2*, (c) *S3*, (d) *S4*.

To classify the general properties of the hysteretic behavior of the most widely used timber connections, some cases of experimental tests in the scientific literature are studied and discussed. For each case, the backbone and limiting curves are plotted and analyzed.

Type 1: Angle Bracket

In timber frame, CLT, and Laminated Veneer Lumber (LVL) structures, angle brackets are typically used to connect timber elements, such as beams or columns, and resist lateral loads induced by wind or seismic forces. They are usually fabricated from steel and are available in various shapes and sizes to accommodate different structural configurations and load requirements. Moreover, they are attached to timber elements using metallic fasteners, such as nails, screws, or bolts, and the number and placement of fasteners depend on the load-carrying capacity and design requirements of the connection. During cyclic loading, angle brackets exhibit hysteresis behavior characterized by pinching of the hysteresis loop and gradual degradation of stiffness and strength. The loop shape reflects the connection's ability to dissipate energy and withstand repeated loading cycles.

The first scientific campaign taken into consideration is made by researchers Cao et al. in a paper published in 2020 [16]. The researcher's team tested an angle bracket and a hold-down, but only the angle bracket is considered in this paragraph. The experimental test was conducted in China at Tongji University, and the connection between a steel foundation and a wall in CLT was simulated. The connection set-up includes an angle bracket of 230x120x3 mm, screw fasteners of 5x60mm, and a CLT panel of 400x200 mm composed of n.3 layers of glued Canadian Hemlock wood species. The cyclic load test was displacement-controlled and followed EN 12512 [4], taking the value obtained from the monotonic test as the yield displacement value.

The connection experienced 15 mm of deformation upon application of 50 kN of shear force. In the plot of hysteresis curves, it is possible to extract the backbone curve, depicted in Figure 2.8. The curve shows that the strength of the connection increases as the loading test progresses, but the stiffness and strength of the connection degrade in the final phases. Figure 2.9 illustrates that the loop was pinched from the initial phases of the test, and the loop shape increased in amplitude during the central phases of the test. Furthermore, the loop passed through two types of limiting curves: from *S2*, with two curves without inflection points, to *S3*, with two curves with one inflection point for each. Gradually, the loops increased in size, and the inflection points shifted from the left to the right part of the limiting curve.

The second testing campaign made on an angle bracket and taken into consideration is published by researchers Gavric et al. [30] within the SOFIE project

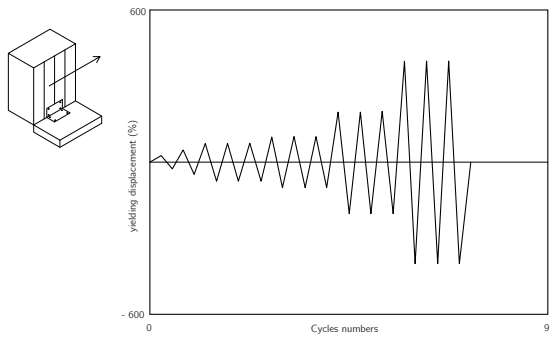
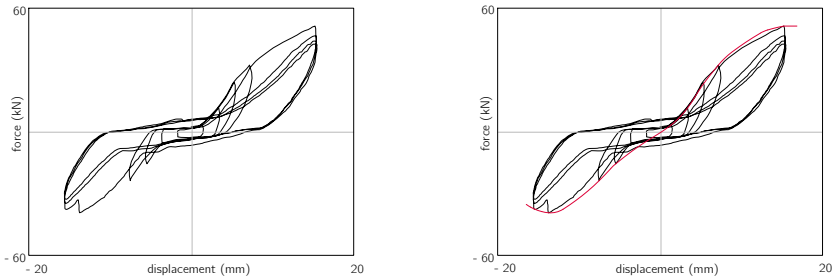


Figure 2.7. Loading protocol for shear loading on the angle bracket tested by Cao et al. in [16] and scheme of the test set-up



(a) (b)

Figure 2.8. (a) Experimental loop exhibited by the angle bracket and (b) its backbone curve.

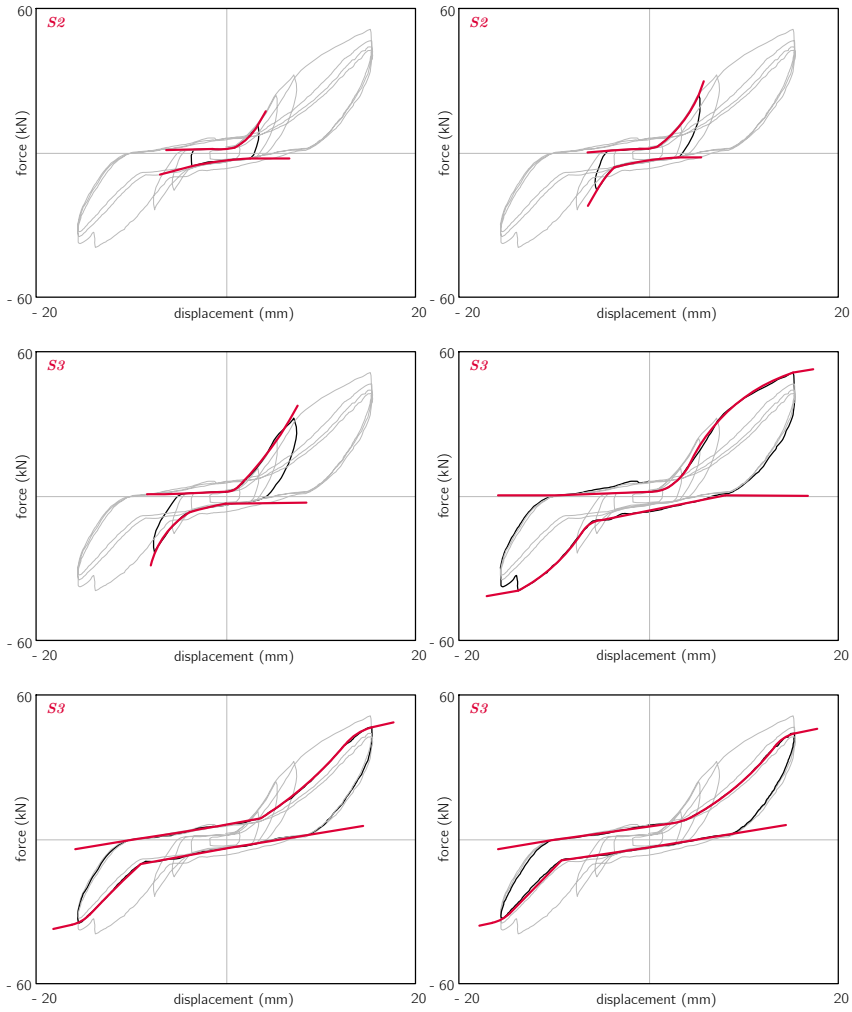


Figure 2.9. Limiting curves for each hysteresis loop

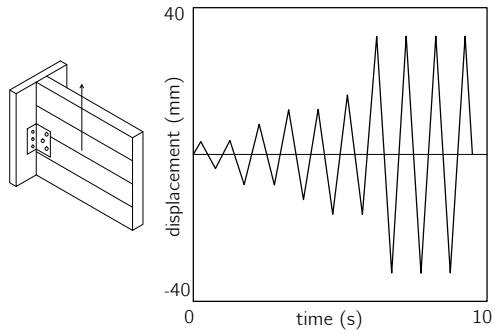
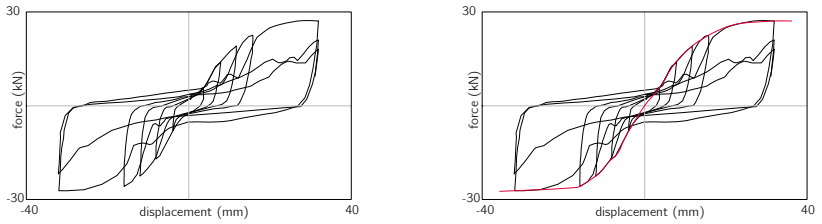


Figure 2.10. Loading protocol for shear loading on the angle bracket tested by Gavric et al. in [30] and scheme of the test set-up



(a) (b)

Figure 2.11. (a) Experimental loop exhibited by the angle bracket and (b) its backbone curve.

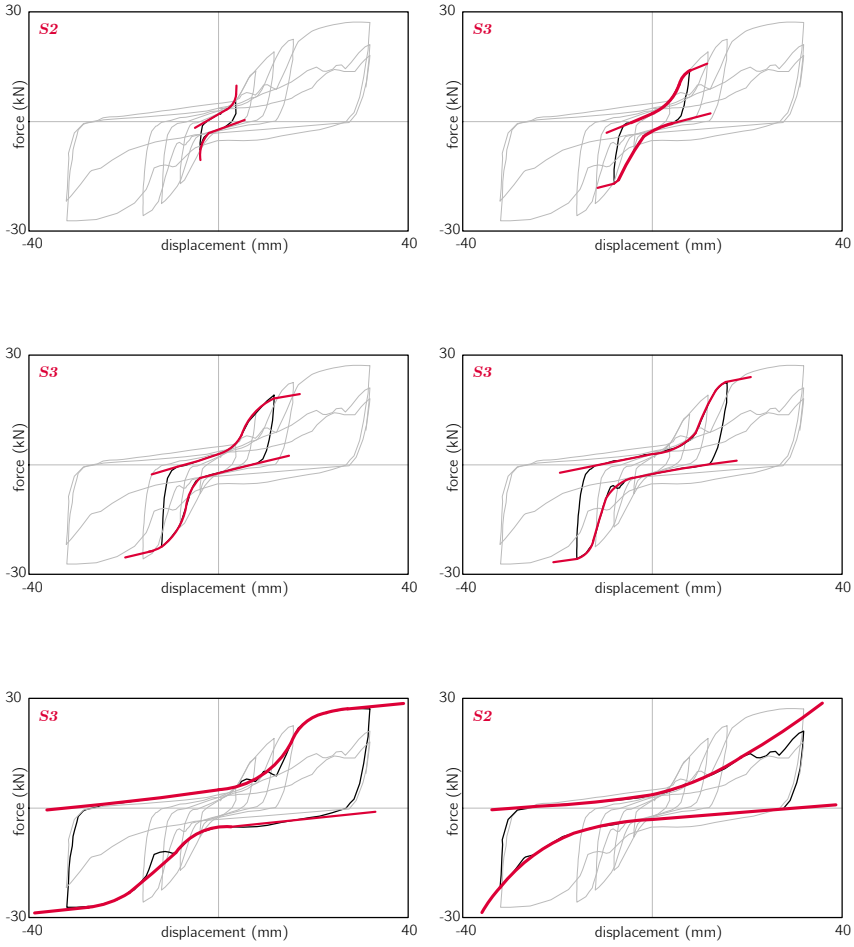


Figure 2.12. Limiting curves for each hysteresis loop

[47]. The connection type under exam is the BMF (Board Measured Foot) 90x116x48x3mm, made of 11 annular ringed nails sized 4x60 mm, as illustrated in Figure 2.10. Experimental monotonic and cyclic tests were conducted on a CLT panel composed of five orthogonally crossed layers, each measuring 17 mm thick. During the cyclic testing phase, a velocity input ranging from 0.4 mm/s to 0.8 mm/s was applied to the specimen. The results revealed favorable performance characteristics, particularly in shear, with the connection displaying commendable ductility up to 30 mm of displacement. Notably, connection failure was observed when the steel nails reached their yielding point, forming two plastic hinges and slightly ovalizing the hole surrounding the nail. Considering the backbone curve in Figure 2.11, the connection strength increases for every cycle until it reaches its resistance limit of around 27 kN with a deformation of 30 mm. Later, the connection has strength and stiffness degradation before reaching the collapse. In Figure 2.12, the limiting curves show that the hysteresis increases its complexity during the test; in fact, the loop becomes pinched immediately and increases its amplitude gradually during the loading history. It is a sign that the connection gradually increases the capacity to dissipate energy, but it decreases strongly in the final part of the test. The limiting curve starts with a *S3* shape, and the inflection point shifts from left (right) to right (left) for the (un)loading phase until the curves lose the inflection point and take shape *S2*.

Summarizing the features of the experimental hysteresis behavior of angle brackets, it is evident that the loop shape is pinched, and gradually, the connection is subjected to strength and secant stiffness degradation, a sign of reducing capacity in dissipating energy. The carrying capacity and deformation depend on the connection geometry in terms of timber panel and angle bracket dimensions and the number and types of metallic fasteners, whose characteristics also influence the size of the loop shape. Limiting curves of hysteresis loops used to be, initially simple curves of the type *S2*, later one or two inflection points appear, becoming *S3* or *S4* curve shapes, and finally, limiting curves degrade again to *S2* shapes, reducing their dissipating capacity until the collapse.

Type 2: Hold – down

In modern timber structures, hold-downs anchor them to their foundations, providing resistance against uplift forces induced by wind or seismic events and transferring vertical loads from the structure to the foundation. They prevent the structure from lifting off its foundation during extreme loading conditions. They typically consist of a metal bracket or plate secured to the timber structure using an anchor bolt embedded in the foundation. As in the case of angle brackets, hold-downs exhibit hysteresis behavior under cyclic loading conditions, with the loop shape reflecting the connection's capacity to dissipate energy and resist

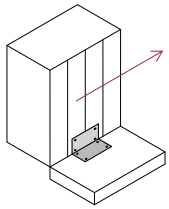
Typology of Connection	Position	Hysteresis Loop Shape
 Angle Bracket	Connect panel or pillar to beam or foundation	• Pronounced pinched loop shape • *S2* and *S3* limiting curve • Shift of inflection point • Increasing of loop amplitude • During final loops: – Reduction of secant stiffness – Reduction of loop area – Force degradation

Table 2.1. Features of Angle Bracket Connection.

uplift forces. The degradation of stiffness and strength over successive loading cycles may occur, influencing the overall performance of the hold-down connection. Usually, hold-downs are tested by applying a tensile force because the pull-out force is the primary action they must absorb. But, in this case, the hysteresis diagram shows a half-hysteresis loop, giving back less information on the loop shape. Therefore, to classify all connections using the same markers, it is more interesting to consider experimental shear tests, through which a complete shape of the hysteresis loop can be seen.

The first sample of hold-down taken into account is experimentally studied by Gavric et al. in [30], in the place of the previously analyzed project. The connection is made of a CLT panel 85 mm thick with n.5 orthogonally crossed layers. The hold-down used in the campaign is a WHT540 connected with 12 annual ringed nails Anker of 4x60 mm. Stationary and cyclic tests were made

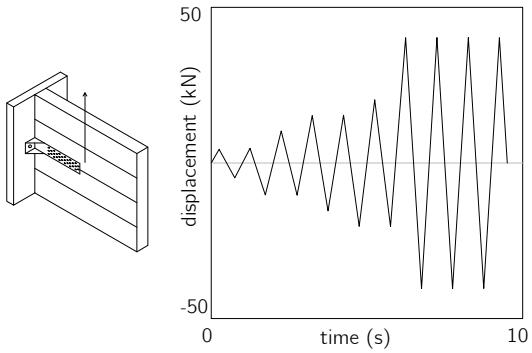
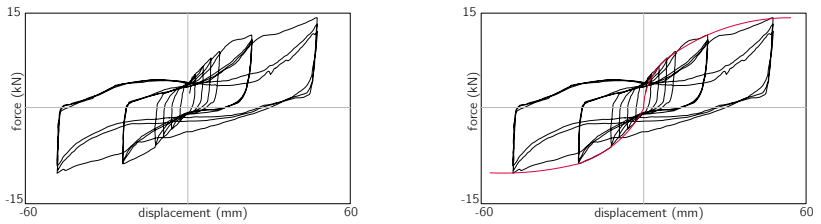


Figure 2.13. Loading protocol for shear loading on the hold-down tested by Gavric et al. in [30] and scheme of the test set-up



(a) (b)

Figure 2.14. (a) Experimental loop exhibited by the hold-down and (b) its backbone curve.

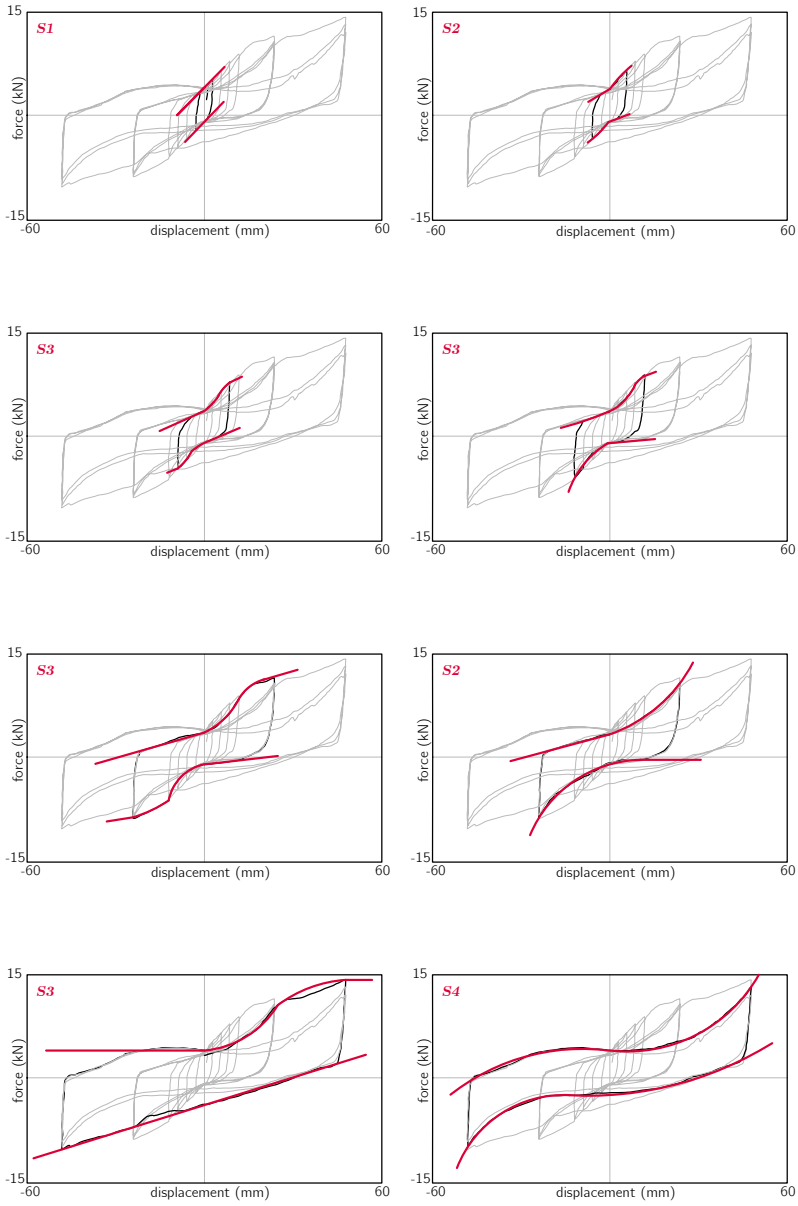


Figure 2.15. Limiting curves for each hysteresis loop

using a velocity input varying from 0.4 mm/s to 0.8 mm/s. The shear test reveals significant connection deformation attributed to local steel buckling and nail withdrawal. The connection reaches a high level of displacement, around 47 mm, with a limited force exerted, around 15 kN, highlighting the connection's ability to accommodate large displacements while maintaining structural integrity. Looking at the hysteresis diagram in Figure 2.14, the backbone curve shows that the strength of the connection increases during the cyclic test, with a slight reduction of the secant stiffness in the last part of the test. Moreover, examination of the limiting curves, as shown in Figure 2.15, reveals a moderately pinched loop shape, indicative of enhanced energy dissipation capabilities compared to conventional timber connections. In addition, in the first phases of the test, the loop shape changes moderately, passing from type *S1* to *S3* limiting curves. As the test progresses, further alterations in the limiting curves are observed with the shifting of the inflection point from the left (right) side to the right (left) for the (un)loading curve. Finally, a reduction of the inner area occurs, which means a starting decay of the connection in strength and dissipating energy.

The second sample considered is part of an experimental campaign carried out by Li, Wanh, and He in the paper [40]. The campaign refers to a study on CLT shear walls where connections, such as angle brackets, hold-downs, and wall-to-wall connections, are located in different specimen positions. The CLT panel is 105 mm thick, made of n.3 layers, and connected to a foundation steel plate. Hold-downs measure 165x80x3 mm and are connected to the foundation with 8.8s anchor bolts and to the CLT panel with self-tapping screws with dimensions 80x5 mm. The specimen was tested to cyclic test (Figure 2.16) observing the protocol ISO 16670 [3], using a controlled later displacement equal to 60 mm, corresponding to a 3 % inter-story drift of the shear wall analyzed. Considering Figure 2.17, the backbone curve of the hysteresis loop shows a slight degradation of the strength and secant stiffness during the last phase of the loop, reaching the resistance capacity around 20 kN and 50 mm of displacement. Only external loops corresponding to the loading load's peaks are considered to understand the shape variation of limiting curves. Indeed, the shape of the limiting curves does not change significantly during the loading history. The shape is maintained in the type *S3*, with one inflection point for each curve, which moves from left (right) to right (left) for the (un)loading curve. Moreover, the pinching phenomenon affects the hysteresis loop, but it influences less the global variation of the internal area, meaning an almost constant capability to dissipate energy.

In summary, the dynamic response of hold-downs to experimental tests is influenced by various factors, including the geometry of the timber element and the steel connection, the number of fasteners employed, the direction of the applied load, and the specific loading protocol utilized. These parameters collectively shape the observed hysteresis behavior and overall performance of the hold-down

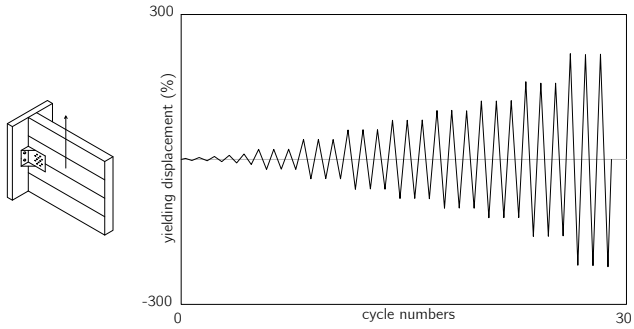
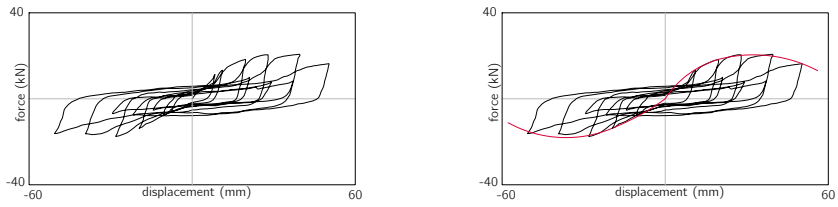


Figure 2.16. Loading protocol for shear loading on the hold-down tested by Li, Wanh, He in [40] and scheme of the test set-up



(a) (b)

Figure 2.17. (a) Experimental loop exhibited by the hold-down and (b) its backbone curve.

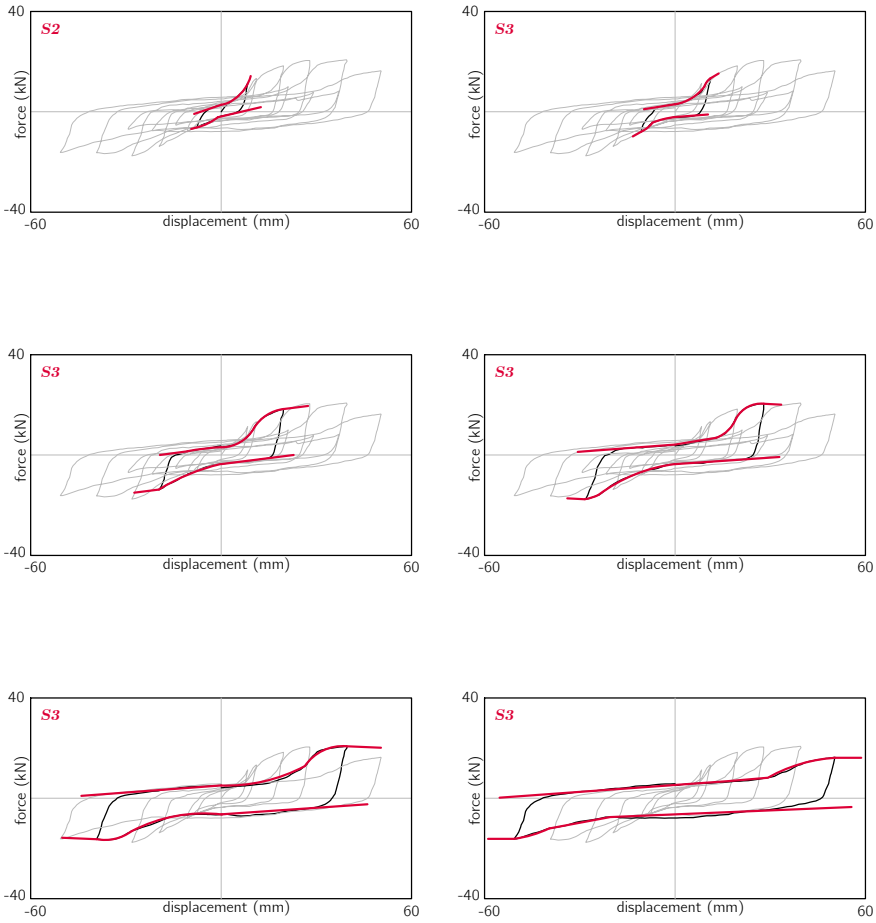


Figure 2.18. Limiting curves for each hysteresis loop

connection under cyclic loading conditions. By examining the hysteresis loops generated by dynamic tests, it is evident that hold-down connections are affected to a small degree by the phenomenon of pinching and secant stiffness degradation. Unlike other timber connections, such as angle brackets, the degree of strength degradation in hold-downs is generally less pronounced. Moreover, limiting curves of the hysteresis loops used to be of the *S3* type, with one inflection point, which moves horizontally during the cyclic test. In the final phases of the loop, the limiting curves degrade to *S2* type, meaning a reduction of the dissipating energy. These considerations mean a relatively stable connection behavior throughout the strain-stress cycle, even when subjected to varying loads and displacement. Despite potentially lower maximum forces reached during testing, this stability underscores the robustness and reliability of hold-down connections in providing anchorage and stability to timber structures.

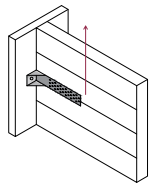
Typology of Connection	**Position**	**Hysteresis Loop Shape**
 Hold-down	Connect panel or pillar to beam or foundation	• *S3* limiting curve • Shift of inflection point • Increasing of loop amplitude • During final loops: – Reduction of secant stiffness – Reduction of loop area – Force degradation

Table 2.2. Features of Hold-Down Connection.

Type 3: Pillar-to-Beam connection

The timber connection between beams and pillars is a critical aspect of timber construction, as it ensures the stability and structural integrity of the entire framework. Various typologies of timber connections exist, each offering unique advantages and considerations based on the project's specific requirements. Nowadays, in timber buildings, the most popular option is the use of metal connectors, such as angle brackets or plates, which are fastened to both the beam and the pillar using bolts or screws. These metal connectors provide added strength and stability to the connection, particularly in applications where high loads or dynamic forces are anticipated. Additionally, the beam and pillar connection may display hysteresis loops with varying degrees of pinching and asymmetry. The presence of pinching indicates localized stiffness and strength degradation, while asymmetrical loop shapes may suggest uneven loading or displacement behavior within the connection. By carefully selecting the most appropriate typology of timber connection based on factors such as load requirements, architectural design, and construction methods, engineers and architects can ensure the structural reliability and longevity of timber buildings in various applications. As in the previously studied cases, some typologies of pillar-to-beam connection are illustrated to highlight the general features of their specific hysteresis loops.

The initial focus is on a beam-to-pillar connection, examined by Ajava-kom, Ng, and Ma in their research publication [7]. Conducted at the Forest Products Laboratory, University of California, Berkeley, this investigation delves into the analysis of a T-connection, considering n.20 specimens composed of two timber members connected by plywood plates. The beam and pillar elements, made from LVL, boast a square section of 89 mm, while the plywood plates, measuring 12.7 mm in thickness, are affixed to the beam and pillar using metal screws and retrofit bolts. Cyclic tests are carried out to simulate the damage accumulation and degradation of mechanical characteristics of the T-connection. The research team defines three types of cyclic excitation, although the hysteresis loop is available for only one excitation type, which is thoroughly analyzed herein. The loading protocol, depicted in Figure 2.19, prescribes a cyclic law with trailing cycles featuring decreasing amplitudes. For the study, solely cycles corresponding to the peaks of the law are considered, with the experimental hysteresis loop assuming the configuration illustrated in Figure 2.20. Throughout the loading history, the loop shape is affected by pinching and strength degradation, which is particularly noticeable during the final cycles, as underscored by the backbone curve. Examination of Figure 2.21 reveals that the limiting curves of each cycle adopt the *S3* classification, each characterized by a single inflection point. Although the shape of the limiting curves remains consistent throughout the loading history,

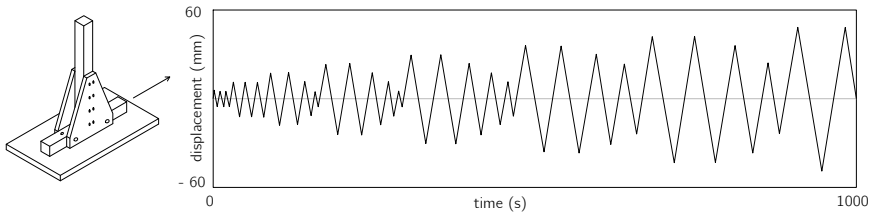
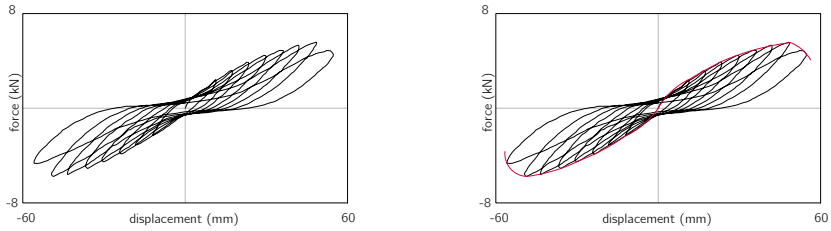


Figure 2.19. Loading protocol for shear loading on the T-connection tested by Ajavakom, Ng, and Ma in [7] and scheme of the test set-up



(a) (b)

Figure 2.20. (a) Experimental loop exhibited by the hold-down and (b) its backbone curve.

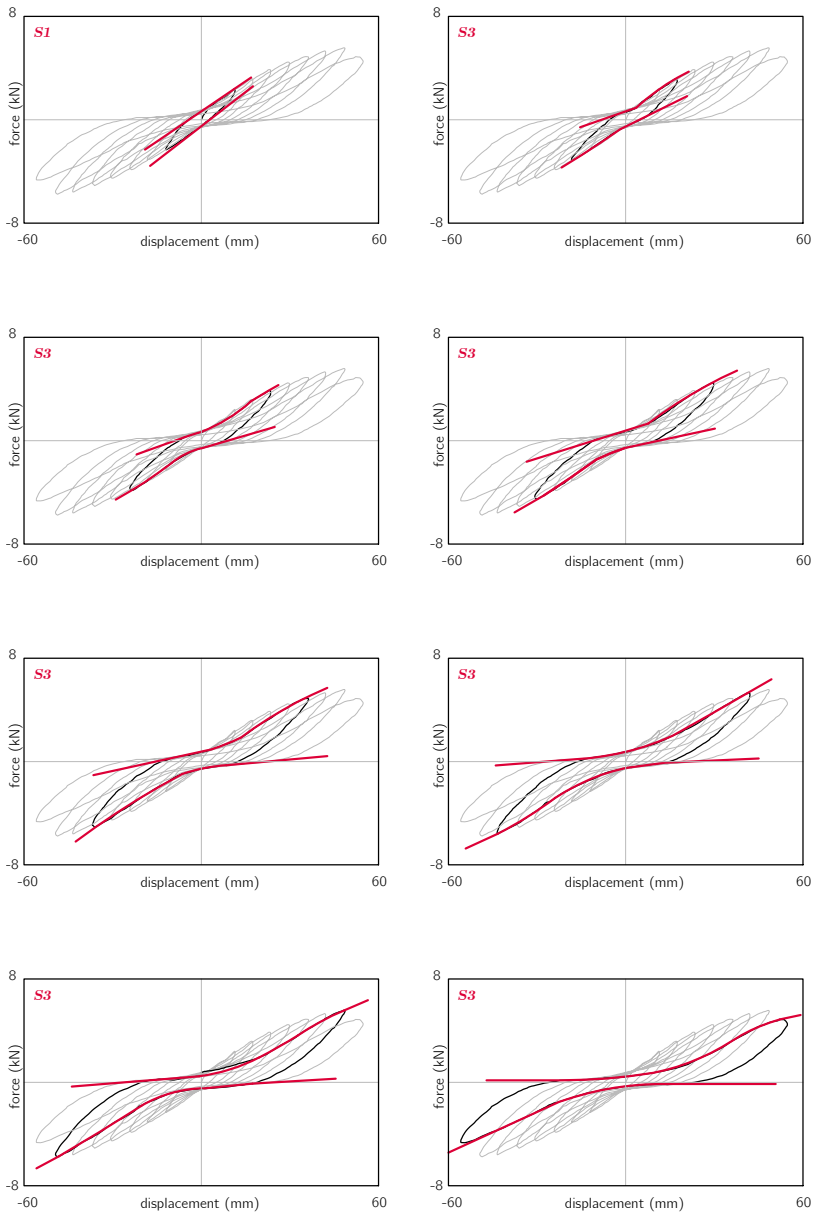


Figure 2.21. Limiting curves for each hysteresis loop

the inflection points shift while the secant stiffness diminishes. The specimen exhibits a notable decrease in resistance capacity and significant deformations throughout the test. Towards the conclusion of the examination, it demonstrates a resistance level of approximately 5 kN, accompanied by a deformation reaching up to 55 mm.

The second example of a pillar-to-beam connection is illustrated in the Master Thesis of Fairweather in [28]. The specimen consists of one continuous pillar and two beams connected to the pillar through steel brackets. Moreover, epoxy steel dowels are inserted at the end of beams and through the pillar. The section of glulam beams is 495x135 mm, the glulam pillar is 495x180 mm, and the steel brackets are 500x150 mm. The test procedure consists of a quasi-static cyclic loading, and the lateral load increases until the target is reached. As Figure 2.22 shows, the displacement increases proportionally in function of the time history. The hysteresis loop in Figure 2.23 is pinched, but nevertheless, it demonstrates a good capability to dissipate energy. In addition, the connection reaches a good resistance with 50 kN and 50 mm of deformation, with a slight strength degradation during the last cycles until the collapse occurs in metal elements. Figure 2.24 points out the pinched nature of the hysteresis loop and shows that in correspondence with the peak load, the limiting curves take the shape of the type *S3*, with one inflection point, whereas during the trailing cycles, limiting curves become of the type *S2*, losing some internal area and dissipation capacity.

In conclusion, the examples presented underline the variability in the dynamic response exhibited by beam-to-pillar connections, emphasizing the significant influence of design choices and loading protocols. Each connection configuration, characterized by distinct material compositions, fastening methods, and geometric arrangements, yields unique hysteresis loop shapes and behavioral patterns under cyclic loading conditions. Despite this inherent variability, general trends, such as those observed in preceding connection cases, can be discerned. The hysteresis loops typically exhibit characteristic features indicative of the connection's mechanical behavior, including pinching phenomena and strength degradation over successive loading cycles. These phenomena are often more pronounced in the latter stages of the test, reflecting the cumulative effects of cyclic loading on connection performance. The limiting curves of the hysteresis loop are of the type *S2* or *S3*, with one inflection point that moves during the loading history. Compared to angle brackets and hold-down, the strength and secant stiffness degradation are reduced, meaning a more constant capability in dissipating energy during the dynamic excitation, even if the final bearing capacity depends on design features.

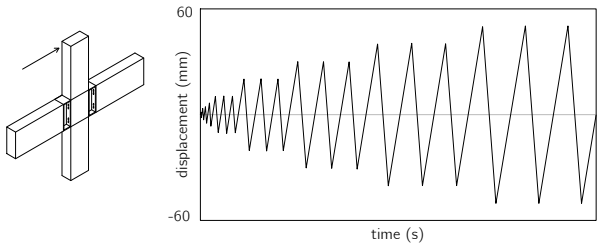
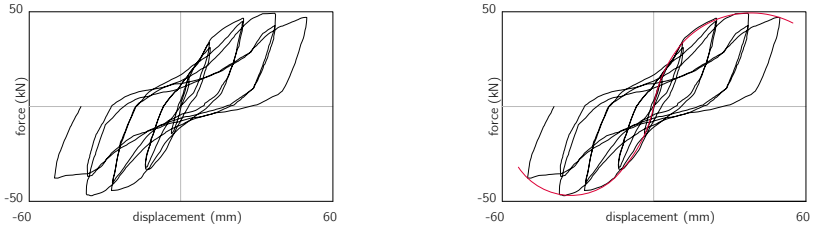


Figure 2.22. Loading protocol for shear loading on the beam-to-pillar connection tested by Fairweather in [28] and scheme of the test set-up



(a) (b)

Figure 2.23. (a) Experimental loop exhibited by the hold-down and (b) its backbone curve.

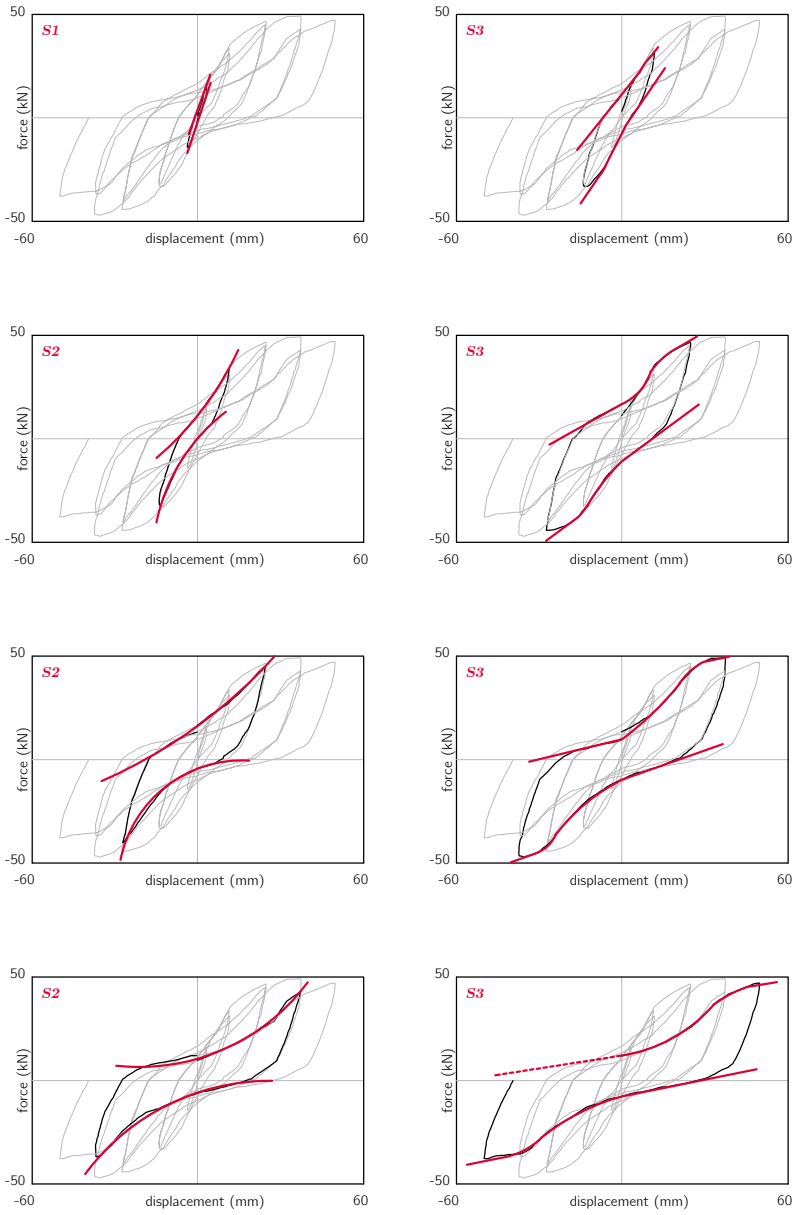


Figure 2.24. Limiting curves for each hysteresis loop

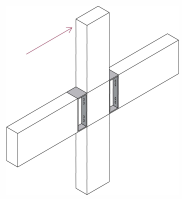
Typology of Connection	Position	Hysteresis Loop Shape
 Beam-to-Pillar	Connect beam to pillar	• Pinched loop shape • *S3* limiting curve • Shift of inflection point • During final loops: – Reduction of secant stiffness – Force degradation

Table 2.3. Features of Beam-to-Pillar Connection.

Type 4: Single – Shear Nail connection

Shear walls are structural elements commonly used in building construction to resist lateral forces, such as wind and seismic loads, and stabilize the overall structure. These walls are designed to withstand horizontal forces acting perpendicular to their plane, thereby preventing excessive building sway and ensuring structural integrity during adverse environmental conditions. They typically comprise vertical timber panels securely attached to the building's framing system. The panels may be made of plywood, oriented strand board (OSB), or other engineered wood products, offering high strength and stiffness properties necessary for resisting lateral loads. The effectiveness of shear walls in resisting lateral forces primarily depends on their capacity to transfer these loads from the building's roof and floors down to the foundation. This is achieved through the shear resistance provided by the interconnected timber panels and framing members and the anchorage and fastening systems used to secure them.

Single-shear nail connections play an essential role in shear wall construction, as they are used to join the sheathing panels to the framing members and connect each panel. Single-shear nail connections can vary in their orientation, with nails being driven perpendicular or inclined to the timber members they are joining. In perpendicular nail connections, nails are typically driven straight through the thickness of one timber member and into another, forming a direct and efficient

bond. This configuration is commonly used in applications where simplicity and ease of installation are paramount, such as in basic timber framing or light-duty construction. On the other hand, inclined nail connections involve driving nails at an angle through one timber member and into another, creating a more complex and robust bond. This orientation increases the resistance to withdrawal forces and can enhance load-carrying capacity, making it suitable for applications requiring greater structural integrity, such as in shear walls or heavy-duty timber structures. Both perpendicular and inclined nail connections have their respective advantages and limitations, and the choice between them depends on factors such as specific structural requirements.

This section will show the characteristics of two connections with perpendicular nails and discuss their behavior when subjected to dynamic loading.

The first sample taken into consideration is analyzed by Hyungsuk Lim in his PhD Thesis [41]. The experimental campaign is carried out at the University of British Columbia on test specimens made of 105x105 mm composite strand-based wood and a panel of OBS 11 mm thicker. The two elements are connected with a unique CN50 nail. Cyclic tests are performed according to the CUREE Basic Loading Protocol [6], which defines one principle cycle and multiple trailing cycles, as shown in Figure 2.25. In the configuration considered, the nail is driven into the edge side of the composite member and loaded parallel to the direction of the grain. The resulting hysteresis loop in Figure 2.26 shows a significant pinched shape since the first cycles. The backbone curve highlights the strength degradation during the last primary cycles, reaching the nail pull-out around 22 mm. Moreover, it is possible to see a strength degradation also for trailing cycles, which increases during the loading history. Considering only primary cycles, limiting curves (Figure 2.27) are of the type *S3* and have one inflection point that moves for each cycle, while limiting curves of trailing cycles are curves of the type *S2*.

The second sample of a single-share nail connection considered is tested by Dong et al. in [26]. Each specimen realized is characterized by an OSB panel 9.5 mm thicker connected through n.2 nails of 3.8 mm to a lumber element of dimension 38 mm x 89 mm. Cyclic tests follow the CUREE loading protocol in ASTM-2126 [6], as illustrated in Figure 2.28, and the loading law is characterized by increasing amplitudes and trailing secondary cycles. Since the beginning of the test, the hysteresis loop is strongly pinched, with a strength and secant stiffness degradation in the last cycle of the loading history. This last behavior is more emphasized for the trailing cycles, as shown in Figure 2.29. As in the previous case, the shape of the limiting curves for principal cycles is of the type *S3*, with one inflection point that moves during the loading history, while secondary cycles have a *S2* shape.

In conclusion, despite variations in design parameters such as geometry, ma-

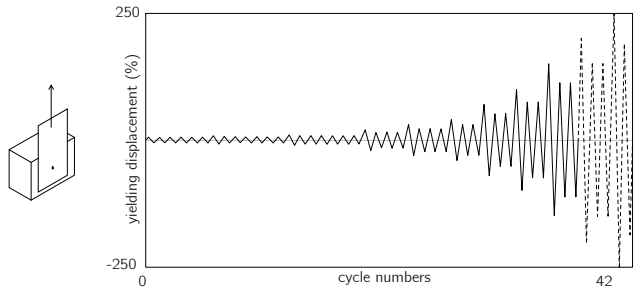
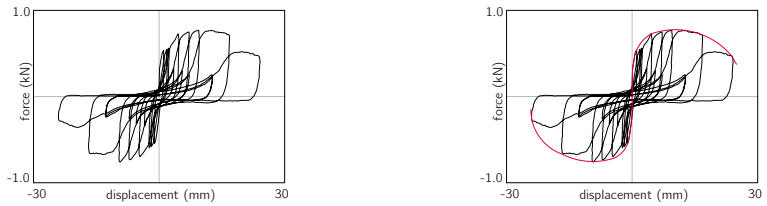


Figure 2.25. Loading protocol for shear loading on the Single-share nail connection tested by Lim in [41] and scheme of the test set-up



(a) (b)

Figure 2.26. (a) Experimental loop exhibited by the hold-down and (b) its backbone curve.

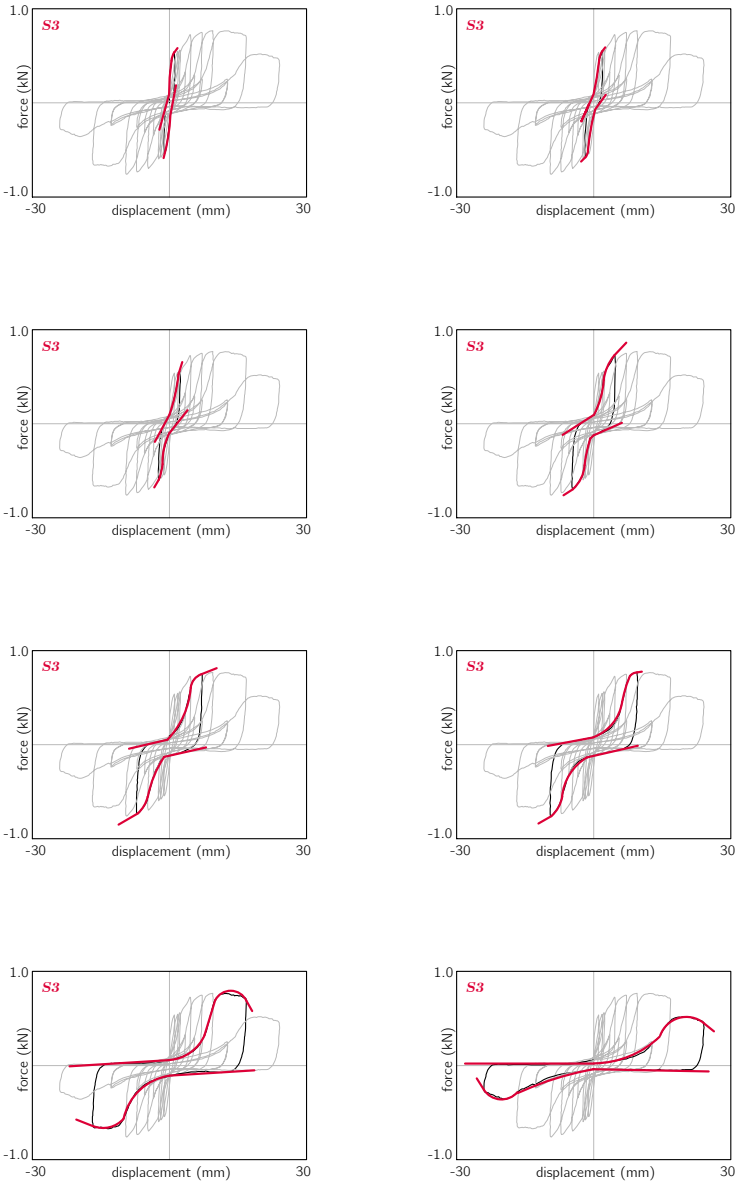


Figure 2.27. Limiting curves for each hysteresis loop

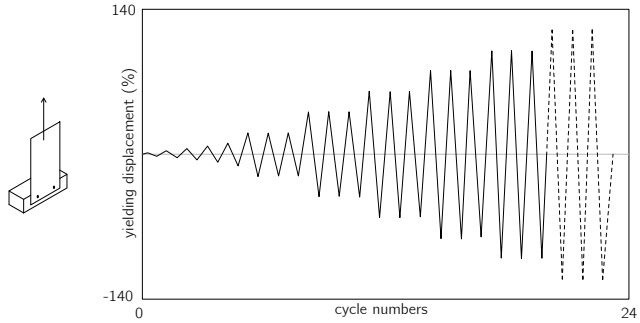
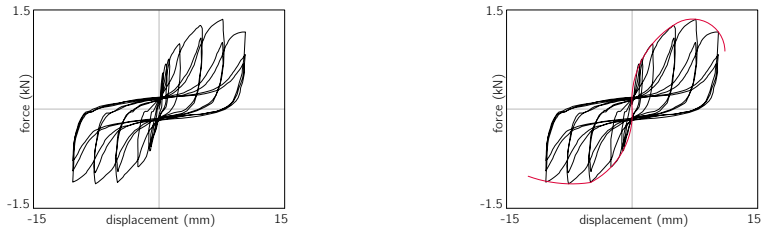


Figure 2.28. Loading protocol for shear loading on the Single-share nail connection tested by Dong et al. in [26] and scheme of the test set-up



(a) (b)

Figure 2.29. (a) Experimental loop exhibited by the hold-down and (b) its backbone curve.

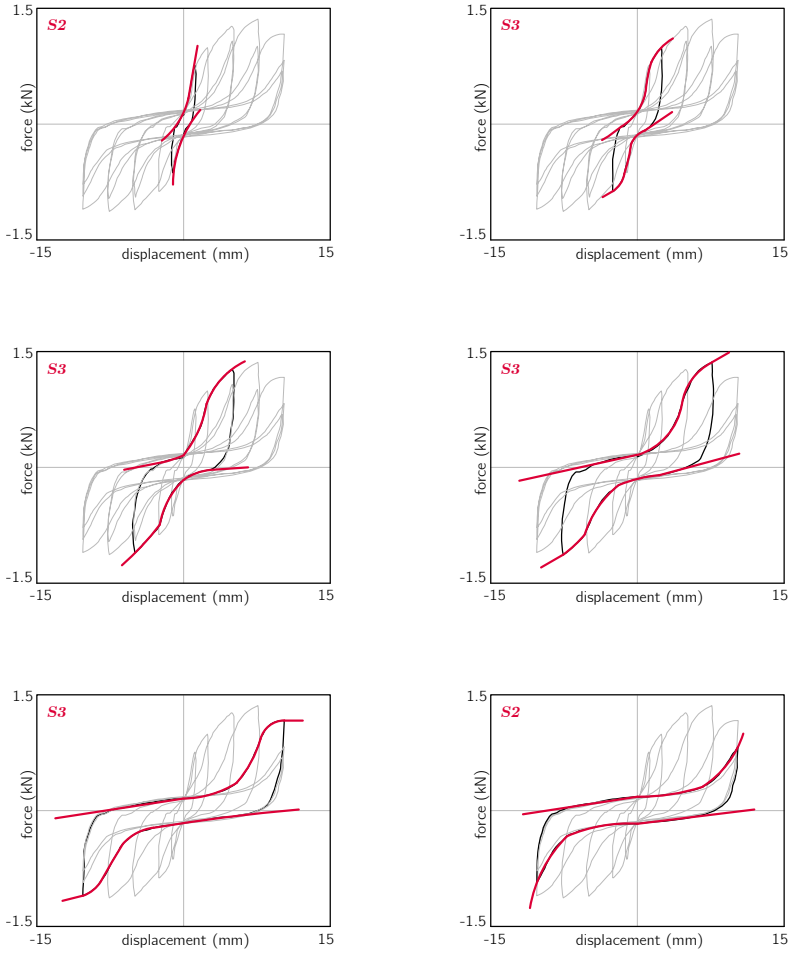


Figure 2.30. Limiting curves for each hysteresis loop

terial, and nail quantity, the uniform behavior observed in single-shear nail connections underscores their fundamental role as the basic elements of shear walls in timber construction. While other connection typologies explored in this chapter, such as hold-downs, angle brackets, and beam-to-pillar connections, may exhibit higher carrying capacities and more complex behaviors, single-shear nail connections remain indispensable components in shear wall assemblies. The inherent simplicity of single-shear nail connections belies their critical function in distributing lateral forces and ensuring the structural integrity of timber buildings. However, this simplicity also implies that the performance of shear walls, and consequently the overall dynamic behavior of the structure, is heavily influenced by the composition and configuration of these connections.

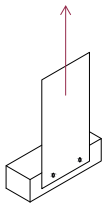
Typology of Connection	**Position**	**Hysteresis Loop Shape**
 Single – Shear Nail connection	Connect single panels to each other	• Pronounced pinched loop shape • *S2* and *S3* limiting curve • Shift of inflection point • During final loops: – Reduction of secant stiffness – Reduction of loop area – Force degradation

Table 2.4. Features of Single Shear Nail Connection.

2.5 Conclusion of Chapter 2

This chapter examined timber as a building material, discussing the different typologies of structures used, with a specific focus on the dynamic behavior of key timber connections under seismic loads, drawing insights from experimental hysteresis loops in the literature. The connection typologies considered are angle brackets, hold-downs, beam-to-pillar connections, and single-shear nail connections. The study of experimental hysteresis loops revealed key insights into the energy dissipation and strength characteristics of different connection types.

Angle bracket connections show significant pinching and gradual strength and stiffness degradation, influenced by geometry and fastener details. Their limiting curves evolve from *S2* to more complex shapes with one of two inflection points before degrading back, reflecting reduced energy dissipation capacity.

Hold-down connections exhibit more stable performance, with minimal pinching and strength loss. Factors like connection geometry and loading protocol shape their response, with limiting curves shifting during testing but generally maintaining robustness.

Beam-to-pillar connections display variability based on design, but trends like moderate pinching and consistent energy dissipation are evident. Limiting curves are typically *S2* or *S3*, ensuring reliable performance despite loading cycles.

Single-shear nail connections, while simpler, are critical in shear wall assemblies for distributing lateral forces with less resistance when confronted with other typologies. Their uniform behavior emphasizes their role in maintaining structural integrity.

In summary, the chapter underscored the importance of connection design in energy dissipation and structural stability, which is crucial for enhancing timber buildings' seismic resilience.

Chapter 3

The Vaiana-Rosati Hysteretic Model

3.1 Summary of Chapter 3

The hysteresis behavior of structures is often modeled by researchers using mathematical frameworks that provide insights into the mechanical properties of the system during loading cycles. When it comes to timber connections, several hysteresis models, such as the Bouc-Wen Model and the Dolan Model, have been developed to replicate their complex behavior. However, these models exhibit limitations, particularly regarding the interpretation of parameters and their ability to simulate asymmetric cycles with degradation and pinching effects.

This chapter introduces the Vaiana-Rosati Model (VRM), a novel hysteresis model designed to overcome these challenges and enable the accurate simulation of intricate hysteretic loop shapes. The VRM will be presented in both its analytical and differential formulations, offering flexibility in application depending on the specific analysis requirements.

Following the model presentation, a sensitivity analysis of the VRM parameters will be performed, facilitating manual calibration of the model. The chapter then discusses parameter identification using optimization techniques, such as the Genetic Algorithm (GA) and the *fminsearch* algorithm. These methods will be employed to fine-tune the model for better accuracy. The comparison of simulations based on these optimization techniques highlights the efficiency and reliability of the genetic algorithm in achieving superior results in reproducing experimental hysteresis loops.

3.2 Introduction

Researchers have developed several models to capture the complex hysteretic loop shapes exhibited by various materials and mechanical systems, including timber connections. The Bouc-Wen Model and the Dolan Model have been widely used in the scientific literature to simulate timber connections and other structural elements under cyclic loading.

The Bouc-Wen Model (BWM) [12, 13, 70] is one of the most commonly used hysteresis models due to its flexibility in representing various types of hysteretic behaviors, including smooth transitions between elastic and plastic deformations. Thanks to the modified version suggested by Baber and Wen [10] and then Barber and Noori [9, 11], the model can also simulate strength, stiffness, and pinching degradation effects. The BWM is characterized by a set of parameters that control the loop's shape, size, and pinching effect, making it versatile for different materials, including timber. The generalized force f is considered as a sum of a linear elastic force f_e and a rate-independent hysteretic force f_h:

$$f(u,z) = f_e(u) + f_h(z) = \alpha k u + (1-\alpha) k u \tag{3.1}$$

where u is the generalized displacement and z is the internal variable, determined by solving the followed first-order nonlinear Ordinary Differential Equation (ODE):

$$\dot{z} = \Psi(z) \frac{A - |z|^n [\beta \mathrm{sgn}(\dot{u} z) + \gamma] \nu}{\eta} \dot{u}, \tag{3.2}$$

where $\Psi(z)$ is the pinching function, a positive bell-shaped function that takes values from 0 to 1, when z moves from $z = 0$ to $z \to \pm\infty$

$$\Psi(z) = 1 - \zeta_1 \exp\left(-\frac{z^2}{2\zeta_2^2}\right). \tag{3.3}$$

ζ_1 is a parameter that affects the intensity of pinching. Moreover, ζ_2 controls the distribution of pinching. Both parameters are nonlinear functions of the generalized hysteretic energy e.

However, despite its adaptability, one of the challenges with the Bouc-Wen model is its complexity, particularly when applied to highly non-linear phenomena like stiffness degradation or pinching in timber connections. Its differential formulation can also complicate the integration into standard structural analysis software, limiting its use in some practical applications.

On the other hand, the Dolan Model [25] was specifically developed to model the hysteretic behavior of wood connections. Dolan's model incorporates fewer parameters and focuses on capturing the stiffness degradation and pinching effects typical in timber structures. While it offers a simpler approach compared to

the Bouc-Wen model, the Dolan Model can sometimes struggle with more complex hysteresis shapes, particularly when dealing with highly asymmetric loops or systems with pronounced pinching effects. The Dolan Model is a finite element approach, described by two exponential-type functions that can be solved in closed form. The first function, $F(u)$, represents the envelope curve, which encloses all the points of maximum force and displacement reached at each load cycle by the timber joint:

$$F(u) = (\mathrm{sgn}P_0 + k_2)\left(1 - \exp\left(-\frac{k_0 u}{\mathrm{sgn}P_0}\right)\right)$$

where P_0 is the Y-intercept of the k_2 line, k_0 is the slope of the curve at the origin, and k_2 is the slope of the curve at the maximum displacement. The second function, $f(u)$, describes each cycle's hysteretic behavior. It is characterized by four different curves depending on whether the connection is in a loading or unloading phase:

$$f(u) = \mathrm{sgn}P_1 + k_4 u + \left(\exp a_{(1-4)}|u| - 1\right)$$

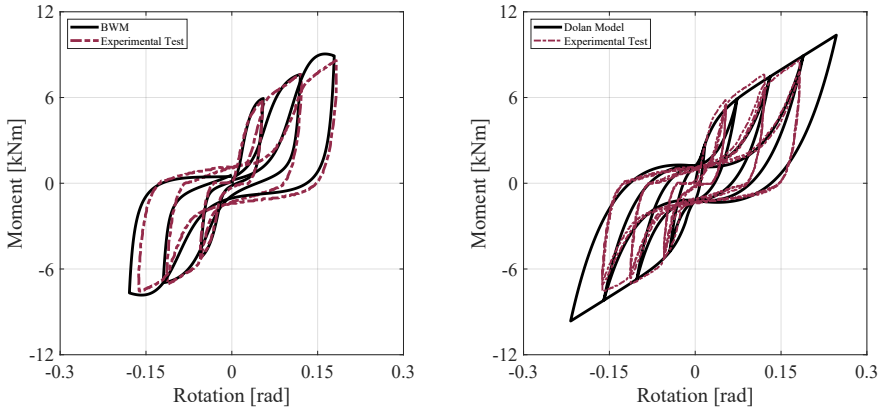
$$a_{(1-4)} = \frac{\log(\mathrm{sgn}F_{(1,2)} + \mathrm{sgn}P_1 - k_4 u_{(1,2)} + 1)}{|u_{(1,2)}|}$$

where P_1 is the load at zero deflection, k_4 is the slope at zero deflection, $u_{(1,2)}$ is the maximum and minimum deflections, and $F_{(1,2)}$ is the maximum and minimum loads.

To evaluate the efficiency of the Bouc-Wen Model and Dolan Model in simulating complex hysteretic loops, the experimental test conducted by Yang et al. in [72] on an L-shaped double-shear beam-to-column Glulam joint is considered and simulated. Figure 3.1 compares the performance of the manually calibrated Bouc-Wen Model and Dolan Model in simulating the hysteresis loop of a timber connection. Both models were calibrated to fit the experimental data, but their limitations in capturing key hysteretic features are evident. The Bouc-Wen Model, shown in Figure 3.1(a), can generally represent hysteretic behavior but struggles with the pronounced pinching effect and the asymmetric loop shape observed in the experimental data. On the other hand, the Dolan Model, shown in Figure 3.1(b), provides a simpler simulation but fails to accurately replicate stiffness degradation and shifting inflection points, which are evident in the experimental loops.

In summary, traditional hysteretic models, such as the Bouc-Wen and Dolan Models, have several notable limitations:

- difficulty in associating parameters with clear physical and geometrical meanings;



(a) (b)

Figure 3.1. Simulation of the experimental hysteresis loop of a timber connection tested by Yang et al. [72], using: (a) the Bouc-Wen Model and (b) the Dolan Model.

- inability to accurately describe the complex behavior of real timber joints;
- challenges in manual calibration of the hysteretic models;
- limited ability to simulate asymmetrical hysteresis cycles, with degradation and pinching.

Building on the strengths of these models, the Vaiana-Rosati Model (VRM) was introduced to address some of their limitations. Derived from an existing class of uniaxial phenomenological models [65, 67, 66, 68, 61], the VRM provides a simplified yet effective approach to simulate complex hysteretic behaviors, particularly in timber connections. Notably, the VRM offers several advantages over the Bouc-Wen and Dolan models. Firstly, the VRM facilitates the computation of generalized hysteretic force, tangent stiffness, and work done during the hysteresis loop in closed form, providing more direct insight into the underlying mechanics of the system. Additionally, it allows for the independent simulation of both the loading and unloading phases using a set of eight model parameters, which makes it particularly well-suited for simulating asymmetric or pinched hysteretic loops commonly observed in timber connections. Moreover, the clear physical and geometric interpretations of these parameters enhance the model's comprehensibility and applicability in engineering practice. Lastly, the VRM's

mathematical formulation is designed to be easily implemented in computational tools, encouraging its adoption in real-world applications.

The VRM is available in two formulations: an analytical version, presented in both its original and reformulated forms, and a differential version. These formulations offer flexibility in modeling and simulation, allowing researchers and engineers to choose the approach that best fits their analytical and computational needs. By leveraging the capabilities of the VRM, structural engineers can more accurately simulate and analyze the dynamic behavior of timber connections, contributing to the advancement of seismic design and performance evaluation methodologies in timber structures.

3.3 The Analytical Formulation of the Vaiana-Rosati Model

3.3.1 VRM: reformulated version (VRM+A)

The reformulated Vaiana-Rosati Model, introduced in a recent paper [62], represents a significant advancement in the field of hysteretic modeling. This updated version offers multiple enhancements that simplify the utilization of closed-form expressions and extend their applicability in design processes, all while reducing complexity. One notable improvement is the description of the hysteretic loop using only two curves: the generalized loading curve f^+ and the generalized unloading curve f^-. These curves capture the essential behavior of the system during both the loading and unloading phases, providing a concise yet comprehensive representation of the hysteresis loop. Another key feature of the reformulated model is the introduction of upper and lower limit curves, denoted as c_u and c_l respectively, as shown in Figure 3.2. These curves represent the asymptotes of the generalized loading and unloading curves, eliminating the need for internal variables and further simplifying the model formulation. With these advancements, the generalized force f becomes a function of displacement u and the coordinates of a generic point $P(u_P, f_P)$. This simplification enhances the model's versatility and ease of use, making it more accessible to practitioners and researchers alike.

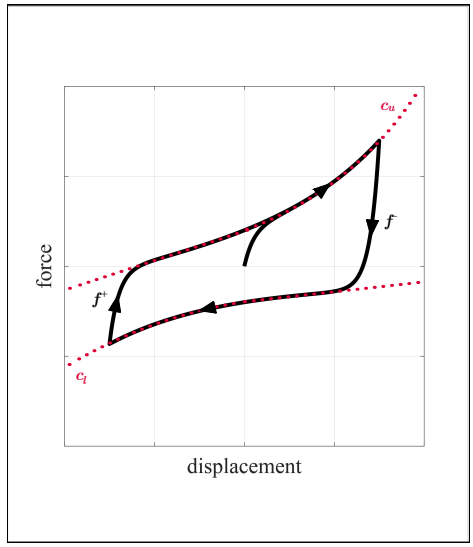


Figure 3.2. Generalized loading f^+ and unloading curves f^-, upper and lower limit curves c_u and c_l.

Generalized force

The novel expression of the generalized loading force f^+ depends on the formulation of the upper limit curve c_u, which can written as follows:

$$\begin{aligned} c^+(u, u_P, f_P) =& f_e^+(u) + k_b^+ u + f_0^+ - \frac{1}{\alpha^+}\left\{\left[+\alpha^+\left(f_e^+(u_P)\right.\right.\right. \\ &+ k_b^+ u_P + f_0^+ + \frac{\delta_k^+}{\alpha^+} - f_P e^{-\alpha^+(u-u_P)} - \delta_k^+. \end{aligned} \tag{3.4}$$

where:

$$f_e^+(u) = \beta_1^+ e^{\beta_2^+ u} - \beta_1^+ + \frac{4\gamma_1^+}{1 + e^{-\gamma_2^+(u-\gamma_3^+)}} - 2\gamma_1^+. \tag{3.5}$$

To obtain the expression of the generalized loading force f^+, we need to impose δ_k^+ zero, and then:

$$\begin{aligned} f^+(u, u_P, f_P) =& f_e^+(u) + k_b^+ u + f_0^+ \\ &- \left(f_e^+(u_P) + k_b^+ u_P + f_0^+ - f_P\right) e^{-\alpha^+(u-u_P)}, \end{aligned} \tag{3.6}$$

and considering the expression of f_e^+ in 3.5, the equation 3.6 becomes:

$$\begin{aligned} f^+(u,u_P,f_P) = &\beta_1^+ e^{\beta_2^+ u} - \beta_1^+ + \frac{4\gamma_1^+}{1+e^{-\gamma_2^+(u-\gamma_3^+)}} - 2\gamma_1^+ + k_b^+ u + f_0^+ \\ &- \Big[\beta_1^+ e^{\beta_2^+ u_P} - \beta_1^+ + \frac{4\gamma_1^+}{1+e^{-\gamma_2^+(u_P-\gamma_3^+)}} \\ &- 2\gamma_1^+ + k_b^+ u_P + f_0^+ - f_P\Big]\, e^{-\alpha^+(u-u_P)}. \end{aligned} \tag{3.7}$$

As anticipated above, the expression of f^+ is a function of u and the coordination of a generic point $P(u_P, f_P)$, which can be the initial point of f^+. Moreover, the curve f^+ reaches asymptotically the upper limit curve c_u and, for this reason, the equation 3.7 can be written as:

$$\begin{aligned} f^+(u,u_P,f_P) &= c_u(u) - \left(f_e^+(u_P) + k_b^+ u_P + f_0^+ - f_P\right) e^{-\alpha^+(u-u_P)} \\ &= c_u(u) + r^+(u,u_P,f_P), \end{aligned} \tag{3.8}$$

with:

$$\lim_{u\to+\infty} r^+(u,u_P,f_P) = 0. \tag{3.9}$$

Considerations for the generalized loading curve f^+ are valid for the generalized unloading curve f^-. In this case, the lower limiting curve c_l can take the form of:

$$\begin{aligned} c^-(u,u_P,f_P) = &f_e^-(u) + k_b^- u + f_0^- - \frac{1}{\alpha^-}\left\{\left[+\alpha^-\left(f_e^-(u_P)\right.\right.\right. \\ &+ k_b^- u_P + f_0^- + \frac{\delta_k^-}{\alpha^-} - f_P e^{-\alpha^-(u-u_P)} - \delta_k^-. \end{aligned} \tag{3.10}$$

where:

$$f_e^-(u) = \beta_1^- e^{\beta_2^- u} - \beta_1^- + \frac{4\gamma_1^-}{1+e^{-\gamma_2^-(u-\gamma_3^-)}} - 2\gamma_1^-. \tag{3.11}$$

Setting δ_k^- null, the expression of the generalized unloading force f^- becomes:

$$\begin{aligned} f^-(u,u_P,f_P) = &f_e^-(u) + k_b^- u + f_0^- \\ &- \left(f_e^-(u_P) + k_b^- u_P + f_0^- - f_P\right) e^{-\alpha^-(u-u_P)}, \end{aligned} \tag{3.12}$$

and using the equation of f_e^- in 3.11, the expression 3.12 can be rewritten:

$$\begin{aligned} f^-(u,u_P,f_P) = {} & \beta_1^- e^{\beta_2^- u} - \beta_1^- + \frac{4\gamma_1^-}{1+e^{-\gamma_2^-(u-\gamma_3^-)}} - 2\gamma_1^- + k_b^- u + f_0^- \\ & - \left[\beta_1^- e^{\beta_2^- u_P} - \beta_1^- + \frac{4\gamma_1^-}{1+e^{-\gamma_2^-(u_P-\gamma_3^-)}}\right. \\ & \left. - 2\gamma_1^- + k_b^- u_P + f_0^- - f_P\right] e^{-\alpha^-(u-u_P)}. \end{aligned} \tag{3.13}$$

It is possible to notice that the expression of f^- is a function of u, and the coordination of a generic point $P(u_P, f_P)$, for simplicity, can be the initial point of f^-. As in the previous case, the curve f^- reaches asymptotically the lower limit curve c_l and the equation 3.13 take this form:

$$\begin{aligned} f^-(u,u_P,f_P) &= c_l(u) - \left(f_e^-(u_P) + k_b^- u_P + f_0^- - f_P\right) e^{-\alpha^-(u-u_P)} \\ &= c_l(u) + r^-(u,u_P,f_P), \end{aligned} \tag{3.14}$$

with:

$$\lim_{u\to-\infty} r^-(u,u_P,f_P) = 0. \tag{3.15}$$

Generalized tangent stiffness

During the generalized loading phase, when the velocity is positive, the generalized tangent stiffness k_t^+ is the first derivative of the generalized force f^+, and that is:

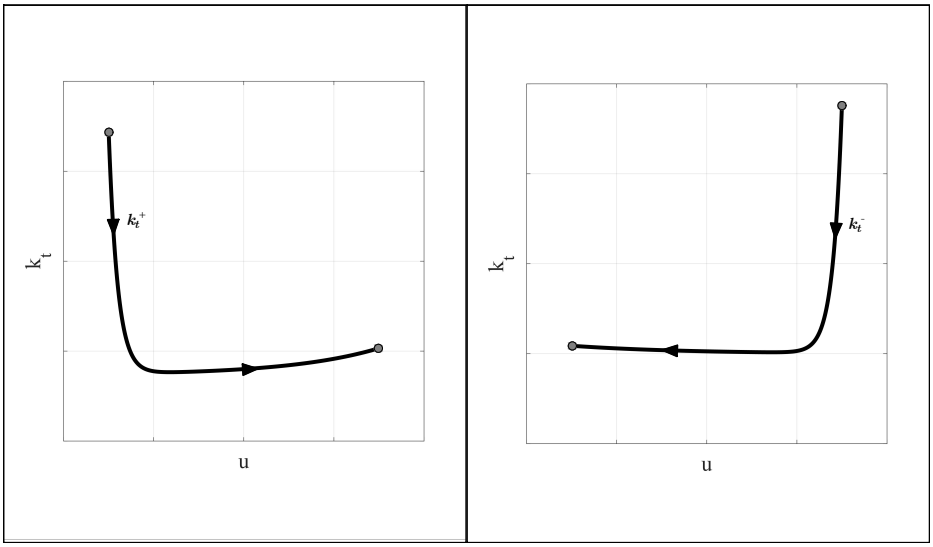
$$k_t^+(u,u_P,f_P) = \frac{d}{du} f^+(u,u_P,f_P). \tag{3.16}$$

Using the formulation of f^+ in 3.6, the generalized tangent stiffness becomes:

$$k_t^+(u,u_P,f_P) = k_e^+(u) + k_b^+ + \alpha^+\left(f_e^+(u_P) + k_b^+ u_P + f_0^+ - f_P\right) e^{-\alpha^+(u-u_P)}, \tag{3.17}$$

with:

$$k_e^+(u) = \frac{d}{du} f_e^+(u) = \beta_1^+\beta_2^+ e^{\beta_2^+ u} + \frac{4\gamma_1^+\gamma_2^+ e^{-\gamma_2^+(u-\gamma_3^+)}}{\left[1+e^{-\gamma_2^+(u-\gamma_3^+)}\right]^2}. \tag{3.18}$$



(a) (b)

Figure 3.3. Illustration of the generalized tangent stiffness function k_t corresponding to the loading (a) and unloading (b) phases of the hysteresis loop shown in Figure 3.2.

By considering the equation of f_e^+ in 3.5, the expression 3.17 can be written as:

$$\begin{aligned} k_t^+(u, u_P, f_P) = {} & \beta_1^+ \beta_2^+ e^{\beta_2^+ u} + \frac{4\gamma_1^+ \gamma_2^+ e^{-\gamma_2^+(u-\gamma_3^+)}}{\left[1 + e^{-\gamma_2^+(u-\gamma_3^+)}\right]^2} + k_b^+ \\ & + \alpha^+ \left[\beta_1^+ e^{\beta_2^+ u_P} - \beta_1^+ + \frac{4\gamma_1^+}{1 + e^{-\gamma_2^+(u_P-\gamma_3^+)}}\right. \\ & \left. - 2\gamma_1^+ + k_b^+ u_P + f_0^+ - f_P\right] e^{-\alpha^+(u-u_P)}. \end{aligned} \tag{3.19}$$

Similarly, during the unloading phase, when the velocity is negative, the generalized tangent stiffness k_t^- is the first derivative of the generalized force f^- and can be computed as:

$$k_t^-(u, u_P, f_P) = \frac{d}{du} f^-(u, u_P, f_P). \tag{3.20}$$

Adopting the formulation of f^- in 3.12, the generalized tangent stiffness becomes:

$$k_t^-(u, u_P, f_P) = k_e^-(u) + k_b^- + \alpha^- \left(f_e^-(u_P) + k_b^- u_P + f_0^- - f_P\right) e^{-\alpha^-(u-u_P)}, \tag{3.21}$$

where:

$$k_e^-(u) = \frac{d}{du} f_e^-(u) = \beta_1^- \beta_2^- e^{\beta_2^- u} + \frac{4\gamma_1^- \gamma_2^- e^{-\gamma_2^-\left(u-\gamma_3^-\right)}}{\left[1 + e^{-\gamma_2^-\left(u-\gamma_3^-\right)}\right]^2}. \tag{3.22}$$

Invoking the equation of f_e^- in 3.11, the expression 3.21 can be written as:

$$\begin{aligned} k_t^-(u, u_P, f_P) = {} & \beta_1^- \beta_2^- e^{\beta_2^- u} + \frac{4\gamma_1^- \gamma_2^- e^{-\gamma_2^-\left(u-\gamma_3^-\right)}}{\left[1 + e^{-\gamma_2^-\left(u-\gamma_3^-\right)}\right]^2} + k_b^- \\ & + \alpha^- \left[\beta_1^- e^{\beta_2^- u_P} - \beta_1^- + \frac{4\gamma_1^-}{1 + e^{-\gamma_2^-\left(u_P-\gamma_3^-\right)}}\right. \\ & \left. - 2\gamma_1^- + k_b^- u_P + f_0^- - f_P\right] e^{-\alpha^-(u-u_P)}. \end{aligned} \tag{3.23}$$

The illustration in Figure 3.3a (b) shows the generalized tangent stiffness during the loading (unloading) phase related to the generic hysteresis loop illustrated in Figure 3.2. In particular, it can be observed that the curve of the tangent stiffness function is continuous without interruptions due to internal variables.

Generalized work

The formulation of the generalized work W^+ performed by the generalized force f^+ over a specified generalized displacement interval $[u_i, u_f]$ during a loading phase ($\dot{u} > 0$) is derived from Equation 3.7, which can be expressed as follows:

$$f^+(u, u_P, f_P) = f_a^+(u) + f_b^+(u) + f_c^+(u) + f_d^+(u, u_P, f_P), \tag{3.24}$$

where:

$$f_a^+(u) = \beta_1^+ e^{\beta_2^+ u} - \beta_1^+, \tag{3.25a}$$

$$f_b^+(u) = \frac{4\gamma_1^+}{1 + e^{-\gamma_2^+\left(u-\gamma_3^+\right)}} - 2\gamma_1^+, \tag{3.25b}$$

$$f_c^+(u) = k_b^+ u + f_0^+, \tag{3.25c}$$

$$\begin{aligned} f_d^+(u, u_P, f_P) = {} & -\left[\beta_1^+ e^{\beta_2^+ u_P} - \beta_1^+ + \frac{4\gamma_1^+}{1 + e^{-\gamma_2^+\left(u_P-\gamma_3^+\right)}}\right. \\ & \left. -2\gamma_1^+ + k_b^+ u_P + f_0^+ - f_P\right] e^{-\alpha^+(u-u_P)}. \end{aligned} \tag{3.25d}$$

By integrating the function of W^+ over the interval of the generic displacement $[u_i, u_f]$, we have:

$$\begin{aligned} W^+(u_i, u_f, u_P, f_P) &= \int_{u_i}^{u_f} f^+(u, u_P, f_P)\, du \\ &= \int_{u_i}^{u_f} \left(f_a^+(u) + f_b^+(u) + f_c^+(u)\right. \\ &\quad \left. + f_d^+(u, u_P, f_P)\, du = \right. \\ &= W_a^+(u_i, u_f) + W_b^+(u_i, u_f) + W_c^+(u_i, u_f) \\ &\quad + W_d^+(u_i, u_f, u_P, f_P), \end{aligned} \tag{3.26}$$

where the terms W_a^+, W_b^+, W_c^+ are taken from the first version of the Vaiana-Rosati Analytical Model, published in [60], and they are computed as follows:

$$W_a^+(u_i, u_f) = \frac{\beta_1^+}{\beta_2^+}\left(e^{\beta_2^+ u_f} - e^{\beta_2^+ u_i}\right) - \beta_1^+(u_f - u_i), \tag{3.27a}$$

$$\begin{aligned} W_b^+(u_i, u_f) = 2\gamma_1^+ \Bigg\{ & \frac{2\ln\left[e^{-\gamma_2^+(u_f - \gamma_3^+)} + 1\right]}{\gamma_2^+} \\ & - \frac{2\ln\left[e^{-\gamma_2^+(u_i - \gamma_3^+)} + 1\right]}{\gamma_2^+} + (u_f - u_i) \Bigg\}, \end{aligned} \tag{3.27b}$$

$$W_c^+(u_i, u_f) = \frac{k_b^+}{2}(u_f^2 - u_i^2) + f_0^+(u_f - u_i), \tag{3.27c}$$

Whereas, the term W_d^+ can be evaluated by:

$$\begin{aligned} W_d^+(u_i, u_f, u_P, f_P) = + \frac{1}{\alpha^+} \Bigg[& \beta_1^+ e^{\beta_2^+ u_P} - \beta_1^+ + \frac{4\gamma_1^+}{1 + e^{-\gamma_2^+(u_P - \gamma_3^+)}} \\ & -2\gamma_1^+ + k_b^+ u_P + f_0^+ - f_P \\ & \times \left[e^{-\alpha^+(u_f - u_P)} - e^{-\alpha^+(u_i - u_P)}\right]. \end{aligned} \tag{3.28}$$

In the same way, the expression of the generalized work W^- done by the negative generalized force f^- over the generic displacement interval $[u_i, u_f]$ during a unloading phase ($\dot{u} < 0$) is derived from Equation 3.13, considering:

$$f^-(u, u_P, f_P) = f_a^-(u) + f_b^-(u) + f_c^-(u) + f_d^-(u, u_P, f_P), \tag{3.29}$$

where:

$$f_a^-(u) = \beta_1^- e^{\beta_2^- u} - \beta_1^-, \tag{3.30a}$$

$$f_b^-(u) = \frac{4\gamma_1^-}{1 + e^{-\gamma_2^-(u-\gamma_3^-)}} - 2\gamma_1^-, \tag{3.30b}$$

$$f_c^-(u) = k_b^- u + f_0^-, \tag{3.30c}$$

$$\begin{aligned} f_d^-(u, u_P, f_P) = -\Bigg[&\beta_1^- e^{\beta_2^- u_P} - \beta_1^- + \frac{4\gamma_1^-}{1 + e^{-\gamma_2^-(u_P-\gamma_3^-)}} \\ &-2\gamma_1^- + k_b^- u_P + f_0^- - f_P\Bigg] e^{-\alpha^-(u-u_P)}. \end{aligned} \tag{3.30d}$$

Then, the integration of f^- over the displacement interval $[u_i, u_f]$ can give the value of the generalized work W^-, in terms of:

$$\begin{aligned} W^-(u_i, u_f, u_P, f_P) &= \int_{u_i}^{u_f} f^-(u, u_P, f_P)\, du \\ &= \int_{u_i}^{u_f} \left(f_a^-(u) + f_b^-(u) + f_c^-(u)\right. \\ &\quad \left. + f_d^-(u, u_P, f_P)\right) du = \\ &= W_a^-(u_i, u_f) + W_b^-(u_i, u_f) + W_c^-(u_i, u_f) \\ &\quad + W_d^-(u_i, u_f, u_P, f_P), \end{aligned} \tag{3.31}$$

where the terms W_a^-, W_b^-, W_c^- derive from the first version of the Vaiana-Rosati Analytical Model, published in [60], and they are:

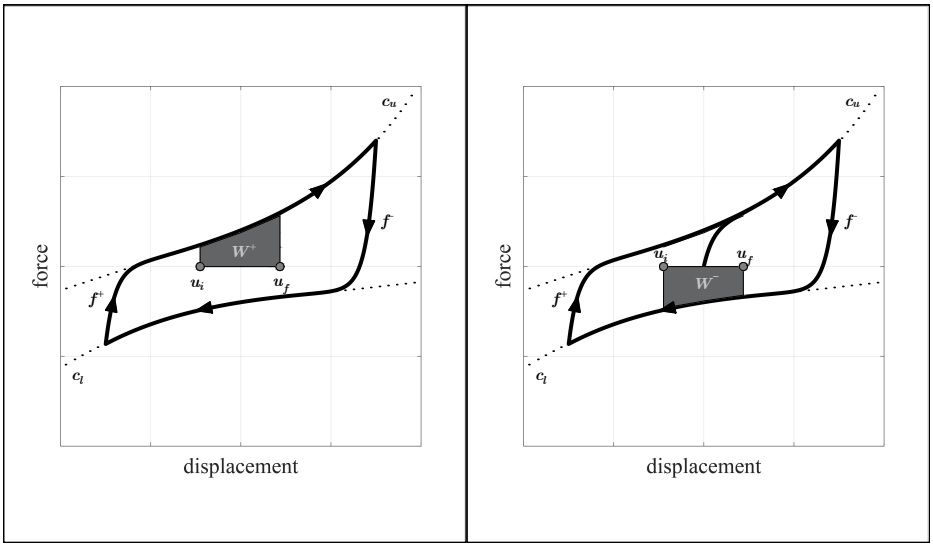
$$W_a^-(u_i, u_f) = \frac{\beta_1^-}{\beta_2^-}\left(e^{\beta_2^- u_f} - e^{\beta_2^- u_i}\right) - \beta_1^-(u_f - u_i), \tag{3.32a}$$

$$\begin{aligned} W_b^-(u_i, u_f) = 2\gamma_1^- \Bigg\{ &\frac{2\ln\left[e^{-\gamma_2^-(u_f-\gamma_3^-)} + 1\right]}{\gamma_2^-} \\ &- \frac{2\ln\left[e^{-\gamma_2^-(u_i-\gamma_3^-)} + 1\right]}{\gamma_2^-} + (u_f - u_i)\Bigg\}, \end{aligned} \tag{3.32b}$$

$$W_c^-(u_i, u_f) = \frac{k_b^-}{2}(u_f^2 - u_i^2) + f_0^+(u_f - u_i), \tag{3.32c}$$

Rather, the term W_d^- is computed as follows:

$$\begin{aligned} W_d^-(u_i, u_f, u_P, f_P) = + \frac{1}{\alpha^-} \Bigg[& \beta_1^- e^{\beta_2^- u_P} - \beta_1^- + \frac{4\gamma_1^-}{1 + e^{-\gamma_2^-(u_P - \gamma_3^-)}} \\ & -2\gamma_1^- + k_b^- u_P + f_0^- - f_P \\ & \times \left[e^{-\alpha^-(u_f - u_P)} - e^{-\alpha^-(u_i - u_P)} \right]. \end{aligned} \tag{3.33}$$



(a) (b)

Figure 3.4. Illustration of the generalized work function W corresponding to the loading (a) and unloading (b) phases of the hysteresis loop shown in Figure 3.2.

Figure 3.4a (b) shows an example of the work function W^+ (W^-), evaluated over the generic displacement interval $[u_i, u_f]$ ($[u_f, u_i]$) during the loading (unloading) phase of the generic hysteresis loop shown in Figure 3.2.

3.4 The Differential Reformulation of the Vaiana-Rosati Model (VRM+D)

The differential formulation of the Vaiana-Rosati Model [62] is based on two first-order linear ordinary differential equations. Their exact solutions are the closed-form expressions of the hysteresis force during the loading phase f^+ and hysteresis force during the unloading phase f^- contained in the analytical formulation of the Vaiana-Rosati Model (VRM+A), explained above. This version of the Model can easily compute the generalized force, tangent stiffness, and work, facilitating the use of it in computational frameworks and numerical simulations, enabling efficient analysis and design of mechanical systems subjected to complex loading conditions. Overall, the differential formulation represents a powerful tool for studying hysteretic behavior and holds significant potential for advancing the understanding and application of hysteretic models in engineering practice.

Generalized force

In order to determine the rate of the generalized force f^+, a new function is introduced:

$$g^+(u) = f_e^+(u) + k_b^+ u + f_0^+, \tag{3.34}$$

then, the equation 3.6 can be re-written as follow:

$$f^+(u, u_P, f_P) = g^+(u) - \left(g^+(u_P) - f_P\right) e^{-\alpha^+(u-u_P)}. \tag{3.35}$$

Proceeding to differentiate the previous equation with respect to displacement u, we have:

$$\frac{d}{du} f^+(u, u_P, f_P) = \frac{d}{du} g^+(u) + \alpha^+ \left(g^+(u_P) - f_P\right) e^{-\alpha^+(u-u_P)}, \tag{3.36}$$

and taking into account the Equation (3.35), it takes this form:

$$\frac{d}{du} f^+(u, u_P, f_P) = \frac{d}{du} g^+(u) - \alpha^+ \left(f^+(u, u_P, f_P) - g^+(u)\right) \tag{3.37}$$

which can also be described as:

$$\begin{aligned} \frac{d}{du} f^+(u, u_P, f_P) + \alpha^+ f^+(u, u_P, f_P) &= \frac{d}{du} g^+(u) + \alpha^+ g^+(u) \\ &= k_e^+(u) + k_b^+ + \alpha^+ g^+(u), \end{aligned} \tag{3.38}$$

Applying the chain rule to the force function f^+, it is possible to compute its rate:

$$\frac{d}{dt}f^+(u, u_P, f_P) = \frac{d}{du}f^+(u, u_P, f_P)\frac{du}{dt}, \tag{3.39}$$

and using (3.34) and (3.38), the equation 3.39 can be written as:

$$\begin{aligned}\dot{f}^+(u, u_P, f_P) = \big[k_e^+(u) + k_b^+ + \alpha^+ \left(f_e^+(u) + k_b^+ u\right. \\ \left. + f_0^+ - f^+(u, u_P, f_P)\dot{u},\end{aligned} \tag{3.40}$$

with $\dot{f}^+ = df^+/dt$ and $\dot{u} = du/dt$.

By writing the solution of the first-order linear ordinary differential equation $\dot{f}^+$, it can prove that its exact solution is precisely the expression of f^+ function in Equation 3.6. Thus:

$$f^+(u, u_P, f_P) = f_c^+(u, u_P, f_P) + f_p^+(u), \tag{3.41}$$

where f_c^+ is the complementary solution associated with the homogeneous ordinary differential equation and f_p^+ is the particular one, and they take these expressions:

$$f_c^+(u, u_P, f_P) = C^+(u_P, f_P)\, e^{-\alpha^+ u}, \tag{3.42}$$

and

$$f_p^+(u) = e^{-\alpha^+ u} \int \left(k_e^+(u) + k_b^+ + \alpha^+ g^+(u)\right) e^{+\alpha^+ u} du. \tag{3.43}$$

To begin with, we have:

$$\int k_e^+(u), e^{+\alpha^+ u} du = f_e^+(u), e^{+\alpha^+ u} - \alpha^+ \int f_e^+(u), e^{+\alpha^+ u} du, \tag{3.44}$$

based on Equation (3.18). Next, we can write:

$$\int k_b^+, e^{+\alpha^+ u} du = k_b^+ u, e^{+\alpha^+ u} - \alpha^+ \int k_b^+ u, e^{+\alpha^+ u} du, \tag{3.45}$$

and also:

$$\int \alpha^+ g^+(u), e^{+\alpha^+ u} du = \alpha^+ \int \left(f_e^+(u) + k_b^+ u + f_0^+\right), e^{+\alpha^+ u} du, \tag{3.46}$$

as deduced from Equation (3.34).

By combining the three equations above, we can express Equation (3.43) as:

$$f^+ p(u) = e^{-\alpha^+ u} \left(f e^+(u), e^{+\alpha^+ u} + k_b^+ u, e^{+\alpha^+ u} + \alpha^+ f_0^+ \int e^{+\alpha^+ u} du \right), \tag{3.47}$$

or, equivalently, after performing the indefinite integral:

$$f^{+}p(u) = fe^{+}(u) + k_b^{+}u + f_0^{+}. \tag{3.48}$$

Therefore, the solution to Equation (3.38) is:

$$f^{+}(u, u_P, f_P) = C^{+}(u_P, f_P), e^{-\alpha^{+}u} + f_e^{+}(u) + k_b^{+}u + f_0^{+}. \tag{3.49}$$

The integration constant C^{+} is determined by choosing the solution that satisfies $f^{+}(u_P, u_P, f_P) = f_P$, passing through the point $P(u_P, f_P)$:

$$C^{+}(u_P, f_P), e^{-\alpha^{+}u_P} + f_e^{+}(u_P) + k_b^{+}u_P + f_0^{+} = f_P, \tag{3.50}$$

thus yielding:

$$C^{+}(u_P, f_P) = \left(f_P - f_e^{+}(u_P) - k_b^{+}u_P - f_0^{+}\right) e^{+\alpha^{+}u_P}. \tag{3.51}$$

Finally, substituting this expression of C^{+} back into (3.49), we obtain Equation (3.6).

Considerations made for the loading function f^{+} can be equivalently made for the unloading function f^{-}. In fact, to determine the rate equation for the generalized force f^{-}, we introduce the following function:

$$g^{-}(u) = f_e^{-}(u) + k_b^{-}u - f_0^{-}, \tag{3.52}$$

allowing Equation (3.12) to be equivalently rewritten as:

$$f^{-}(u, u_P, f_P) = g^{-}(u) - \left(g^{-}(u_P) - f_P\right) e^{+\alpha^{-}(u-u_P)}. \tag{3.53}$$

Differentiating the above relation with respect to u gives:

$$\frac{d}{du} f^{-}(u, u_P, f_P) = \frac{d}{du} g^{-}(u) - \alpha^{-} \left(g^{-}(u_P) - f_P\right) e^{+\alpha^{-}(u-u_P)}, \tag{3.54}$$

which, based on Equation (3.53), simplifies to:

$$\frac{d}{du} f^{-}(u, u_P, f_P) = \frac{d}{du} g^{-}(u) + \alpha^{-} \left(f^{-}(u, u_P, f_P) - g^{-}(u)\right). \tag{3.55}$$

Considering Equations (3.22) and (3.52), the above expression can be also rewrit-

ten as:

$$\begin{aligned}\frac{d}{du}f^-(u,u_P,f_P)-\alpha^-f^-(u,u_P,f_P)&=\frac{d}{du}g^-(u)-\alpha^-g^-(u)\\&=k_e^-(u)+k_b^--\alpha^-g^-(u).\end{aligned}\tag{3.56}$$

To derive the rate equation for f^-, we first apply the chain rule to f^-:

$$\frac{d}{dt}f^-(u,u_P,f_P)=\frac{d}{du}f^-(u,u_P,f_P)\frac{du}{dt},\tag{3.57}$$

and then use Equations (3.52) and (3.56) to express Equation (3.57) as:

$$\begin{aligned}\dot{f}^-(u,u_P,f_P)=\big[k_e^-(u)+k_b^--\alpha^-\left(f_e^-(u)+k_b^-u\right.\\-f_0^--f^-(u,u_P,f_P)\dot{u},\end{aligned}\tag{3.58}$$

where $\dot{f}^-=df^-/dt$ and $\dot{u}=du/dt$.

To show that the function f^- given by Equation (3.12) is the solution of the first-order linear ordinary differential equation (3.56), we begin by expressing the solution as:

$$f^-(u,u_P,f_P)=f_c^-(u,u_P,f_P)+f_p^-(u),\tag{3.59}$$

where f_c^- is the complementary solution, and f_p^- is the particular one. It follows that:

$$f_c^-(u,u_P,f_P)=C^-(u_P,f_P)\,e^{+\alpha^-u},\tag{3.60}$$

and:

$$f_p^-(u)=e^{+\alpha^-u}\int\left(k_e^-(u)+k_b^--\alpha^-g^-(u)\right)e^{-\alpha^-u}du.\tag{3.61}$$

Additionally, we can write:

$$\int k_e^-(u)\,e^{-\alpha^-u}du=f_e^-(u)\,e^{-\alpha^-u}+\alpha^-\int f_e^-(u)\,e^{-\alpha^-u}du,\tag{3.62}$$

according to Equation (3.22),

$$\int k_b^-\,e^{-\alpha^-u}du=k_b^-u\,e^{-\alpha^-u}+\alpha^-\int k_b^-u\,e^{-\alpha^-u}du,\tag{3.63}$$

and:

$$\int\alpha^-g^-(u)\,e^{-\alpha^-u}du=\alpha^-\int\left(f_e^-(u)+k_b^-u-f_0^-\right)\,e^{-\alpha^-u}du,\tag{3.64}$$

using Equation (3.52).

Summing these three equations, we obtain:

$$f_p^-(u) = e^{+\alpha^- u}\left(f_e^-(u)\, e^{-\alpha^- u} + k_b^- u\, e^{-\alpha^- u} + \alpha^- f_0^- \int e^{-\alpha^- u} du\right), \tag{3.65}$$

which simplifies to:

$$f_p^-(u) = f_e^-(u) + k_b^- u - f_0^-, \tag{3.66}$$

after evaluating the indefinite integral.

Therefore, the solution to Equation (3.56) is:

$$f^-(u, u_P, f_P) = C^-(u_P, f_P)\, e^{+\alpha^- u} + f_e^-(u) + k_b^- u - f_0^-. \tag{3.67}$$

To find the integration constant C^-, we apply the condition

$$f^-(u_P, u_P, f_P) = f_P. \tag{3.68}$$

Thus:

$$C^-(u_P, f_P)\, e^{+\alpha^- u_P} + f_e^-(u_P) + k_b^- u_P - f_0^- = f_P, \tag{3.69}$$

yielding:

$$C^-(u_P, f_P) = \left(f_P - f_e^-(u_P) - k_b^- u_P + f_0^-\right) e^{-\alpha^- u_P}. \tag{3.70}$$

Finally, substituting this expression back into (3.67), we recover Equation (3.12).

Generalized tangent stiffness

During the loading phase of the hysteresis loop, when $\dot{u} > 0$, the generalized tangent stiffness k_t^+ is defined as:

$$k_t^+(u, u_P, f_P) = \frac{d}{du} f^+(u, u_P, f_P), \tag{3.71}$$

which, by using Equations (3.34) and (3.38), simplifies to:

$$k_t^+(u, u_P, f_P) = k_e^+(u) + k_b^+ + \alpha^+\left(f_e^+(u) + k_b^+ u + f_0^+ - f^+(u, u_P, f_P)\right), \tag{3.72}$$

where $f_e^+(u)$ and $k_e^+(u)$ derive from Equations (3.5) and (3.18), respectively.

On the other hand, during the unloading phase of the hysteresis loop, for $\dot{u} < 0$, the generalized tangent stiffness k_t^- is given by:

$$k_t^-(u, u_P, f_P) = \frac{d}{du} f^-(u, u_P, f_P), \tag{3.73}$$

and using Equations (3.52) and (3.56), we obtain:

$$k_t^-(u, u_P, f_P) = k_e^-(u) + k_b^- - \alpha^- \left(f_e^-(u) + k_b^- u - f_0^- - f^-(u, u_P, f_P) \right), \quad (3.74)$$

where $f_e^-(u)$ and $k_e^-(u)$ are computed from Equations (3.11) and (3.22), respectively.

It is important to note that providing the rate equation for k_t^+ (k_t^-) is unnecessary, as the generalized tangent stiffness can be directly computed using Equation (3.72) (Equation (3.74)) once f^+ (f^-) after solving the Equation (3.40) (Equation (3.58)).

Generalized work

To determine the rate equation for the generalized work W^+ related to the loading phase, we start by applying the chain rule to the function W^+. This yields:

$$\begin{aligned} \dot{W}^+(u, u_P, f_P) &= \frac{d}{dt} W^+(u, u_P, f_P) = \frac{d}{du} W^+(u, u_P, f_P) \frac{du}{dt} \\ &= f^+(u, u_P, f_P)\, \dot{u}. \end{aligned} \quad (3.75)$$

Similarly, to find the rate equation for the generalized work W^- related to the unloading phase, we again apply the chain rule, resulting in:

$$\begin{aligned} \dot{W}^-(u, u_P, f_P) &= \frac{d}{dt} W^-(u, u_P, f_P) = \frac{d}{du} W^-(u, u_P, f_P) \frac{du}{dt} \\ &= f^-(u, u_P, f_P)\, \dot{u}. \end{aligned} \quad (3.76)$$

It is notably that W^+ (W^-) can be computed using Equation (3.75) (Equation (3.76)) once f^+ (f^-) after solving Equation (3.40) (Equation (3.58)).

3.5 Calibration Methods and Parameter Identifications

Accurate representation of hysteresis in structural materials is essential for predicting their behavior under cyclic loading. Calibration of hysteresis models involves identifying parameters that best fit experimental data, a step that is crucial for creating predictive and reliable models. To understand calibration's role within the broader framework of model development, it is essential to consider two other processes that precede and follow calibration: verification and validation [59, 42]. These phases are defined by the American Society of Mechanical

Engineers (ASME) [57]. The first phase, verification, is defined as *"the process of determining that a computational model accurately represents the underlying mathematical model and its solution"*. Verification confirms that the computational model correctly implements its theoretical algorithms, ensuring consistency between the code and mathematical formulations and confirming the model designer's intentions. This step is focused on internal accuracy, not yet comparing the model to real-world data. Following calibration, validation is performed. According to ASME, validation is *"the process of determining the degree to which a model is an accurate representation of the real world from the perspective of the intended uses of the model"*. This step tests whether the model can reliably predict behaviors beyond the calibration dataset, solidifying its applicability to real-world scenarios. Calibration itself serves as an intermediate phase, bridging verification and validation. Calibration adjusts model parameters to align the model more closely with specific experimental or observed data, improving accuracy within a controlled dataset. However, it does not necessarily ensure predictive accuracy in untested conditions, which is assessed during validation.

Calibration can be divided into two main processes: manual calibration and optimization-based calibration. Initially, a sensitivity analysis is conducted to determine each parameter's influence on the model's output, identifying the most impactful parameters for focused calibration. Manual calibration follows, where parameters are iteratively adjusted based on expert judgment and visual comparison between the model's predictions and experimental results. While time-consuming, manual calibration leverages model knowledge to achieve a satisfactory fit. To enhance precision and objectivity, optimization procedures are then employed. These procedures use algorithms, such as genetic algorithms or gradient-based methods, to systematically explore the parameter space, efficiently converging to optimal parameter sets by minimizing an objective function [43, 42]. Combining manual calibration with optimization techniques ensures robust and reliable parameter identification, ultimately resulting in accurate and predictive hysteresis models for timber connections. By following this structured approach of verification, calibration, and validation, the model can be refined to provide accurate and meaningful predictions in practical applications.

3.5.1 Sensitivity Analysis

The Vaiana-Rosati Model, previously illustrated in the two versions, is characterized by two sets of eight parameters that influence the behavior of the hysteretic loop in various ways. To consciously manipulate the model and carefully describe the materials' behavior, each parameter's influence was analyzed by imposing a sinusoidal generalized displacement with a unit amplitude and frequency. This process provides valuable insights for optimizing the model's performance

and understanding its behavior in different scenarios, particularly useful when the model replicates the experimental hysteresis loops. It is possible to subdivide the parameters' effect into three groups: the former group with base parameters including k_b, α, and f_0; the second with β_1 and β_2 and the last with γ_1, γ_2, and γ_3.

The hysteresis loop taken into account is obtained for the following parameter values: $k_b^+ = 0.5$, $f_0^+ = 2.5$, $\alpha^+ = 10$, $\beta_1^+ = 0$, $\beta_2^+ = 0$, $\gamma_1^+ = 0.5$, $\gamma_2^+ = 4$ and $\gamma_3^+ = 1.5$; $k_b^- = 0.5$, $f_0^- = 2$, $\alpha^- = 10$, $\beta_1^- = 0$, $\beta_2^- = 0$, $\gamma_1^- = 0.5$, $\gamma_2^- = 8$ and $\gamma_3^- = -1$. It is asymmetric and limited by two $S2$-shaped limiting curves with one inflection point, where the upper curve is an increasing curve, whereas the lower one is a decreasing curve.

Only the positive or negative parameters in each case were changed to analyze the sensitivity of each parameter on the hysteresis loop. This method allowed for a clear understanding of how individual parameters influence the loop shape and behavior without the confounding effects of simultaneously altering multiple parameters. Starting from the initial loop shape, changing the values of k_b^+ (k_b^-), f_0^- (f_0^+), and α^+ (α^-), we can observe, in Figure 3.5a-c, respectively, an increase in the slope of the upper (lower) limiting curve, a shift of the lower (upper) limiting curve downward (upward), and an increase of the curvature of the generic loading (unloading) curve. To explore the influence of parameters β_1 and β_2, the initial values of model parameters were set differently from zero and, in particular, $\beta_2 = 0.5$. Looking at Figure 3.5d-e, if the values of β_1 and β_2 change, there is a variation in the slope of the generic loading (unloading) curve. Otherwise, increasing β_1 and simultaneously decreasing β_2 makes it possible to decrease the curvature of the limiting curves. On the contrary, by reducing β_1 and at the same time increasing β_2, it is possible to increase the curvature of the limiting curves. Finally, observing Figure 3.5f-h by changing the value of γ_1, γ_2, and γ_3 parameters, it is possible to manage the inflection effect of the limiting curves. In particular, the parameter γ_1 affects the vertical distance between asymptotes of the limit curves; γ_2 influences the slope of the tangent to the limit curve at the inflection point, and lastly, γ_3 moves the inflection point horizontally, to the right for the loading curve and the left for the unloading one [63].

The principal roles of the model parameters are finally summarized in Table 3.1. In particular, parameters are grouped into (i) *basic loop shape*, (ii) *curvature*, and (iii) *pinching* related to the effects that produce their modification, and for each parameter, its role in the hysteresis loop shape is explained.

3.5.2 Parameter Identification

Parameter identification, also known as parameter estimation, is a fundamental step in simulating mechanical phenomena. The procedure involves determin-

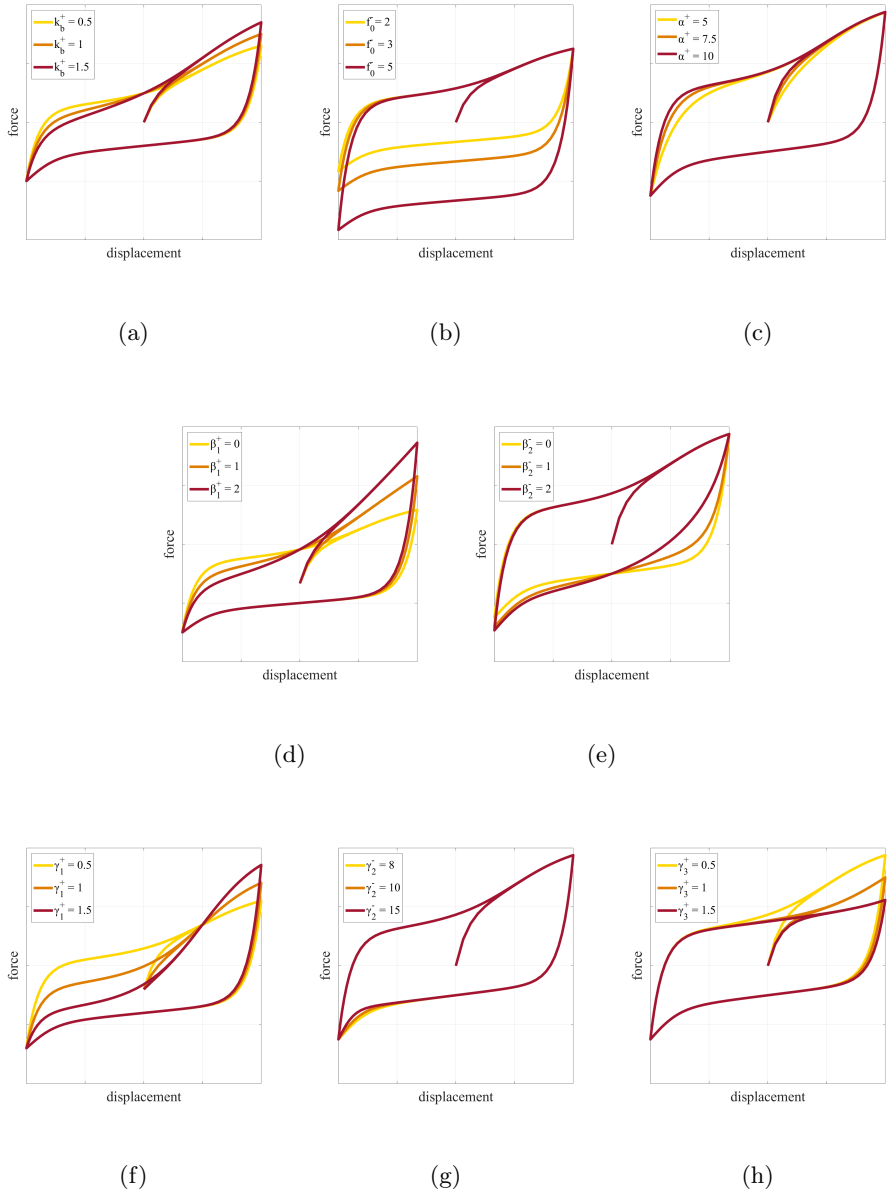


Figure 3.5. Influence of Vaiana-Rosati Model parameters on the shape of the hysteresis loop

Parameter	Role	Group
k_b	variation in the slope of the limiting curve	basic loop shape
f_0	intercept of the limiting curve with the y-axis	
α	variation in the curvature of the generic (un)loading curve	
β_1	variation in the curvature of the limiting curve	curvature
β_2	variation in the curvature of the limiting curve	
γ_1	variation in vertical distance between asymptotes of the limit curve	pinching
γ_2	variation in the slope of the tangent to the limit curve at the inflection point	
γ_3	moves the inflection point horizontally	

Table 3.1. Summary of Vaiana-Rosati Model parameters and their roles for hysteresis loop shape.

ing the values of parameters in mathematical models that describe a system's behavior. It can be evaluated using different strategies and techniques. Related to the problem's complexity, it is possible to identify parameters manually or using one of the many automated algorithms, with their advantages and disadvantages. In particular, manual identification follows the sensitivity analysis and it is often preferred when researchers have a deep understanding of the system, data is limited, or when there are strong prior beliefs about the parameter values [42]. On the other hand, automated identification is valuable when dealing with complex models and large data sets or when an objective, data-driven approach is necessary. It is also useful when exploration of a wide parameter space is required. In some cases, a hybrid approach can be used, combining the expertise of manual identification with the efficiency and objectivity of automated methods to strike a balance between control and accuracy.

The identification process is often called an optimization problem because it involves finding the best set of parameters for a mathematical model that

minimizes the difference between the model's predictions and the observed experimental data. In other words, it's about optimizing the parameters to make the model fit the data as closely as possible.

3.5.3 Optimization Methods for Parameter Identification

Optimization methods are a crucial tool in the field of parameter identification, allowing researchers to determine the most suitable set of parameters for a mathematical model [43, 32]. The process of optimization involves the careful selection of the best option from a multitude of available choices, with these choices evaluated against specific criteria. The ultimate goal in optimization is often to either minimize or maximize a particular objective function, which encapsulates the essence of the problem being addressed. Two fundamental components must be established to formally define an optimization problem. The first is a set of feasible solutions, denoted as $\boldsymbol{X}$, representing the range of possible values for the parameters under consideration. The second is the objective function, typically denoted as $y = OF(x)$, where x is an element of $\boldsymbol{X}$, and $OF(x)$ represents the measure to be minimized or maximized for achieving the desired outcome. Formally, the problem is expressed in two distinct forms:

$$\min_{x \in X} OF(x) \quad \text{or} \quad \max_{x \in X} OF(x). \tag{3.77}$$

These formulations establish the core structure of optimization problems and serve as the foundation for various optimization techniques.

In the context of parameter identification, the vector $\boldsymbol{X}$, which represents the parameters, is not free to take arbitrary values. Instead, it is subject to a set of mathematical constraints. These constraints ensure that the identified parameters adhere to the properties and physical limits of the underlying system, and they are expressed as a combination of equations and inequalities, which take on the following general forms:

$$\begin{aligned} g_i(x) &= b_i \text{ for } i = 1, ..., n \\ h_j(x) &\leq d_j \text{ for } j = 1, ..., m, \end{aligned} \tag{3.78}$$

In these expressions, g_i and h_j represent equations and inequalities, respectively, pivotal in constraining the problem. They encapsulate the relationships and dependencies within the system, and they must be satisfied by the identified parameter values. The terms b_i and d_j are constants and represent the specific conditions or requirements associated with each constraint. The ultimate solution to the parameter identification problem is acceptable only if it respects and satisfies all these constraints. Balancing the optimization objective with these

constraints is a fundamental aspect of parameter identification, ensuring that the identified parameters are not only optimal in terms of the objective function but also consistent with the system's underlying physical and mathematical relationships.

The resolution method for solving optimization problems is a fundamental approach that enables us to determine the solutions for vector $\boldsymbol{X}$. These solutions can be classified into two primary categories: exact and heuristic, each with distinct characteristics and applications. An exact solution, as the name implies, represents the best possible outcome in the context of the optimization problem. It is a solution that rigorously adheres to the problem's constraints and optimizes the objective function. Exact solutions are often obtained through precise and often computationally intensive methods, such as mathematical programming, exact algorithms, or rigorous optimization techniques. These methods guarantee that the solution found is the absolute best among all feasible alternatives within the defined problem space. On the other hand, a heuristic solution, while not necessarily the absolute best, is a valid approach in scenarios where finding the exact solution is impractical or computationally cost-prohibitive. Heuristic methods focus on finding *good enough* solutions in a more efficient and expedited manner. While these solutions may not be optimal, they often balance quality and computational resources. Heuristic techniques include genetic algorithms, simulated annealing, and particle swarm optimization. In practice, the choice between exact and heuristic resolution methods depends on the problem's nature, complexity, and the trade-off between solution quality and computational resources. Researchers often use heuristic methods when exact solutions are impractical, as they can provide valuable insights and near-optimal results. Determining which method to employ is a critical decision in optimization, as it directly impacts the quality and efficiency of the solutions obtained for the vector $\boldsymbol{X}$ [36, 49, 34].

Once the problem structure is defined, optimization methods can be classified into two primary categories based on their approach to finding solutions: local optimizers and global optimizers.

Local search Optimizers: *fminsearch* Algorithm

Local search optimizers are heuristic methods that focus on refining solutions within a limited region of the parameter space [55, 43]. These methods iteratively adjust parameters to minimize or maximize the objective function, typically starting from an initial guess. While effective in converging towards a local minimum or maximum, local optimizers do not guarantee that the global optimum will be found, especially when there are multiple local minimums or maximums. Moreover, the end of the process does not ensure an optimal solution, and it can stop after a given time limit.

The *fminsearch* algorithm is a widespread example of a local search optimizer. It utilizes the Nelder-Mead simplex method [44], a derivative-free optimization technique suitable for unconstrained problems. A simplex is a geometric figure consisting of $n+1$ vertices in a n-dimensional space. For example, the simplex is a triangle in two dimensions (Figure 3.6) and a tetrahedron in three dimensions. The simplex adapts its shape and size as it explores the parameter space to find an optimum. The *fminsearch* algorithm iteratively updates the simplex using four key operations:

1. reflection: the algorithm reflects the worst vertex (the point with the highest function value) through the centroid of the remaining n vertices. This creates a new candidate point. Reflection aims to explore regions of the search space likely to yield better objective function values by moving away from poor-performing areas;

2. expansion: if the reflected point shows significant improvement, the algorithm tries to expand further in the same direction by moving even further away from the centroid. This is done by calculating a new point beyond the reflected point. Expansion helps in taking larger steps when the search direction appears promising;

3. contraction: if the reflected point does not yield improvement, the algorithm contracts the simplex towards the better-performing points. This is done by moving the worst point closer to the centroid towards the inside (inside contraction) or outside (outside contraction). Contraction helps fine-tune the search around a promising region when large steps are not beneficial;

4. shrinkage: if neither reflection nor contraction improves the solution, the algorithm shrinks the entire simplex towards the best vertex. All points are moved closer to the best point found so far. Shrinkage reduces the search space, allowing the algorithm to focus on a smaller region when progress stalls.

Global Optimizers: Genetic Algorithm

In contrast, global optimizers are designed to explore a broader parameter space range to identify the objective function's global minimum or maximum. These methods, like Genetic Algorithms, Particle Swarm Optimization (PSO), and Simulated Annealing, employ heuristic strategies to systematically search for solutions across different regions. Genetic Algorithms are popular in the optimization field of hysteretic models [32]. They are based on Darwin's evolutionary

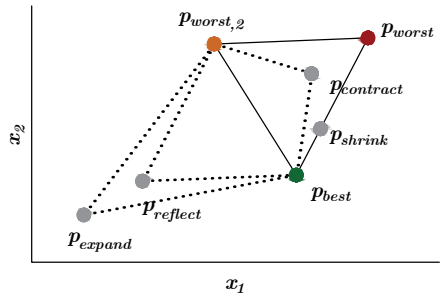


Figure 3.6. Example of the iteration process of the Nelder-Mead simplex method on a two-dimensional simplex.

theory and simulate the population selection. Generally, they are used to generate more stable and high-quality optimized solutions. As Figure 3.7 shows, the process is based on specific mechanisms that reflect genetic evolution, and in particular, they are:

1. the initialization of the process starts by creating an initial population of individuals. Each individual is usually represented by a string called a chromosome. The number of individuals defines the population size;

2. follows the evaluation of each individual in the population using a Fitness Function. This function measures how well an individual solves the problem at hand;

3. the selection of Parents from the current population is made using different methods, such as roulette wheel selection, tournament selection, and rank-based selection;

4. crossover implies the combination of Parents to create new individuals. It is possible to choose one or more points where the parents' chromosomes will be split and recombined, as well as the Crossover Rate, which determines the proportion of the population to undergo crossover;

5. mutation is made to introduce random Variation of the genetic material to maintain genetic diversity. In this case, the Mutation Rate decides the probability of a mutation occurring in an individual;

6. the process terminates for different reasons: when the algorithm reaches a maximum number of generations, a satisfactory fitness level or a stagnation in fitness improvement occurs;

7. finally, the individual with the highest fitness score in the final population is considered the best solution to the problem.

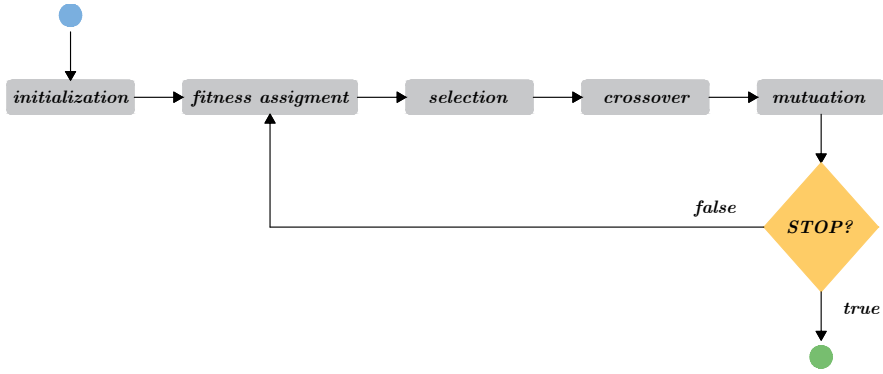


Figure 3.7. Example of the operation process of the genetic algorithm.

3.5.4 Application of Optimization Methods

The choice between local and global optimizers depends on the optimization problem's nature, complexity, dimensionality, and the desired balance between solution quality and computational resources. Local optimizers, like *fminsearch*, are suitable for problems where finding a precise solution around a given starting point is critical [73, 29]. In contrast, global optimizers, such as Genetic Algorithms, succeed in scenarios requiring the exploration of diverse solutions across a larger parameter space [49, 48, 69]. Researchers often integrate both optimizers in a hybrid approach to leverage their respective strengths and improve the efficiency and reliability of parameter identification tasks [39, 33, 24].

To evaluate the potential and distinct features of global and local optimization techniques, we used both *fminsearch* and the Genetic Algorithm to simulate specific experimental hysteresis loops. Starting from experimental data, the objective function was designed to minimize the difference between the input data and the simulated response, ensuring an accurate representation of the hysteresis behavior.

These sections present the MATLAB code implementation of the *fminsearch* method and genetic algorithm and detail the key components of the optimization process.

MATLAB Code Using *fminsearch* for Parameter Optimization

The optimization process begins with loading the experimental displacement and force data of a typical hysteresis loop:

```
%% Experimental data
exp_x = d; % displacement data
exp_F = f; % force data
```

We define the initial set of model parameters (x_0) to establish a starting point for the optimization. These parameters can be chosen arbitrarily or based on prior manual calibration of the VRM:

```
%% Initial set of model parameters
x0 = [0.70,2.00,4.10, 0.10, 0.80,0.0,-1.0,-1.0,
      0.70,2.00,4.10,-0.02,-1.35,0.0, 0.0, 0.0];
```

The objective function calculates the error between the experimental and simulated forces, which *fminsearch* aims to minimize. The error metric is computed using the root mean square (RMS) error, which provides a measure of the average magnitude of the differences:

$$\text{error} = \sqrt{\frac{1}{n}\sum_{i=1}^{n}(f_{exp} - F_{model})^2} \tag{3.79}$$

where n represents the total number of data points in the cycle. The MATLAB implementation of this objective function is as follows:

```
%% Optimization
objectiveFcn = @(params) hysteresisObjective(params, exp_x,
    exp_F); % objective function

function error = hysteresisObjective(params, exp_x, exp_F)

    % Extract parameters
    kbp     = params(1);  kbm     = params(9);
    f0p     = params(2);  f0m     = params(10);
    alfap   = params(3);  alfam   = params(11);
    beta1p  = params(4);  beta1m  = params(12);
    beta2p  = params(5);  beta2m  = params(13);
    gamma1p = params(6);  gamma1m = params(14);
    gamma2p = params(7);  gamma2m = params(15);
    gamma3p = params(8);  gamma3m = params(16);

    % Initialize variables
```

```
    F_model = zeros(size(exp_x));
    for i = 2:length(exp_x)
        dx = exp_x(i) - exp_x(i-1);
        params = VRM_AF_par(sign(dx), kbp, kbm, f0p, f0m,
            alfap, alfam, beta1p, beta1m, beta2p, beta2m,
            gamma1p, gamma1m, gamma2p, gamma2m, gamma3p,
            gamma3m);
        F_model(i) = VRM_AF_f(exp_x(i), sign(dx), exp_x(i-1),
             F_model(i-1), params);
    end

    % Calculate error
    error = sqrt(mean((exp_F - F_model).^2)); % root mean
        square error
end
```

The functions *VRM_AF_par* and *VRM_AF_f* compute the VRM parameters and the generalized force analytically. The latter function includes the mathematical formulations detailed in Section 3.3 (3.5-3.7 and 3.11-3.13).

The optimization is executed using the *fminsearch* function, which returns the optimal parameter set (*paramOpt*), the minimized error value ($fval$), and additional diagnostic information about the optimization process:

```
% Run the fminsearch optimization
[paramOpt, fval, exitflag, output] = fminsearch(objectiveFcn,
    x0);
```

This approach allows for a systematic exploration of the parameter space, leveraging the strengths of *fminsearch* as a local optimizer. The performance of this method is compared to the Genetic Algorithm in subsequent sections to highlight the differences in efficiency and accuracy.

MATLAB Code Using the Genetic Algorithm for Parameter Optimization

Compared to the *fminsearch* method, the Genetic Algorithm requires additional configuration to handle the complexity and non-linearity of the parameter optimization problem. The GA is a global optimization technique that mimics the process of natural selection to search for the optimal set of parameters efficiently. First, the input arguments are set, including the number of variables n, the initial set of model parameters x_0, the linear equality and inequality constraints (A_eq, b_eq, A, b), and lower and upper bounds (l_b, u_b).

```
%% Input arguments
```

```
n = 16;
x0 = [0.70,2.00,4.10, 0.10, 0.80,0.0,-1.0,-1.0,
      0.70,2.00,4.10,-0.02,-1.35,0.0, 0.0, 0.0];
lb = [0,0,-10,-10,-10,-10,-10,-10,
      0,0,-10,-10,-10,-10,-10,-10];
ub = [10,10,10,10,10,10,10,10,
      10,10,10,10,10,10,10,10];
```

In this example, only the lower and upper bounds are specified to constrain the search space, ensuring that the model parameters remain within physically meaningful ranges.

The objective function remains the same as in the *fminsearch* case, where it calculates the error between the experimental and simulated forces. The Genetic Algorithm is then called with specific options set for optimization:

```
%% OPTIMIZATION
% Define the anonymous function handle for the combined
    objective function
objectiveFcn = @(params) hysteresisObjective(params, exp_x,
    exp_F);

% Run the genetic algorithm optimization (global optimizer)
options = optimoptions('ga', 'Display', 'iter', '
    MaxGenerations', 2500, 'OutputFcn', @gaOutputFcn, '
    InitialPopulationMatrix', x0);
[paramOpt_ga, fval_ga, exitflag, output_ga] = ga(objectiveFcn
    , n, [], [], [], [], lb, ub, [], options);
```

The solver options include:

- Display: controls how the progress of the optimization is displayed; here, it is set to 'iter' to show the details of each iteration;
- MaxGenerations: specifies the maximum number of generations for the GA, which influences how thoroughly the parameter space is explored;
- OutputFcn: allows customization of the output information and can be modified to tailor the optimization process further;
- InitialPopulationMatrix: the vector x_0 will be part of the initial population, and the GA will use it as one of the starting points while generating the rest of the population randomly within the defined bounds (l_b and u_b). This might help the GA to converge faster in some cases, especially if x_0 is close to the optimal solution. However, this option is not required when using the Genetic Algorithm, because the lower and upper bounds are sufficient to operate effectively.

By employing the Genetic Algorithm, the model gains the ability to explore a broader parameter space more effectively, which is particularly useful for complex and highly non-linear problems where local optimizers like *fminsearch* may struggle. The results from both optimization methods are compared later to illustrate the strengths and limitations of global versus local optimization techniques.

Figure 3.8 presents the optimization process in a flowchart diagram. This schematic representation outlines the steps involved in setting up and running the optimization for parameter identification. The process is flexible and can be adapted to various study cases by varying the input data, using alternative hysteresis models to better capture the specific behavior of the structural system, or selecting a different optimization algorithm. This adaptability ensures that the framework can be applied to a wide range of hysteresis modeling scenarios, making it a robust tool for simulating and understanding complex dynamic behaviors in structural systems.

Comparison between Optimization Methods

To compare the potentialities of the automated calibration of the VRM by using the $fminsearch$ method and the Genetic Algorithm, four examples of optimized hysteresis loops are shown in Figure 3.9. The corresponding Tables 3.2, 3.4, 3.6, 3.8, display the initial parameter values (x_0), lower (l_b) and upper (u_b) bounds, and the optimized parameters for each case. Furthermore, Tables 3.3, 3.5, 3.7, 3.9 provide a detailed comparison of computation time, the number of iterations, and convergence quality, illustrating the trade-offs between precision and computational effort. The hysteresis loops shown in Figures 3.9a-c demonstrate that both optimization algorithms are capable of effectively minimizing the objective function, with error discrepancies not exceeding 3.52% when compared to experimental data. However, the limitations of *fminsearch* become apparent in the last case depicted in Figure 3.9d, where the error rises to 17.32%. This significant discrepancy can be attributed to the increased complexity of the loop shape. Unlike the other examples, this particular hysteresis loop is more intricate and is characterized by being confined to a single quadrant, making it more challenging for *fminsearch* to converge accurately. The algorithm's tendency to get trapped in local minima becomes more pronounced in such cases, where the loop shape's non-linearity and asymmetric behavior pose additional challenges.

In general, it is possible to conclude that, despite the differences in their underlying mechanisms, both methods can effectively minimize the objective function to an acceptable degree of accuracy. While *fminsearch* converges faster and requires fewer iterations due to its local optimization nature, it may get trapped in local minima, especially in complex, multimodal landscapes. In contrast, though computationally more intensive and slower to converge, the Genetic Algorithm

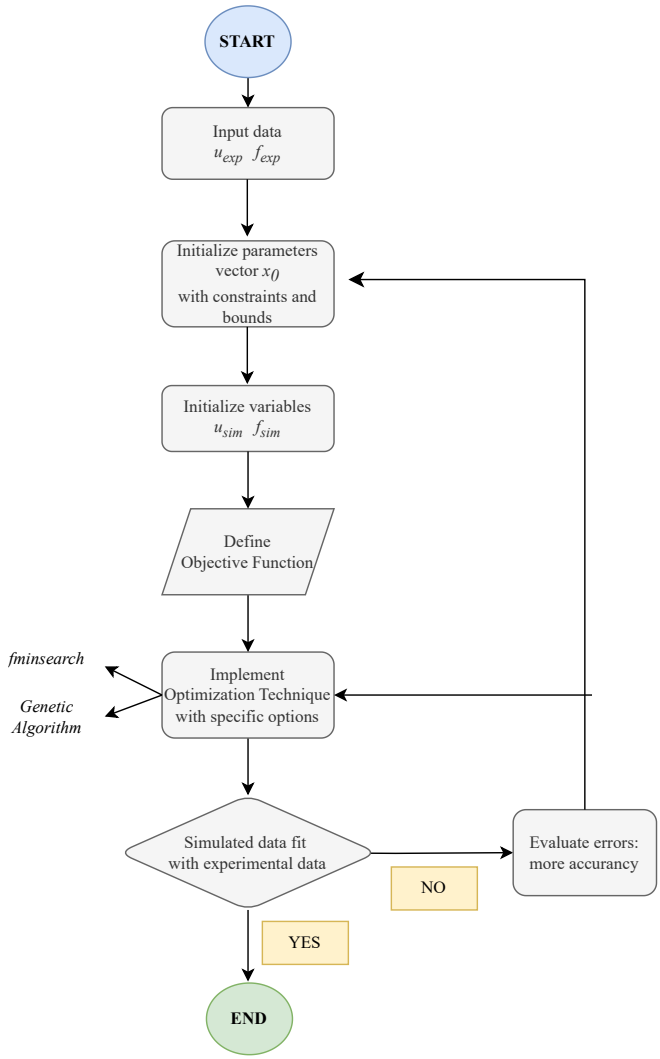


Figure 3.8. Flowchart of the optimization process of hysteresis model parameters.

explores a broader range of potential solutions, thereby increasing the likelihood of escaping local minima and achieving a more globally optimal solution. This highlights the trade-off between exploration (GA) and exploitation (*fminsearch*)

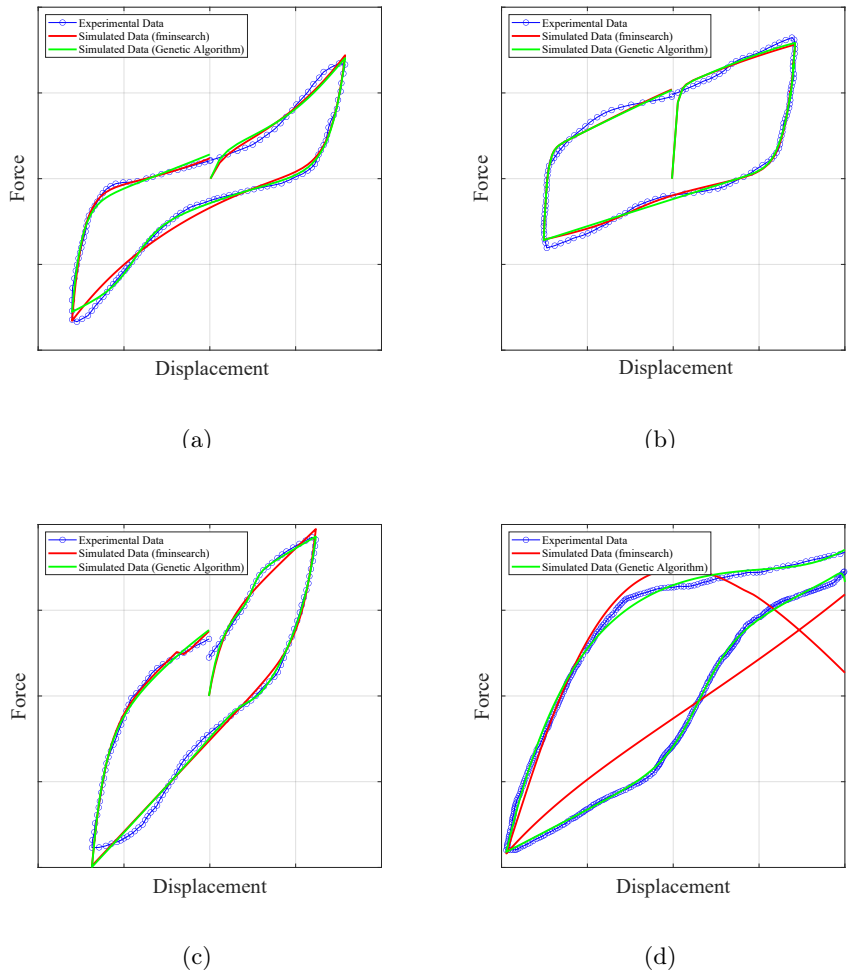


Figure 3.9. Examples of the optimized hysteresis loops, comparing the experimental loops with the simulated one using the *fminsearch* and Genetic Algorithms.

in optimization tasks. For complex, non-linear problems or cases with unique hysteresis shapes, combining both methods may even be considered to leverage their complementary strengths.

3.6 Conclusion of Chapter 3

This Chapter introduced the Vaiana-Rosati Model (VRM) as a more effective alternative to traditional hysteresis models for simulating the complex behavior of timber connections by comparing it with the Bouc-Wen and Dolan Model. The VRM's flexibility in capturing asymmetric loop shapes, stiffness degradation, and pinching effects was emphasized.

A sensitivity analysis provided a foundation for manual parameter calibration, highlighting the influence of key parameters. However, automated optimization methods were applied to enhance accuracy and efficiency. The *fminsearch* method proved efficient for simpler cases but struggled with complex loop shapes, often getting trapped in local minima. In contrast, the Genetic Algorithm offered a more robust, global search, yielding better accuracy for challenging hysteresis loops.

The comparative analysis demonstrated the trade-offs between speed and precision, with the Genetic Algorithm showing clear advantages for complex simulations. This chapter established the VRM's potential and the importance of choosing suitable optimization techniques to model timber connections under cyclic loading accurately.

Par.	s	Initial Values x_0	Lower Bounds l_b	Upper Bounds u_b	Optimized Values by *fminsearch*	Optimized Values by GA
k_b	+	0.70	0	10	0.12	0.83
	-	0.70	0	10	0.23	1.15
f_0	+	2.0	0	10	2.24	7.84
	-	2.0	0	10	3.41	5.78
α	+	4.1	-10	10	1.63	1.87
	-	4.1	-10	10	1.29	1.14
β_1	+	0.1	-10	10	4.22	-2.53
	-	-0.02	-10	10	-3.15	-4.10
β_2	+	0.8	-10	10	0.16	0.02
	-	-1.35	-10	10	-0.18	0.11
γ_1	+	0.0	-10	10	-0.07	2.54
	-	0.0	-10	10	-0.68	1.46
γ_2	+	-1.0	-10	10	-3.79	0.62
	-	0.0	-10	10	-0.30	1.42
γ_3	+	-1.0	-10	10	-43.60	7.73
	-	0.0	-10	10	0.08	-4.34

Table 3.2. VRM Parameters used as initial values and optimized by *fminsearch* and Genetic Algorithm to simulate the hysteresis loop in Figure 3.9a.

	Execution time (sec)	n. iterations	Value of Objective Function	error (%)
fminsearch	0.2467	2461	83.6990	2.09
GA	20.2215	2500	57.8487	3.58

Table 3.3. Comparison between *fminsearch* and Genetic Algorithm to simulate the hysteresis loop in Figure 3.9a.

Par.	s	Initial Values x_0	Lower Bounds l_b	Upper Bounds u_b	Optimized Values by *fminsearch*	Optimized Values by GA
k_b	+	0.25	0	20	0.19	0.31
	-	0.10	0	20	0.22	0.27
f_0	+	4.5	0	20	3.04	3.95
	-	2.0	0	20	1.10	2.43
α	+	3.5	-20	20	6.43	5.63
	-	1.5	-20	20	2.16	2.40
β_1	+	0.0	-20	20	-0.02	2.04
	-	0.0	-20	20	-0.01	0.39
β_2	+	0.0	-20	20	-0.01	0.01
	-	0.6	-20	20	0.0	-0.30
γ_1	+	0.4	-20	20	1.29	0.47
	-	1.0	-20	20	0.20	1.02
γ_2	+	1.0	-20	20	0.24	0.25
	-	1.0	-20	20	1.18	0.46
γ_3	+	1.0	-20	20	-3.95	-0.94
	-	-2.0	-20	20	1.99	-4.42

Table 3.4. VRM Parameters used as initial values and optimized by *fminsearch* and Genetic Algorithm to simulate the hysteresis loop in Figure 3.9b.

	Execution time (sec)	n. iterations	Value of Objective Function	error (%)
fminsearch	0.2864	2451	22.4682	3.52
GA	31.0657	2500	22.5307	2.51

Table 3.5. Comparison between *fminsearch* and Genetic Algorithm to simulate the hysteresis loop in Figure 3.9b.

Par.	s	Initial Values x_0	Lower Bounds l_b	Upper Bounds u_b	Optimized Values by *fminsearch*	Optimized Values by GA
k_b	+	0.25	0	10	1.20	0.63
	-	1.10	0	30	1.37	1.34
f_0	+	15.1	0	30	20.61	22.99
	-	15.1	0	30	13.28	15.93
α	+	0.5	-10	10	0.33	0.39
	-	1.5	-10	10	0.35	0.57
β_1	+	0.0	-10	10	-0.01	-6.05
	-	0.0	-10	10	-0.02	0.83
β_2	+	0.0	-10	10	0.07	-0.05
	-	0.0	-10	10	-0.04	0.14
γ_1	+	0.0	-10	10	0.74	1.79
	-	0.0	-10	10	3.46	-1.90
γ_2	+	0.0	-10	10	-10.06	-1.17
	-	0.0	-10	10	-0.01	0.55
γ_3	+	1.0	-10	10	-6.26	10.0
	-	-2.0	-10	10	12.42	9.05

Table 3.6. VRM Parameters used as initial values and optimized by *fminsearch* and Genetic Algorithm to simulate the hysteresis loop in Figure 3.9c.

	Execution time (sec)	n. iterations	Value of Objective Function	error (%)
fminsearch	0.3809	2415	639.73	2.11
GA	29.0804	2500	502.56	1.01

Table 3.7. Comparison between *fminsearch* and Genetic Algorithm to simulate the hysteresis loop in Figure 3.9c.

Par.	s	Initial Values x_0	Lower Bounds l_b	Upper Bounds u_b	Optimized Values by *fminsearch*	Optimized Values by GA
k_b	+	0.70	0	10	-4.76	0.72
	-	0.50	0	10	2.32	2.17
f_0	+	2.0	0	10	-9.88	9.60
	-	2.0	0	10	5.66	1.60
α	+	4.10	-10	10	0.38	0.43
	-	3.0	-10	10	0.19	10.0
β_1	+	0.10	-10	10	0.14	-10.0
	-	-0.02	-10	10	-0.04	2.83
β_2	+	0.80	-10	10	-0.55	0.22
	-	-1.35	-10	10	-0.42	7.20
γ_1	+	0.0	-10	10	-0.07	4.19
	-	0.0	-10	10	0.04	-3.82
γ_2	+	-1.0	-10	10	-11.86	1.00
	-	0.0	-10	10	0.02	-1.63
γ_3	+	-1.0	-10	10	-3.37	0.76
	-	0.0	-10	10	0.05	-5.07

Table 3.8. VRM Parameters used as initial values and optimized by *fminsearch* and Genetic Algorithm to simulate the hysteresis loop in Figure 3.9d.

	Execution time (sec)	n. iterations	Value of Objective Function	error (%)
fminsearch	0.7089	2448	6974.83	17.32
GA	101.3538	2500	149.33	1.08

Table 3.9. Comparison between *fminsearch* and Genetic Algorithm to simulate the hysteresis loop in Figure 3.9d.

Chapter 4

Simulation of Experimental Hysteretic Loops

4.1 Summary of Chapter 4

Based on the experimental hysteretic loops introduced in Chapter 2 and the Vaiana-Rosati Model (VRM) discussed in Chapter 3, this chapter will focus on simulating four experimental loops, each representing a different connection type: angle bracket, hold-down, beam-to-pillar, and single shear wall connection. The VRM will be applied to simulate these loops, starting with carefully interpreting model parameters. The calibration process begins with the first loading cycles and extends to subsequent cycles, showcasing how parameters evolve in relation to the dissipated energy.

Key observations will be made, particularly in comparing the errors between the experimental and simulated loops based on the work dissipated. Additionally, the trends of the model parameters during the loading and unloading phases will be examined in relation to energy dissipation. A particular focus is placed on the angle bracket connection, which is simulated using the genetic algorithm. This will provide an opportunity to analyze the advantages of optimization methods and identify challenges for future improvements.

The chapter concludes by assessing the overall performance of these simulations and their alignment with experimental data, offering insights into the potential enhancements that can be achieved through optimization techniques.

4.2 Introduction

The behavior of timber structures under seismic loading is a critical area of study, particularly in regions prone to earthquakes. Understanding how these structures respond during seismic events ensures their safety and resilience. In Chapter 2, we analyzed various typologies of timber connections, focusing on their experimental performance under cyclic loading. The hysteretic behavior observed in these experiments provides valuable insights into the energy dissipation, stiffness degradation, and overall dynamic response of timber joints and assemblies.

This chapter aims to simulate the experimental hysteretic loops discussed in Chapter 2 using the Vaiana-Rosati Model (VRM) introduced in Chapter 3. This model, which was developed to capture the complex nonlinear behavior of structures under cyclic loading, will be applied to replicate the observed hysteretic responses. The objective is to evaluate the model's accuracy and reliability and extract some physical data by comparing the simulated loops with the experimental data.

We will begin by providing an overview of the selected experimental hysteretic loops, outlining the criteria used for their selection and their relevance to the study. Following this, we will describe the methodology employed for the simulations, including model calibration, assumptions, and the computational approach. The results of the simulations will be presented and analyzed, with a focus on how well the models capture the key characteristics of the experimental loops. Additionally, we will conduct a sensitivity analysis to assess the influence of various parameters on the simulation outcomes. This chapter thus serves as a critical evaluation of the VRM's ability to simulate the hysteretic behavior of timber structures. It contributes to a deeper understanding of their seismic performance and provides insights that can inform future design and analysis efforts.

4.3 Overview of Selected Experimental Hysteretic Loops

In Chapter 2, we thoroughly analyzed a variety of timber connections, focusing on their performance under seismic loading conditions. For each category—angle brackets, hold-downs, beam-to-pillar connections, and single shear wall connections— we selected two representative experimental hysteretic loops that exemplify the typical behavior of these connections under cyclic loading. These loops were chosen based on their relevance to the most common types of timber structures used in seismic regions and their ability to illustrate key characteristics such as energy dissipation, stiffness degradation, and failure modes. The

studied experimental loops provide a comprehensive view of the cyclic behavior of timber connections, showcasing the diverse ways these elements respond to seismic forces. For instance, the angle brackets and hold-downs represent commonly used metal connectors that play a crucial role in anchoring timber elements. At the same time, the beam-to-pillar and shear wall connections are critical for maintaining the overall integrity and stability of timber frames.

For the angle bracket and hold-down categories, we selected the experimental loops derived from the test specimens Gavric, Ceccotti, and Fragiacomo studied in their research [30] and showed in Figure 2.11a and Figure 2.14a. These connections were chosen for several reasons. Firstly, the experimental data provided by these authors offers a clear and detailed representation of each hysteretic loop, facilitating accurate analysis and simulation. Secondly, the selected loops exhibit key phenomena dominant in timber connections under seismic loads, such as pinching effects and secant stiffness degradation. Additionally, the study by Gavric et al. provides a detailed account of the connections' behavior when subjected to cyclic loads in both directions. This aspect is crucial for understanding the full range of their performance under seismic conditions. This bidirectional loading information is particularly relevant for the global dynamic analysis that will be discussed in subsequent chapters.

Regarding the beam-to-pillar connection category, we have selected the specimen tested by Fairweather in his Master Thesis [28]. The decision to use this particular specimen is based on two main considerations. First, as shown in Figure 2.23a, the experimental data from this test offer a clear and well-defined representation of each hysteretic loop, making it ideal for simulation purposes. This clarity is essential for accurately capturing the features of the connection's cyclic behavior. Second, the design of the beam-to-pillar connection tested by Fairweather is highly representative of common practice in timber construction. The connection utilizes metallic plates to join vertical and horizontal elements, a method frequently employed in the industry.

The selection process was slightly different for the category of single-shear wall connections due to the inherent similarities across various experimental studies in the literature. These similarities stem from consistent design aspects and standardized loading protocols used in testing shear wall connections. Given this uniformity, our primary criterion for selecting the experimental loop was the clarity and ease of reading the individual loops, which is crucial for accurate simulation and analysis. Consequently, we chose the specimen presented in the study by Dong et al. [26]. This particular experiment was selected because it provides a clear and distinct representation of the hysteretic loops, making it an excellent candidate for simulation. The well-documented behavior of the single shear wall connection in this study and its clear loop formation allows for a precise comparison between the simulated and experimental data.

4.4 Simulation Methodology

The simulation methodology for replicating the experimental hysteretic loops involves a detailed calibration process, which is crucial for accurately capturing the complex behavior observed during cyclic loading. This process is structured in several key steps, focusing on identifying and adjusting model parameters to simulate the main phenomena affecting the loops throughout the loading history.

The first step in the calibration process is to identify the main phenomena influencing the shape and behavior of the hysteretic loops. First, there is the pinched loop shape. This characteristic is typically observed in connections with significant energy dissipation, leading to a narrowing of the loop during unloading and reloading cycles. Then, there is the phenomenon of shifting the inflection point. This occurs when the inflection point of the loop's limiting curves shifts from one cycle to the next, indicating changes in the connection's stiffness or damping characteristics. Finally, the slope and strength degradation variation reflects the material's response to accumulated damage.

To simulate these phenomena, specific VRM parameters are adjusted. The sensitivity analysis of these parameters, discussed in Chapter 3, guides the calibration process:

- the parameter f_0 is primarily responsible for managing the variations in amplitude during the loading cycle. By adjusting f_0 the model can simulate the changing amplitude observed in the experimental loops as the connection undergoes cyclic loading;
- the slope of the limiting curves, which reflects the connection's stiffness, is controlled by the parameters β_1 and β_2. Adjusting these parameters allows the model to replicate the observed changes in stiffness as the loading progresses;
- if the experimental loop exhibits a pinched shape, this behavior is captured by modifying the parameters γ_1, γ_2, and γ_3. Specifically, γ_3 is crucial when the inflection point of the loop shifts from cycle to cycle, requiring precise adjustments to match the observed experimental behavior.

Once the fundamental phenomena have been identified and the relevant parameters are adjusted, the initial experimental cycles —often exhibiting instability in shape and features— are removed from consideration. This exclusion is necessary to avoid the influence of these unstable characteristics on the calibration process. The calibration then begins with a single, stable cycle from the loading history. During this phase, a sinusoidal displacement with increasing amplitude is applied, and the model parameters are manually varied to achieve the best fit to the selected cycle of each experimental loop. The initial set of parameters used

for this purpose is detailed in Table 4.1. The effectiveness of this calibration is visually demonstrated in Figure 4.1, where the simulated first cycle is overlaid on the corresponding experimental cycle, showing the close alignment achieved between the model and the experimental data.

Fig	s	k_b	f_0	α	β_1	β_2	γ_1	γ_2	γ_3
4.1a	+	0.18	11	1.1	-0.2	0.03	4.1	0.6	6.2
	-	0.2	12	1.0	-0.2	0.03	4.8	0.7	-6.2
4.1b	+	0.25	4.5	3.5	0.01	0.01	0.4	1.0	2.5
	-	0.1	1.7	1.6	0.01	0.01	0.6	1.0	-2.5
4.1c	+	0.1	21	0.5	0.0	0.0	10	0.2	5.0
	-	0.6	10	0.25	0.0	0.0	5.0	0.4	-7.0
4.1d	+	-0.001	0.5	5.0	0.4	0.1	0.2	3.0	0.8
	-	-0.001	0.5	5.0	0.4	0.1	0.2	2.5	-1.0

Table 4.1. Initial set of VRM parameters adopted for simulating the first cycles of the experimental hysteresis loops shown in Figure 4.1

After successfully simulating the first cycle, the next step involves linking the variation of the model parameters to the energy dissipated during the subsequent cycles. As demonstrated in Chapter 3, the formulation of the VRM facilitates the point-by-point computation of dissipated energy using a straightforward closed-form analytical expression. The energy dissipation values throughout the loading history can be used to adjust the model parameters manually to reflect the observed behavior in the experimental loops. This approach allows for precise manipulation of the loop shape in each cycle, effectively simulating the strength and secant stiffness degradation that occurs due to cyclic loading.

The final step involves comparing the parameters used for the first and last cycles. Table 4.2 presents these sets, with the values in bold indicating the parameters that were varied throughout the simulation to replicate the changes in loop shape and behavior. This comparison is essential for validating the model's ability to simulate the degradation and other key phenomena observed in the experimental data.

Following this structured calibration methodology, the VRM can be fine-tuned to accurately replicate the complex hysteretic behavior of timber connections under cyclic loading. This process enhances the model's predictive capabilities and provides valuable insights into the dynamic performance of timber structures in seismic areas.

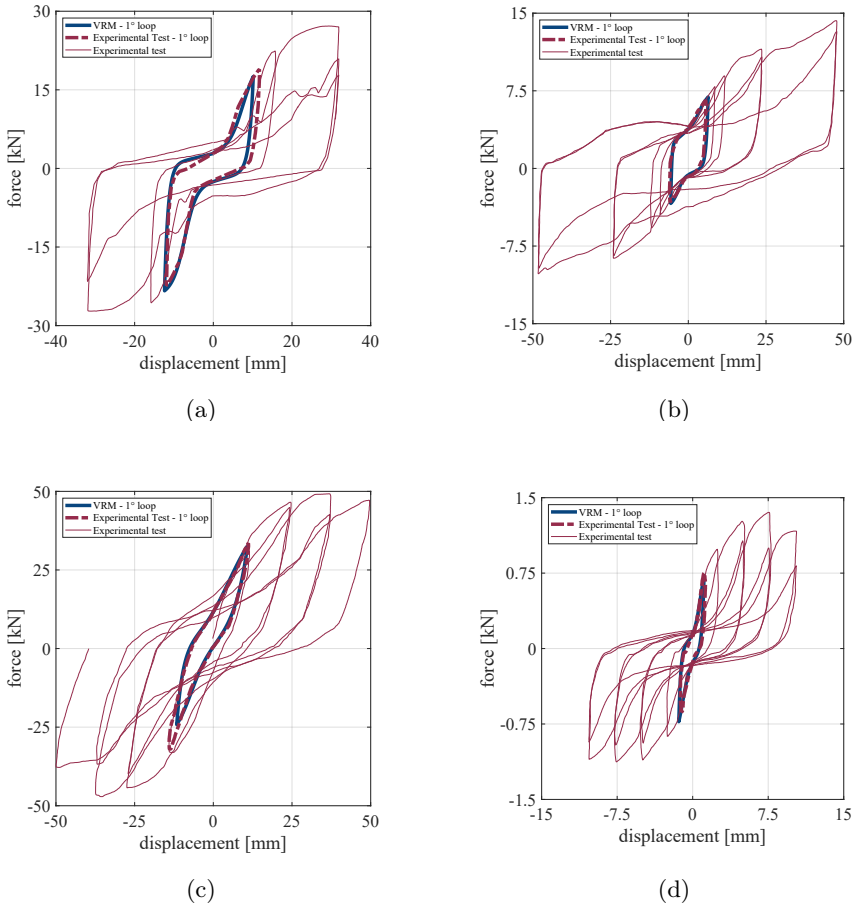


Figure 4.1. Simulation of the first cycle of the experimental hysteresis loops using the VRM: (a) angle bracket and (b) hold-down tested by Gavric et al.[30], (c) beam-to-pillar connection tested by Fairweather [28] and (d) single shear wall tested by Dong et al. [26]

4.5 Results of Simulations and Discussion

The results of the simulations, conducted using the calibrated VRM and shown in Figure 4.2, demonstrate a strong correlation with the experimental hys-

Fig	s	k_b	f_0	α	β_1	β_2	γ_1	γ_2	γ_3
4.2a	+	0.18	11	1.1	-0.2	0.03	4.1	0.6	**31.03**
	-	0.2	12	1.0	-0.2	0.03	**3.56**	0.7	**-31.03**
4.2b	+	**0.52**	**7.80**	3.5	**1.06**	0.01	**2.25**	**0.14**	**42.08**
	-	**0.008**	**6.32**	**0.55**	**1.06**	0.01	**2.18**	**0.21**	**-42.08**
4.2c	+	**0.25**	**23.08**	**0.25**	0.0	0.0	**4.89**	0.2	**27**
	-	**0.23**	**16.22**	0.25	0.0	0.0	5.0	**0.2**	**-24.85**
4.2d	+	-0.001	0.5	**1.35**	**0.5**	**0.02**	0.2	**0.92**	**10.86**
	-	**0.0015**	0.5	**1.29**	**0.5**	**0.02**	0.2	**0.99**	**-11.06**

Table 4.2. Final set of VRM parameters adopted for simulating the experimental hysteresis loops shown in Figures 4.2 changed as a function of the generalized work.

teretic loops for each category of timber connections. The comparison between the simulated and experimental data highlights the model's effectiveness in capturing the key phenomena such as pinching, stiffness degradation, and strength reduction observed during cyclic loading.

Figure 4.2a illustrates the comparison between the experimental and simulated loop of the angle bracket connection, showcasing the accuracy of the simulation in reproducing the complex behavior of these connections. The simulated loop closely replicates the pinched shapes and the gradual degradation in stiffness and strength observed in the experimental data. As the first two lines of Table 4.2 show, the VRM parameters were adjusted during the calibration process, specifically modifying the parameter γ_3 to simulate the shift of the inflection point of the limiting curves from one cycle to the next one. This adjustment accurately represents the transition of the limiting curves from an *S3*-shape (with one inflection point) to an *S2*-shape (a simple curve), which corresponds to the final phases of the loading history characterized by secant stiffness and strength degradation.

The simulated loop of the hold-down connection, shown in Figure 4.2b, demonstrates the VRM's capability to replicate the experimental behavior of the connection closely. The model accurately simulates the increase in strength during the initial stages of the loading history, followed by the eventual degradation of stiffness. Notably, a peculiar shape is observed in the final cycles, likely due to the instability of the connection before collapse. An approximation in the calibration was made to address this, focusing on accurately capturing the maximum force and displacement values rather than the entire loop shape. Unlike the angle bracket loop, where the transition between cycles is faster, the hold-down

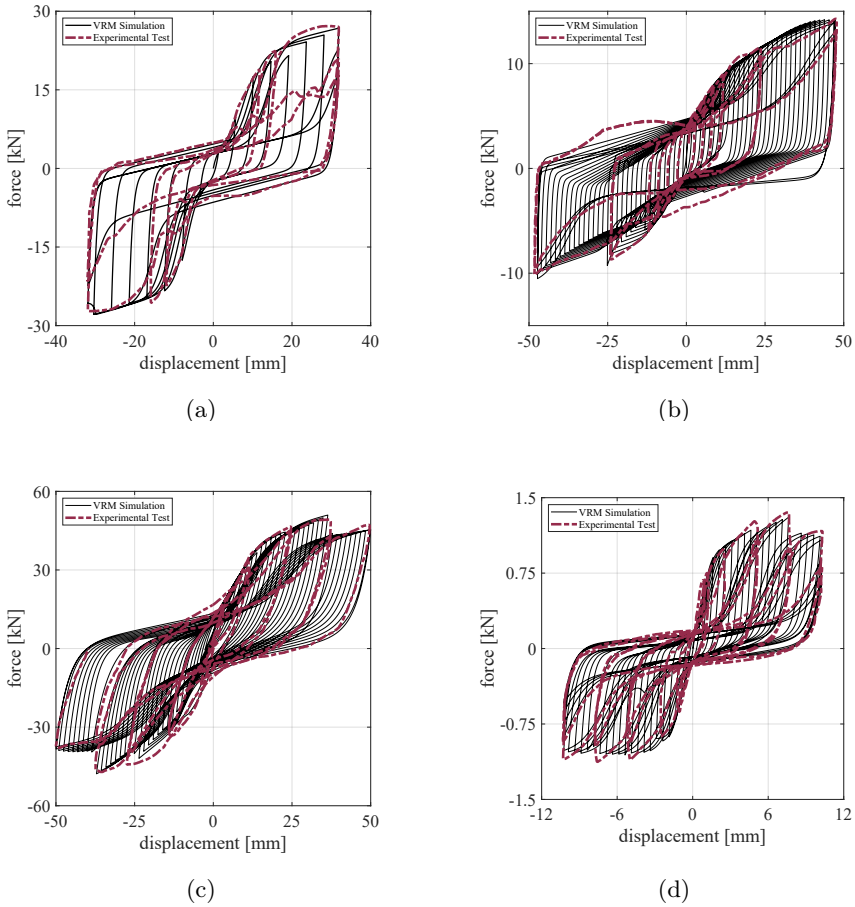


Figure 4.2. Simulation of the experimental hysteresis loops using the VRM: (a) angle bracket and (b) hold-down tested by Gavric et al.[30], (c) beam-to-pillar connection tested by Fairweather [28] and (d) single shear wall tested by Dong et al. [26]

connection requires more internal cycles to achieve a significant change in shape from the initial to the final cycles. Upon examining Table 4.2, which presents the final set of parameters used in the simulation, it is evident that nearly all parameters underwent variations to accurately simulate the evolving loop shape. Notably, there is a significant variation in the loop width, effectively captured by

increasing the value of the parameter f_0. Additionally, the substantial increase in the values of parameters γ_1 and γ_3 contributes to achieving a slight symmetry in the final cycles. This adjustment is crucial for simulating the shift of the inflection point between the limiting curves, reflecting the complex behavior observed in the experimental data.

As in the cases previously considered, the loop exhibited by the beam-to-pillar connection can be successfully simulated by the model, as shown in Figure 4.2c. The variation of parameters k_b and α slightly adjusts the tangent stiffness and the slope of the loop, allowing for fine-tuning of the initial stiffness and subsequent response. The parameter f_0 is instrumental in softly increasing the amplitude of the cycles, which is critical in matching the overall energy dissipation observed in the experimental data. The pinching effect and stiffness degradation, which become more pronounced as the loading history progresses, are effectively simulated by manipulating the γ_3 parameter. This parameter adjustment ensures that the model can replicate the progressive narrowing of the loop and the reduction in stiffness, characteristic of the connection's response under cyclic loading. Similar to the hold-down connection, the simulation of the beam-to-pillar connection requires the model to generate more intermediate cycles to capture the detailed variation in loop shape accurately. This approach allows the model to mimic the gradual changes in the experimental cycles, ensuring that the transition between different stages of the loading history is well-represented.

The simulation results for single-shear wall connections also strongly correlate with the experimental data, as depicted in Figure 4.2d. When comparing the initial set of parameters listed in Table 4.1 with the final parameters in Table 4.2, it is evident that nearly all parameters underwent adjustments. However, unlike the previous cases, the parameter f_0, which governs the amplitude of the loop, remains unchanged. This stability is due to the consistent amplitude of the loop throughout the loading history, indicating a different energy dissipation pattern compared to the other connection types. To accurately simulate the behavior observed in the experimental data, a substantial reduction in the parameter α was necessary to reflect the decreased slope of the loops, particularly near the horizontal axis. Additionally, the pinching phenomenon and the shift of the inflection point in the limiting curves were effectively simulated by varying the parameter γ_3, which plays a crucial role in capturing the complex, non-linear behavior typical of single-shear wall connections under cyclic loading.

A way to verify the degree of correspondence between the experimental loops and the simulated ones is to compare the dissipated energy for each cycle. As illustrated in Figure 4.3, we observe distinct trends that offer a more comprehensive view of the dynamic behavior of the connections during cyclic loading. Table 4.4 provides the corresponding numerical values for both the experimental and simulated loops, emphasizing the differences in energy dissipation and further

validating the model's accuracy.

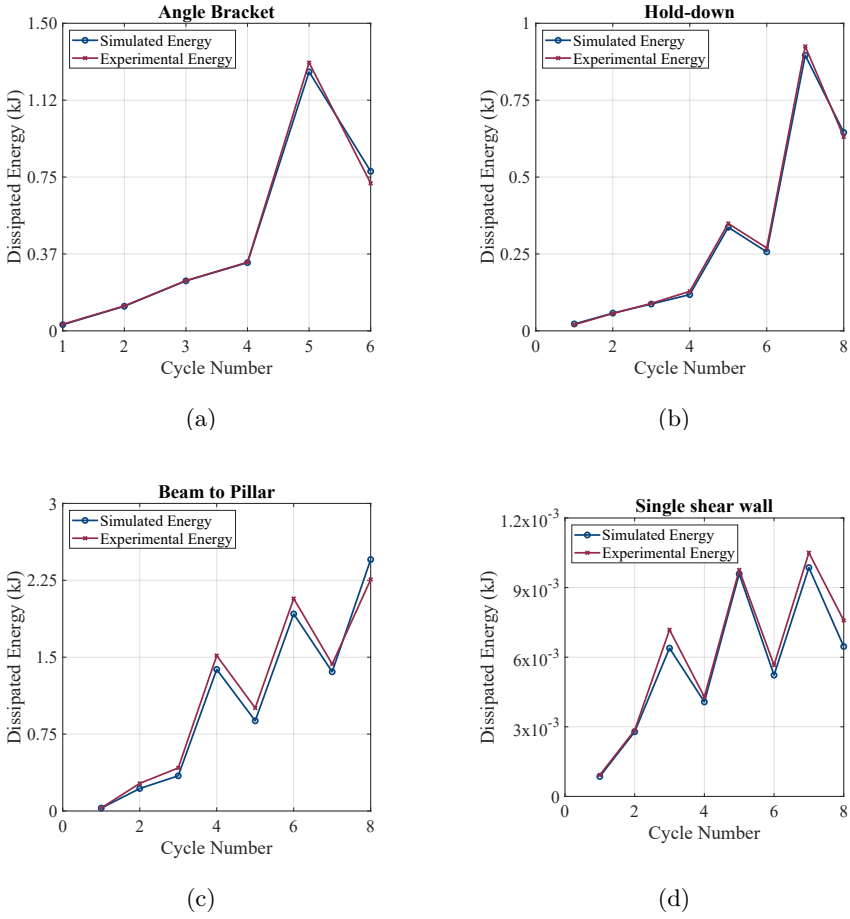


Figure 4.3. Comparison of the dissipated energy per cycle between the experimental hysteresis loop and the simulated one by the use of the VRM: (a) angle bracket and (b) hold-down tested by Gavric et al.[30], (c) beam-to-pillar connection tested by Fairweather [28] and (d) single shear wall tested by Dong et al. [26]

The dissipated energy per cycle increases gradually for the angle bracket connection (Figure 4.3a). It decreases drastically in the final cycle, reflecting the typical stiffness and strength degradation observed experimentally. Considering

Case	Fig.	n. Cycle	W_{sim} [kJ]	W_{exp} [kJ]	Error [kJ]	Error [%]
a	4.2a	1	28.05	30.29	2.24	7.40
		2	112.01	113.53	1.52	1.34
		3	227.55	228.66	1.10	1.34
		4	310.49	312.42	1.93	0.62
		5	1178.94	1221.03	42.09	3.45
		6	726.07	671.61	54.46	8.11
b	4.2b	1	22.38	19.98	2.40	12.01
		2	57.66	56.51	1.15	2.03
		3	87.13	89.22	2.09	2.34
		4	117.82	128.58	10.76	8.37
		5	336.71	349.02	12.31	3.53
		6	256.83	269.41	12.58	4.67
		7	896.03	925.14	29.11	3.15
		8	645.26	630.59	14.67	2.33
c	4.2c	1	28.17	29.51	1.35	4.56
		2	219.00	269.02	50.02	18.59
		3	343.00	419.95	76.96	18.33
		4	1380.95	1515.31	134.35	8.87
		5	879.72	1004.88	125.17	12.46
		6	1922.04	2071.93	149.88	7.23
		7	1357.48	1432.94	75.46	5.27
		8	2452.90	2257.95	194.95	8.63
d	4.2d	1	0.86	0.93	0.07	7.45
		2	2.79	2.85	0.06	2.21
		3	6.39	7.18	0.79	11.00
		4	4.07	4.29	0.22	5.10
		5	9.59	9.76	0.17	1.75
		6	5.23	5.66	0.43	7.63
		7	9.86	10.50	0.64	6.10
		8	6.46	7.59	1.12	14.82

Table 4.3. Comparison of the dissipated energy per cycle between the experimental hysteresis loops and the simulated one shown in Figures 4.2.

Table 4.4a, the error remains under 10% for most cycles, with the largest deviation (8.11%) occurring in the final cycle. The close agreement in the early cycles underscores the model's ability to replicate this connection's stiffness degradation and pinching behavior. Similar considerations can be made in the case of the hold-down connection (Figure 4.3b); the energy increases gradually, but it presents a more rapid reduction in dissipated energy during the trailing cycles. This steep decline suggests that the hold-down connection is highly effective in energy dissipation during the first few cycles but becomes less efficient as it approaches failure. The error fluctuates slightly more, particularly in the early and middle cycles, where the error reaches up to 12.01% in the first cycle. The model captures the general trend of energy dissipation but shows some deviations as the cycles progress. This might be attributed to the shear action used in the experimental test, which is not the ideal loading condition for hold-down connections that primarily resist axial forces. In the case of the beam-to-pillar connection (Figure 4.3c), the dissipated energy has an up-and-down trend due to the different trailing internal cycles during the loading history. Analyzing the data presented in Table 4.4c, it is possible to notice a moderate difference between experimental and simulated energy dissipation. The largest discrepancy occurs in cycles 2 and 3, where the error surpasses 18%. The later cycles exhibit improved accuracy, with the error falling below 10%. These results suggest that the VRM model captures the general behavior but may need further adjustments to simulate the early cycle dynamics more accurately. Finally, the single-shear wall connection shown in Figure 4.3d exhibits a stable energy dissipation profile, with minimal variation between cycles. Relating to the error between the simulated and experimental dissipated energy, it is possible to notice a relatively small discrepancy in the first few cycles, with errors mostly under 10%. However, the error increases to 14.82% in the final cycle. Despite the modest differences, the overall agreement between simulated and experimental values highlights the VRM's ability to simulate this connection, particularly considering the constant amplitude and limited strength resistance observed in the experiments.

The comparison of dissipated energy between experimental and simulated cycles across all connection types underscores the VRM model's effectiveness in capturing the complex cyclic behavior of timber connections. In most cases, the errors are within acceptable ranges, indicating that the model is well-calibrated to replicate key phenomena like pinching, stiffness degradation, and strength reduction. The variation of energy dissipation provides a useful metric for assessing the model's performance in different loading history phases, and the observed deviations offer insight into potential areas for further refinement.

To further investigate the dynamic behavior of timber connections and evaluate the model's effectiveness in simulating these complex interactions, we focus on the variation of the VRM parameters during cyclic loading for one of the four

previously discussed cases—specifically, the angle bracket connection shown in Figure 4.2a. The parameters were systematically adjusted for each cycle to reflect the changes observed in the connection's hysteretic response. This detailed analysis allows for a deeper understanding of how individual parameters influence the overall system behavior. Figures 4.4-4.11 illustrate the variation of these parameters across different cycles, where values corresponding to the loading phase are highlighted in red, and those from the unloading phase are shown in blue.

While the parameter variations do not strictly follow a specific pattern, we observe that in the final cycles, the loading and unloading phases converge to nearly identical values, suggesting a trend toward symmetry in the loop shape. In particular, Figure 4.8 demonstrates that after the second cycle, the values of β_2^+ and β_2^- stabilize, which is significant because this parameter heavily influences the curvature of the limiting curves. Additionally, the parameter γ_3 variation, illustrated in Figure 4.11, reveals an interesting trend: positive values are associated with the loading phase, while negative values appear in the unloading phase. This behavior is consistent with the need to achieve a more symmetric hysteresis loop. Such observations provide valuable insights into how the VRM parameters affect the overall accuracy and symmetry of the simulated response.

4.5.1 Application of Optimization Methods

The optimization methods introduced in Chapter 3 are applied here to improve the simulation accuracy of timber connections, with a particular focus on the angle bracket connection. Building on the findings from Chapter 3, where both the *fminsearch* method and Genetic Algorithm (GA) were analyzed for parameter optimization, the GA was chosen for its superior capability in navigating complex, non-linear parameter spaces and locating global optima. This study employs the GA to refine the model parameters initially calibrated manually, as shown in Figure 4.2a, ensuring a more precise and reliable simulation of the hysteresis behavior.

The optimization begins by initializing the GA with the initial model parameters manually calibrated and displayed in Table 4.1a. Each parameter is bounded within a permissible range to ensure the parameters remain within realistic and physically meaningful limits. For example, parameters such as k_b and f_0 are constrained to positive values based on the assumptions of the VRM model. This bounding process not only ensures the physical validity of the parameters but also narrows the search space, thereby improving the efficiency and convergence rate of the GA.

The objective function for this optimization is designed to minimize the discrepancy between the experimental force (f_{exp}) and the simulated force (f_{sim}) generated using the VRM. This gap is quantified using the root mean square

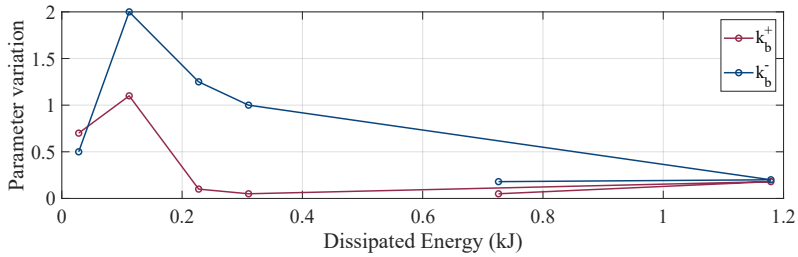


Figure 4.4. Variation of the k_b parameter in function of the dissipated energy in the case of the simulated hysteretic loop of the angle bracket tested by Gavric et al.[30]

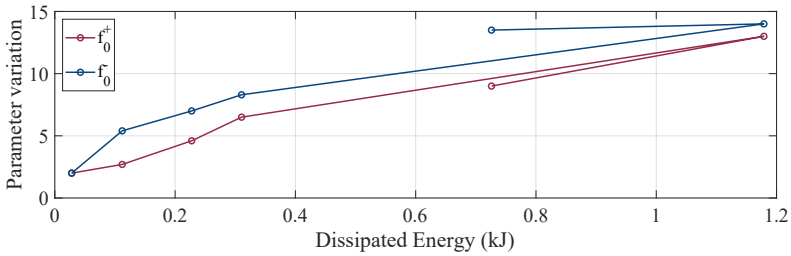


Figure 4.5. Variation of the f_0 parameter in function of the dissipated energy in the case of the simulated hysteretic loop of the angle bracket tested by Gavric et al.[30]

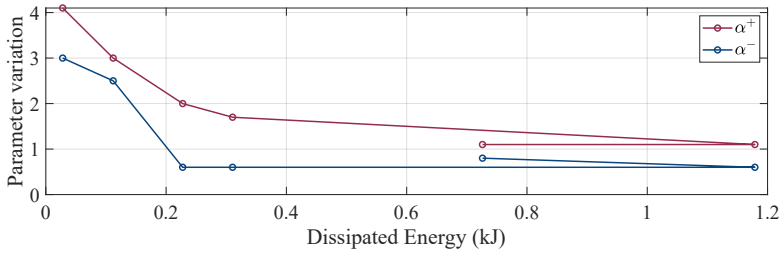


Figure 4.6. Variation of the α parameter in function of the dissipated energy in the case of the simulated hysteretic loop of the angle bracket tested by Gavric et al.[30]

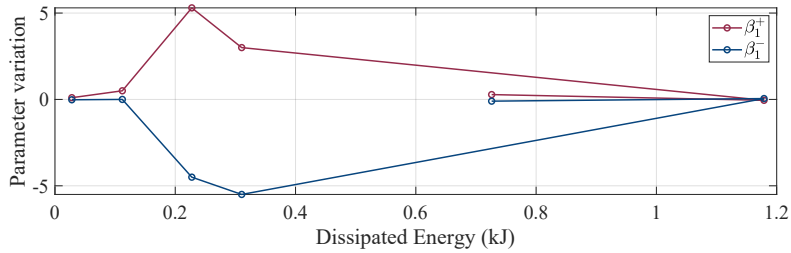


Figure 4.7. Variation of the β_1 parameter in function of the dissipated energy in the case of the simulated hysteretic loop of the angle bracket tested by Gavric et al.[30]

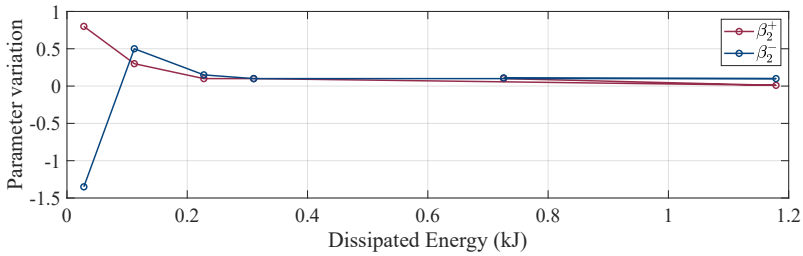


Figure 4.8. Variation of the β_2 parameter as a function of the dissipated energy in the case of the simulated hysteretic loop of the angle bracket tested by Gavric et al.[30]

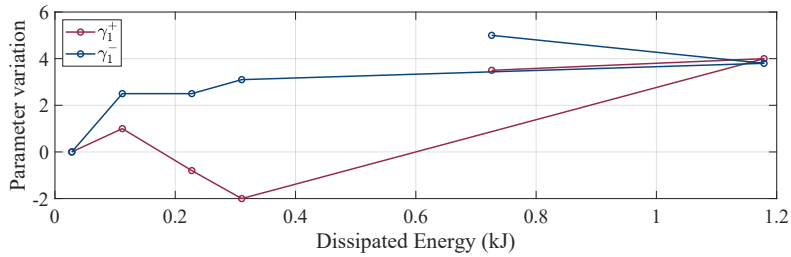


Figure 4.9. Variation of the γ_1 parameter in function of the dissipated energy in the case of the simulated hysteretic loop of the angle bracket tested by Gavric et al.[30]

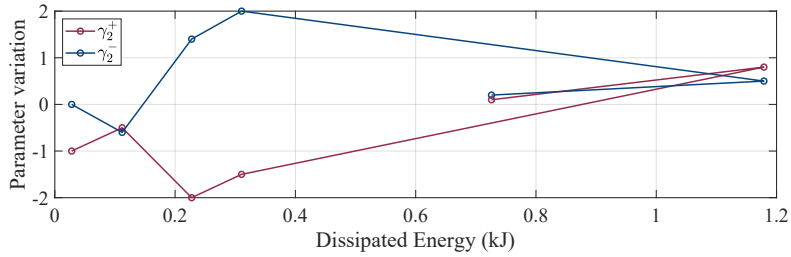


Figure 4.10. Variation of the γ_2 parameter in function of the dissipated energy in the case of the simulated hysteretic loop of the angle bracket tested by Gavric et al.[30]

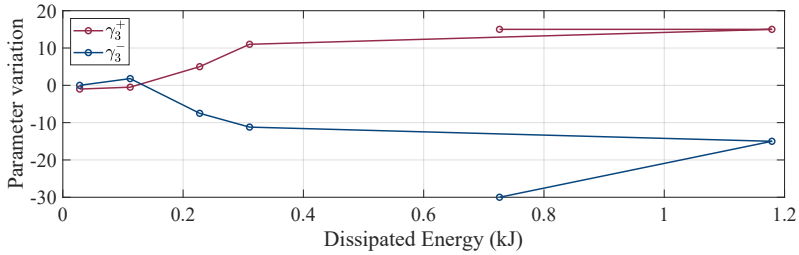


Figure 4.11. Variation of the γ_3 in function of the dissipated energy in the case of the simulated hysteretic loop of the angle bracket tested by Gavric et al.[30]

(RMS) error, which provides an average measure of the differences between the experimental and simulated forces:

$$\text{error} = \sqrt{\frac{1}{n}\sum_{i=1}^{n}(f_{exp} - f_{sim})^2} \tag{4.1}$$

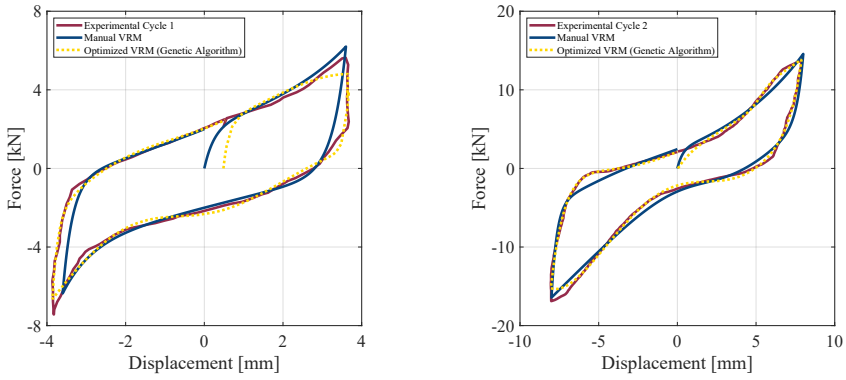
where n represents the total number of data points in the cycle.

By iteratively adjusting the model parameters, the GA minimizes the RMS error, resulting in an optimal parameter set that best fits the experimental data. The number of iterations and generations is customized to balance the desired accuracy and computational efficiency.

The optimized simulation results in Figures 4.12-4.13 in yellow demonstrate that the GA effectively replicates the experimental hysteresis loops. The optimized model successfully captures key characteristics such as stiffness, pinching effects, and peak values of displacement and force, achieving a good level of accuracy within seconds. However, some challenges remain, particularly in cases where the cycle's limiting curves exhibit $S3$ type behavior. Here, the correct positioning of inflection points proves difficult, suggesting that manual fine-tuning of parameters γ_1, γ_2, and γ_3 may be necessary after the automated optimization process to achieve a more precise fit. This issue can be noticed in Figures 4.13c-d, where the inflection points of the unloading curves are more pronounced than in the other cycles.

Figures 4.14-4.21 compare the parameter variation during the loading and unloading phases for both the manually calibrated and GA-optimized models. In most cases, the parameters in the penultimate cycles converge toward symmetry between the loading and unloading phases. Moreover, parameters such as k_b, α, β_2, γ_1, and γ_2 in the optimized solution closely align with those from the manual calibration, indicating that the manual approach was near-optimal. However, for parameters like f_0, β_1, and γ_3, the optimized values deviate more significantly, highlighting that multiple parameter combinations can produce similar loop shapes.

The application of the genetic algorithm resulted in noticeable improvements in the simulation's accuracy. By comparing the work values from the manually calibrated simulations and those optimized by the genetic algorithm, as shown in Table 4.4, it is evident that the optimization process yields a better match to the experimental data. For instance, the error percentages for the optimized simulations (W_{opt}) are generally lower than those for the manually calibrated simulations (W_{sim}), indicating a closer correspondence to the experimental hysteresis loops. Adjustments made to the model parameters during optimization were key to this improved accuracy. Parameters such as f_0 (loop amplitude),



(a) (b)

Figure 4.12. Comparison between the experimental angle bracket hysteresis loop tested by Gavric et al.[30] and the loops simulated by manually calibrating the VRM and using the genetic algorithm: (a) Cycle 1; (b) Cycle 2.

γ_3 (pinching and inflection point shift), and stiffness components (k_b^+, k_b^-) were refined to better replicate the observed behavior in the experimental data. These adjustments allowed the model to more precisely capture phenomena like stiffness degradation and the pinching effect, leading to a more accurate representation of the connection's dynamic response.

In conclusion, optimization techniques —particularly the genetic algorithm— have proven highly effective in improving the fidelity of simulated hysteresis loops, offering a more reliable tool for predicting the behavior of timber connections under seismic loading. Moving forward, significant progress would be made in applying automatic calibration to the entire hysteresis loop rather than individual cycles. This broader application has several advantages: it allows for the simultaneous optimization of multiple cycles, ensuring that the model captures long-term behavior, including cumulative damage effects and changes in stiffness over repeated cycles. Additionally, this approach could significantly reduce computational time by simplifying the process, eliminating the need for cycle-by-cycle manual adjustments, and ensuring global optimization across the entire response spectrum. As a result, the automatic technique would offer more consistent and comprehensive simulations, which are crucial for analyzing timber connections in realistic seismic scenarios where dynamic responses evolve. This enhanced efficiency and accuracy would make the model a powerful tool for both research and practical applications in structural design and assessment.

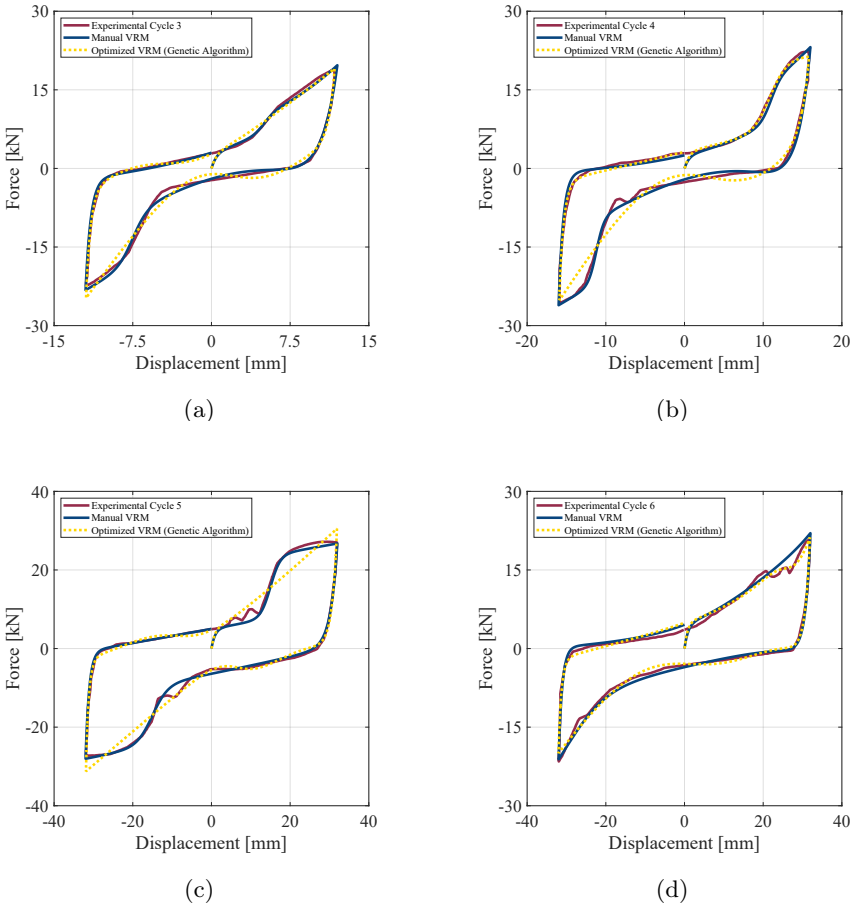


Figure 4.13. Comparison between the experimental angle bracket hysteresis loop tested by Gavric et al.[30] and the loops simulated by manually calibrating the VRM and using the genetic algorithm: (a) Cycle 3; (b) Cycle 4; (c) Cycle 5; (d) Cycle 6.

4.6 Conclusions of Chapter 4

Chapter 4 simulated four experimental hysteretic loops using the Vaiana-Rosati Model, focusing on typical timber connections, such as angle bracket, hold-

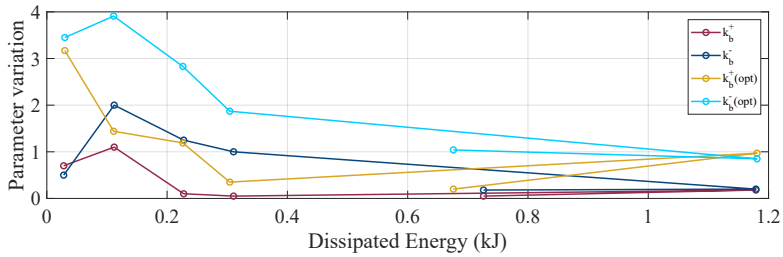


Figure 4.14. Variation of the k_b parameter as a function of the dissipated energy for the simulated hysteretic loop of the angle bracket (tested by Gavric et al.[30]) and the GA-optimized procedure.

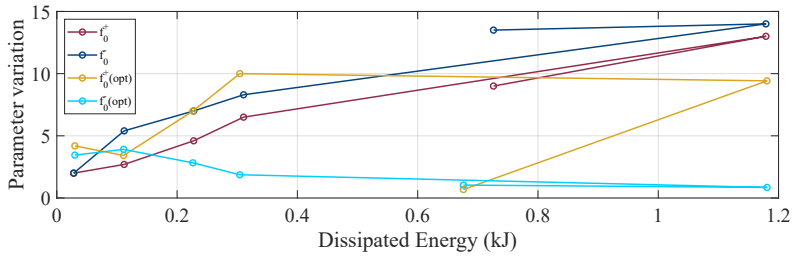


Figure 4.15. Variation of the f_0 parameter as a function of the dissipated energy for the simulated hysteretic loop of the angle bracket (tested by Gavric et al.[30]) and the GA-optimized procedure.

down, beam-to-pillar, and single shear wall connections. The VRM effectively captured key trends in energy dissipation and stiffness evolution, with a slight discrepancy in confront to the experimental data.

The approach of varying model parameters as an energy dissipation function successfully reproduced complex hysteretic behaviors. However, limitations arose due to the need for additional cycles to transition between loop shapes, complicating direct energy dissipation comparisons with experimental data.

The genetic algorithm applied to the angle bracket connection demonstrated the potential of optimization methods to enhance calibration accuracy, despite computational challenges and parameter sensitivity.

In summary, the VRM proved effective for modeling non-linear hysteretic be-

Fig.	n. Cycle	W_{exp} [kJ]	W_{sim} [kJ]	W_{opt} [kJ]	$Error_{sim}$ [%]	$Error_{opt}$ [%]
4.12a	1	30.29	28.05	29.99	7.40	0.99
4.12b	2	113.53	112.01	111.09	1.34	2.15
4.12c	3	228.66	227.55	226.25	1.34	1.05
4.12d	4	312.42	310.49	304.23	0.62	2.62
4.13a	5	1221.03	1178.94	1180.8	3.45	3.29
4.13b	6	671.61	726.07	676.03	8.11	0.66

Table 4.4. Comparison of the dissipated energy per cycle between the experimental hysteresis loop of the angle bracket tested by Gavric et al.[30] and the simulated loop by calibrating the VRM manually (W_{sim}) and by using an optimization technique, the Genetic Algorithm (W_{opt}).

havior, with optimization techniques offering significant improvements. Future work should refine parameter sensitivity and expand scenarios for broader applicability.

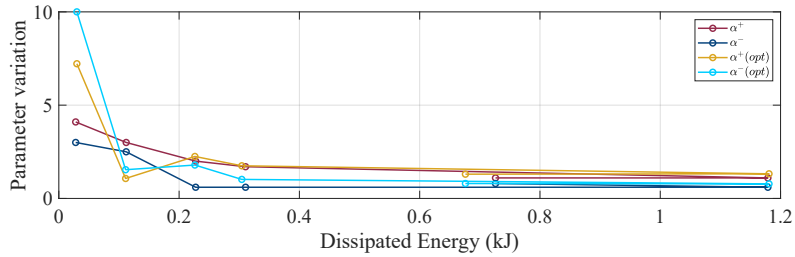


Figure 4.16. Variation of the α parameter as a function of the dissipated energy for the simulated hysteretic loop of the angle bracket (tested by Gavric et al.[30]) and the GA-optimized procedure.

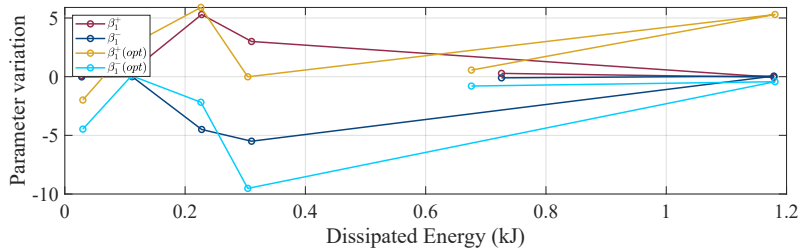


Figure 4.17. Variation of the β_1 parameter as a function of the dissipated energy for the simulated hysteretic loop of the angle bracket (tested by Gavric et al.[30]) and the GA-optimized procedure.

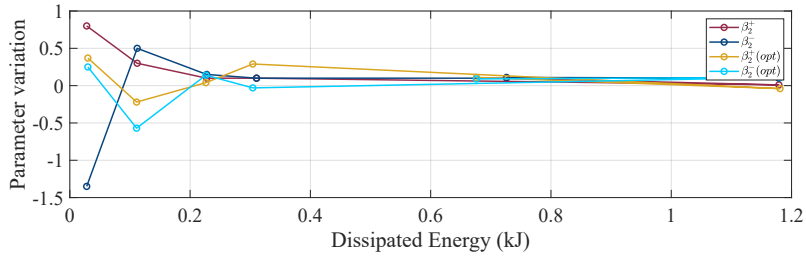


Figure 4.18. Variation of the β_2 parameter as a function of the dissipated energy for the simulated hysteretic loop of the angle bracket (tested by Gavric et al.[30]) and the GA-optimized procedure.

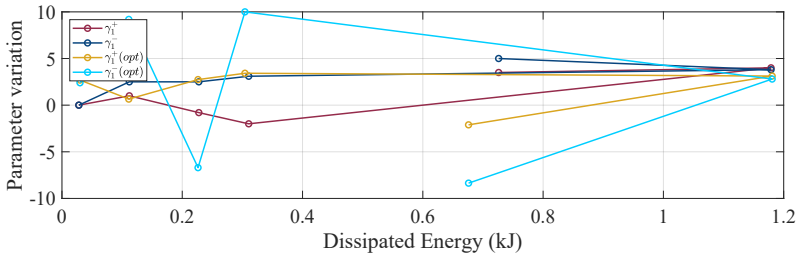


Figure 4.19. Variation of the γ_1 parameter as a function of the dissipated energy for the simulated hysteretic loop of the angle bracket (tested by Gavric et al.[30]) and the GA-optimized procedure.

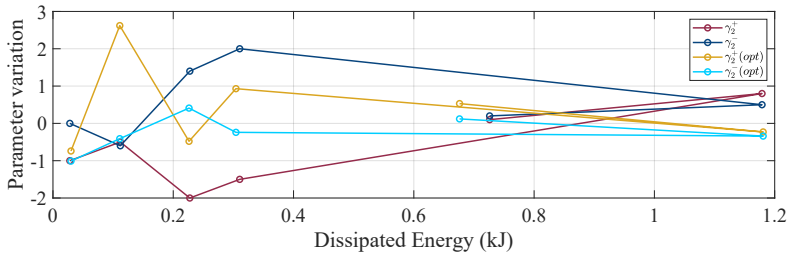


Figure 4.20. Variation of the γ_2 parameter as a function of the dissipated energy for the simulated hysteretic loop of the angle bracket (tested by Gavric et al.[30]) and the GA-optimized procedure.

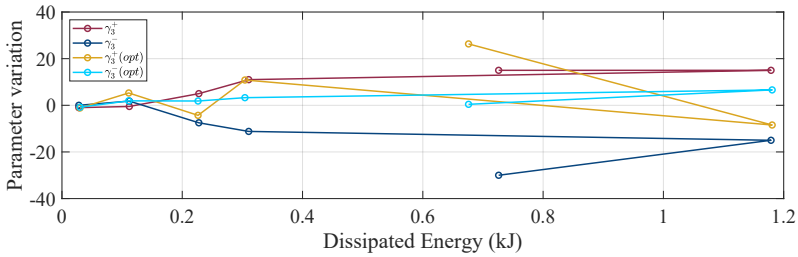


Figure 4.21. Variation of the γ_3 parameter as a function of the dissipated energy for the simulated hysteretic loop of the angle bracket (tested by Gavric et al.[30]) and the GA-optimized procedure.

Chapter 5

Dynamic Behavior of a Timber Panel

5.1 Summary of Chapter 5

Chapter 5 investigates the dynamic behavior of a Cross-Laminated Timber (CLT) panel connected to its foundation using angle brackets and hold-downs. The study relies on experimental data from controlled tests, particularly emphasizing the axial performance of hold-down connections, which are crucial for resisting uplift forces and maintaining structural stability. This work builds upon experimental research reported in [30], providing a solid basis for developing an advanced simulation model.

To capture the non-linear dynamic response of the timber panel, a mathematical model is developed that incorporates the complex hysteretic behavior of the connections. This behavior is derived from the simulated loops presented in Chapter 4. The numerical implementation is discussed comprehensively, focusing on the computational strategies employed, including time step refinement to balance simulation accuracy and computational efficiency.

For clarity and to facilitate focused analysis, the timber panel is simplified to a rigid body model with three degrees of freedom (DOFs): vertical displacement, horizontal displacement, and rotation. This assumption shifts the emphasis from the panel itself to the role of its connections in governing the system's response to dynamic loads. By adopting this simplification, the study effectively captures the critical dynamic behavior without the complexity of a fully detailed structural model.

The chapter concludes with a detailed discussion of the numerical results, analyzing key dynamic metrics such as displacement and acceleration time histories.

These results bridge the gap between experimental observations and numerical simulations, enhancing the understanding of timber structures under dynamic loading conditions.

5.2 Dynamic Behavior of a CLT panel

The sample analyzed in this Chapter is based on the experimental study conducted by Gavric et al. in [30]. Previously, in Chapters 2 and 3, we discussed the behavior of angle brackets and hold-downs, which are now applied to a Cross-Laminated Timber panel. This CLT panel has a thickness of 85 mm, is composed of five 17 mm layers, and features a square geometry measuring 2950 mm per side. The panel is anchored to a steel foundation using two hold-downs at the base corners and four internal angle brackets, referred to as HD and AB in Figure 5.1.

The structural resistance and stiffness of timber structures, especially light-frame timber systems, are generally influenced by five primary deflection modes [31]:

- slipping between the sheathing and timber frame: caused by relative movement between sheathing panels and the timber frame, significantly affecting energy dissipation and deformation in light-frame structures;
- sliding of the frame relative to the foundation: it involves lateral displacement of the entire structure relative to the base, influenced by the stiffness of connections and the structure's overall mass (Figure 5.2a);
- rigid rocking: the structure tilts or rocks about its base, typically resisted by hold-down connections under tension and compression forces (Figure 5.2b);
- shear distortion occurs within the panel itself, often resulting in a parallelogram -like shape change. This mode is common in more flexible light-frame structures where sheathing panels significantly contribute to shear resistance (Figure 5.2c);
- flexural deformation: associated with bending stresses within timber elements, contributing to overall deformation when structural components experience bending moments (Figure 5.2d).

However, research by Casagrande et al. [17] shows that the deflection behavior of CLT panels differs significantly from light-frame timber structures. Due to the high in-plane rigidity of CLT panels, the most dominant deflection modes are rigid sliding and rocking, accounting for 77 % and 16 % of the total deformation, respectively, with only 7 % attributable to panel deformation. The stiffness

and strength of CLT panels are considerably higher than their connections. This means that the overall deformation of the structure is primarily governed by the behavior of these more flexible connections. CLT panels are engineered with a cross-oriented, layered construction that makes them exceptionally stiff and resistant to in-plane deformation, bending, and shearing. In contrast, metal connections such as hold-downs and angle brackets yield or deform under loading, facilitating energy dissipation, especially under dynamic seismic forces.

Therefore, the overall structural deformation under lateral or vertical loads results more from connection behavior (e.g., slipping, sliding, and rocking) than from panel deformation. As a result, shear distortion, slipping between sheathing and frame, and flexural deformation are considered negligible. The focus on rigid sliding and rocking modes highlights the critical importance of accurately modeling connection behavior to effectively predict the dynamic performance of CLT structures.

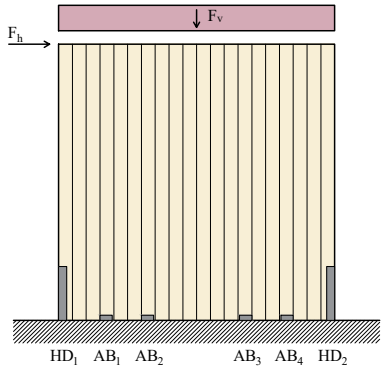


Figure 5.1. CLT Panel connected to the foundation with n.2 hold-downs and n.4 angle bracket and subjected to vertical (F_v) and horizontal (F_h) loads.

The vertical loads due to rigid rocking are typically resisted by hold-downs strategically placed at the corners of the panel to prevent uplift forces and provide stability. At the same time, angle brackets resist the shear forces resulting from the horizontal slip at the base, ensuring that the panel remains securely attached to the foundation under lateral loads, such as those induced by seismic activity or wind. The research taken as an example simplifies the approach by neglecting the axial stiffness and strength of the angle brackets, as well as the shear stiffness and strength of the hold-downs. This simplification is justified by focusing on the dominant effects that significantly influence the overall structural response. The model emphasizes the critical behaviors that govern the panel's deflection

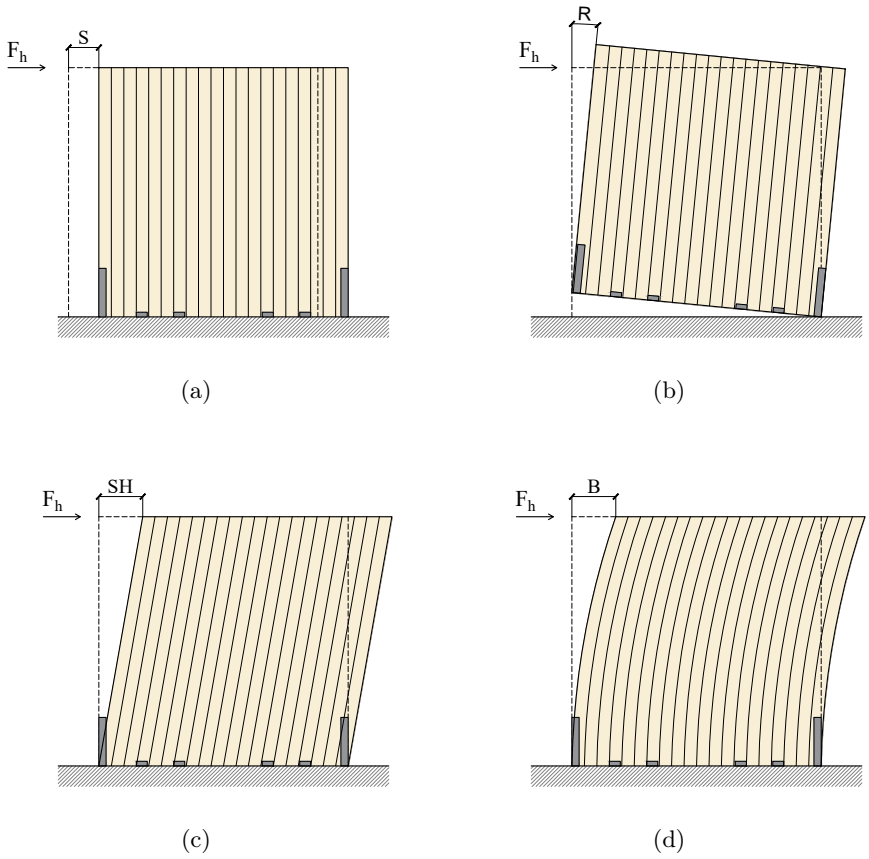


Figure 5.2. General deflection modes of a timber structure: (a) sliding, (b) rigid rocking, (c) shear distortion, and (d) flexural deformation.

and energy dissipation by omitting these components.

However, these simplifications can have potential implications. Neglecting the axial stiffness of the angle brackets and the shear strength of the hold-downs might introduce some level of inaccuracy in the simulation results. In some scenarios, the structural response could be slightly overestimated or underestimated, depending on how influential these neglected components are in reality.

5.3 Test Procedure and Experimental Data

The CLT panel considered in this study is connected to a steel beam foundation using a series of metal fasteners. Specifically, two hold-downs are anchored with 12 nails each, measuring 4x60 mm, while four angle brackets are fixed with 11 nails each, also measuring 4x60 mm. This robust fastening configuration is crucial for accurately replicating the realistic boundary conditions of timber structures in seismic events.

The loading protocol follows the cyclic test procedures outlined in EN 12512: 2001 [4], which specify parameters for assessing the behavior of timber connections under dynamic loads. The displacement input is varied in velocity, ranging from 0.4 mm/s to 0.8 mm/s, to simulate different loading rates that could occur during seismic activity. Additionally, a constant static vertical load of 18.5 kN/m is applied at the top of the panel to mimic the typical load conditions that a wall panel might experience in a real building structure.

The mechanical properties of the CLT panel, including stiffness and strength parameters, are provided following EN 12512:2001 [4]. These properties are essential for interpreting the experimental results and validating numerical models. The relevant mechanical characteristics of the panel are summarized in Table 5.1. Other characteristics necessary for computing the panel's dynamic behavior are sourced from EN 1991-1-1 [2]. These include the material's density, specified as 5 kN/m^3. Furthermore, the panel's secant stiffness, crucial for simulating its dynamic response, is calculated as the ratio of the maximum force ($F_{\max}$) to the maximum displacement ($u_{\max}$), yielding a value of 2.21 kN/mm. This stiffness parameter will be employed in the simulation of the panel's rigid body dynamics.

	Property	**Unit**	**Value**
Yield Load	F_y	[kN]	87.17
Yield Displacement	v_y	[mm]	16.96
Max Load	F_{max}	[kN]	104.21
Max Displacement	v_{max}	[mm]	47.18
Elastic stiffness	k_{el}	[kN/mm]	4.77
Plastic stiffness	k_{pl}	[kN/mm]	0.80

Table 5.1. Mechanical properties of CLT panel tested by Gavric et al. in [30].

The CLT panel in this study uses the same angle brackets and hold-downs analyzed in detail in Chapters 2 and 4. As previously discussed, these connections play a critical role in the panel's overall behavior under cyclic loading,

with their mechanical performance characterized by hysteresis loops that exhibit pinching, stiffness degradation, and energy dissipation. In Chapter 2, we investigated the experimental behavior of angle brackets and hold-downs under shear loads, analyzing their complete hysteresis loops with both positive and negative displacements. These loops provided valuable insights into the connections' energy dissipation capabilities and ductility. Subsequently, in Chapter 4, we employed the Vaiana-Rosati Model to simulate these connections' experimentally observed hysteresis behavior. As shown in Figure 4.2a-b, the resulting simulations demonstrated the model's effectiveness in capturing key features like pinching and stiffness degradation.

Considering the assumption that hold-downs react only in the axial direction, the following section will focus on the experimental behavior of the hold-downs and simulate their hysteresis loops using the VRM. These insights are crucial to the current study, as the calibrated connection characteristics and simulation results will be integrated to model the CLT panel's dynamic response accurately.

5.3.1 Hold–downs in axial direction

The geometric features of the hold-down studied are thoroughly detailed in Section 2.4.1 of Chapter 2. In this analysis, we focus on the behavior of the hold-down under axial loading conditions. As such, the loading protocol, depicted in Figure 5.3, only considers positive displacements since negative displacements are not physically realistic for axial loading scenarios.

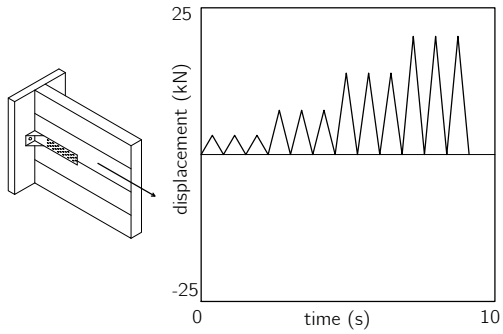


Figure 5.3. Loading protocol for axial loading on the hold-down tested by Gavric et al. in [30] and scheme of the test set-up

The experimental campaign by Gavric et al. [30] highlighted the exceptional axial resistance of the hold-down connection. The results showed that even under significant axial forces, the hold-down itself remained undamaged, while the primary signs of deformation were observed in the nails. The ultimate failure of the connection occurred due to the intense deformation of the nails, either through pulling out of the timber or bending. This demonstrates the robust performance of the hold-down in axial loading, with failure mechanisms primarily tied to the fasteners rather than the hold-down component itself. The experimental hys-

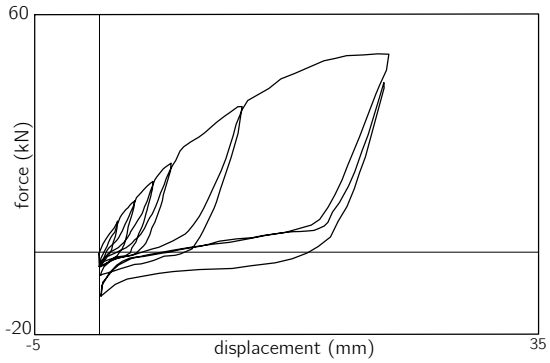


Figure 5.4. Experimental loop exhibited by the hold-down when loaded in axial direction.

teresis loop for the hold-down under axial loading is shown in Figure 5.4 and is confined to a single quadrant due to the nature of the load, which only involves positive displacements. This positioning reflects the physical constraint of axial forces that prevent the occurrence of negative displacements. From the shape of the loop, several key features emerge that indicate the typical hysteresis behavior of timber connections. Firstly, the loop's pinched shape, evident from the onset of loading, suggests significant energy dissipation mechanisms primarily governed by the deformation of the nails rather than the hold-down itself. This pinching effect is associated with reduced energy absorption efficiency, a common characteristic in timber connections due to the slippage and yielding of fasteners. As the cyclic loading continues, the stiffness of the connection decreases progressively, indicative of accumulated damage and micro-level material deterioration. This gradual stiffness degradation can be attributed to the plastic deformation of the nails and the potential localized crushing of the timber around the fastener connections. The loop also displays a mild reduction in peak strength following the

maximum displacement of 24 mm, where a force of 50 kN is reached. This slight strength degradation highlights the connection's ability to sustain high levels of axial resistance even as it nears its failure threshold. Such behavior is critical in seismic applications, where maintaining load-bearing capacity for as long as possible is vital for structural stability. The gradual decline in strength suggests a ductile failure mode, generally preferred in structural design because it provides warning signs before complete failure. Furthermore, the ultimate failure mechanism observed—characterized by nail pull-out or bending—emphasizes the role of the fasteners in the overall performance of the connection. The nails' intense deformation absorbs significant amounts of energy, contributing to the overall ductility of the system. This observation underscores the importance of nail properties and fastening techniques in connection design. Enhancements in nail strength, embedment depth, or the use of additional fasteners could improve the connection's performance by delaying stiffness degradation and extending the serviceability of the connection under high loads.

In summary, the hysteresis loop analysis reveals that the hold-down connection offers substantial resistance and energy dissipation, even as it experiences gradual degradation. These findings are crucial for understanding the connection's behavior under real-world dynamic loads, emphasizing the importance of designing robust and reliable fastener systems to enhance the performance and safety of timber structures under seismic conditions.

Calibration of the VRM on the experimental hysteresis loop

The VRM was manually calibrated to replicate the unique characteristics of the experimentally observed hysteresis loop. The primary objective was to fine-tune the model to accurately represent the pinched shape and the gradual stiffness degradation observed during cyclic loading. Figure 5.5 illustrates how the calibrated VRM closely matches the experimental data, capturing the essential features of the connection's response. Following the calibration methodology outlined in Section 4.4, an initial set of model parameters was established, as presented in Table 5.2. Figure 5.5a demonstrates that the VRM can approximate the initial cycles of displacement and force. However, the precision is limited for these early cycles, which exhibit less stability and a more irregular shape compared to subsequent cycles. This initial discrepancy is attributed to the inherent instability and variability in the loop's shape during the early stages of loading. To improve the simulation, key model parameters were adjusted to account for the observed variation in stiffness throughout the loading history. Specifically:

- k_b^-, which controls the slope of the limiting curve. Modifying it, the model can adjust the overall stiffness of the connection during the loading process;

- β_1^- and β_2^-, whom influence the curvature of the limiting curve. By varying them, the model can simulate the gradual stiffness degradation and curvature changes that occur as the loading history progresses.

By strategically adjusting these parameters in response to the dissipated energy, the VRM successfully captures the evolving stiffness and strength characteristics of the hold-down connection. This approach reflects the ongoing damage and plastic deformation occurring in the nails, as well as the slight reduction in peak strength after reaching the maximum displacement of 24 mm. In Table 5.3, parameters k_b^-, β_1^- and β_2^- are highlighted in bold to indicate their variation, which was crucial for accurately modeling the loop shape and energy dissipation.

The comparison between the experimental and simulated hysteresis loops demonstrates the VRM's capability to model the complex nonlinear behavior of timber connections under axial loads. The model effectively preserves the characteristic pinching effect and accurately reproduces the energy dissipation and strength retention observed experimentally. This result confirms the robustness and reliability of the VRM in predicting the dynamic response of timber connections, even under challenging loading conditions.

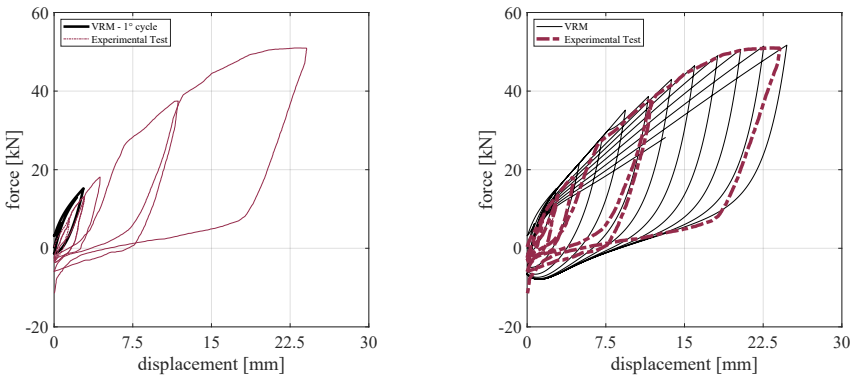


Figure 5.5. Simulation of the experimental hysteresis loop of the hold-down tested by Gavric et al. [30] in the axial direction by using the VRM: (a) first cycle and (b) complete loop.

first cycle								
s	k_b	f_0	α	β_1	β_2	γ_1	γ_2	γ_3
+	3.3	10	1.14	5.0	-0.05	-1.95	0.5	-1.53
-	0.8	5.0	0.5	10	-0.51	4.07	0.5	0.86

Table 5.2. Initial set of VRM parameters adopted for simulating the first cycles of the experimental hysteresis loops shown in Figure 5.5a

final cycle								
s	k_b	f_0	α	β_1	β_2	γ_1	γ_2	γ_3
+	**2.62**	10	1.14	**38.83**	**-0.03**	-1.95	0.5	-1.53
-	0.8	5.0	0.5	10	-0.51	4.07	0.5	0.86

Table 5.3. Final set of VRM parameters adopted for simulating the experimental hysteresis loops shown in Figures 5.5b changed as a function of the generalized work.

5.4 Mathematical Model for the Nonlinear Dynamic Analysis

This section presents a mathematical framework for analyzing the non-linear dynamic behavior of the CLT panel connected by rate-independent hysteretic elements, specifically angle brackets, and hold-downs. The model builds upon the method introduced by Vaiana and Rosati in [64], focusing on the interaction between the rigid panel and hysteretic connections to accurately describe energy dissipation and deformation mechanisms under dynamic loading conditions.

The CLT panel is idealized as a rigid body moving in two-dimensional space, as shown in Figure 5.6. It is treated as a plane object with uniform mass distribution m, where the center of mass coincides with the geometric center G.The analysis uses a right-handed Cartesian coordinate system, centered at G with axes x_1 and x_2 for translational motion and x_3 for rotation about an out-of-plane axis. The generalized coordinates that describe the panel's motion are:

- $u_1(t)$ displacement along the x_1 direction;
- $u_2(t)$ displacement along the x_2 direction;
- $\theta(t)$ rotation about the x_3

These coordinates form the basis for a dynamic analysis that includes external forces and moments acting on the panel as well as internal forces from the hysteretic connections.

The panel's mass properties, including its mass and moment of inertia, are derived from its polygonal geometry. Specifically, the mass moment of inertia about x_3 axis, denoted J_{x_3}, is essential for analyzing rotational effects under dynamic loading:

$$J_{x_3} = \frac{m}{A}(I_{x_1} + I_{x_2}), \tag{5.1}$$

where A is the area of the polygonal body, I_{x_1} and I_{x_2} are the area moments of inertia about the x_1 and x_2 axes, respectively. They are given by:

$$I_{x_1} = \int_A y^2 \, \mathrm{d}A, \tag{5.2}$$

$$I_{x_2} = \int_A x^2 \, \mathrm{d}A, \tag{5.3}$$

where: x and y are the distances from the centroid of the area A to each differential area element $\mathrm{d}A$ along the x_2 and x_1 directions, respectively.

These properties establish the foundational mass and inertia values needed to assess the panel's resistance to translational and rotational motion during seismic loading.

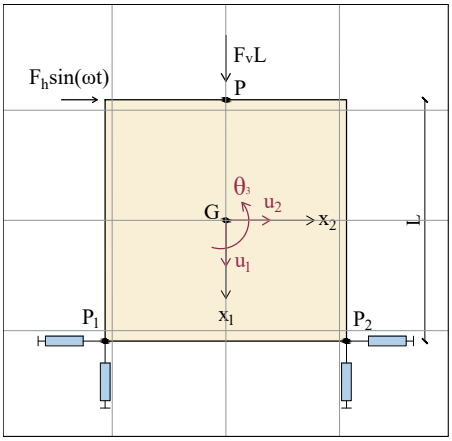


Figure 5.6. Mathematical Model with selected generalized coordinates.

The four angle brackets and two hold-downs at the base points P_1 and P_2 are modeled as rate-independent hysteresis springs that respond to the relative

movement between the CLT panel and its foundation. To compute the dynamic response of these connections, we calculate the displacement of each base point relative to the center of mass G of the rigid panel. Under the assumption of small displacements, the displacement components of each base point relative to the coordinates of G are given by:

$$\begin{aligned} u_1^{P_i} &= u_1 - \theta x_2^{P_i}, \\ u_2^{P_i} &= u_2 + \theta x_1^{P_i}, \end{aligned} \tag{5.4}$$

where u_1 and u_2 are the displacements of G along the x_1 and x_2 axes, respectively, θ is the rotation about the x_3 axis and $x_1^{P_i}$ and $x_2^{P_i}$ are the coordinates of the base point P_i relative to G.

A set of second-order, non-linear ordinary differential equations governs the dynamic equilibrium of the CLT panel. These equations account for the generalized inertial forces $(f_i)_1$, $(f_i)_2$, $(m_i)_3$, generalized hysteretic forces from the connections $(f_{ri})_1^{P_1}$, $(f_{ri})_2^{P_1}$, $(f_{ri})_1^{P_2}$, $(f_{ri})_2^{P_2}$, and any generalized external loads, p_1, p_2, m_3, applied to the panel in point P. By imposing the conditions of equilibrium to the rigid body at the generic time t, we have the dynamic system's equation set, which is:

$$\begin{aligned} p_1(t) =& (f_i)_1(t) + (f_{ri})_1^{P_1}(t) + (f_{ri})_1^{P_2}(t) \\ p_2(t) =& (f_i)_2(t) + (f_{ri})_2^{P_1}(t) + (f_{ri})_2^{P_2}(t) \\ p_3(t) =& (m_i)_3(t) - (f_{ri})_1^{P_1}(t)x_2^1 - (f_{ri})_1^{P_2}(t)x_2^2 \\ &+ (f_{ri})_2^{P_1}(t)x_1^1 + (f_{ri})_2^{P_2}(t)x_2^1 \end{aligned} \tag{5.5}$$

where the inertial forces are:

$$\begin{aligned} (f_i)_1(t) =& m\ddot{u}_1(t) \\ (f_i)_2(t) =& m\ddot{u}_2(t) \\ (m_i)_3(t) =& J_{x_3}\ddot{\theta}_3 \end{aligned} \tag{5.6}$$

and

$$p_3(t) = m_3(t) - p_1(t)x_2^P + p_2(t)x_1^P \tag{5.7}$$

5.4.1 Numerical implementation

The non-linear dynamic behavior of the CLT panel connected by hysteretic springs under combined vertical and horizontal loading was simulated using MATLAB R2023a. The numerical implementation leverages a non-linear time history analysis (NLTHA) approach, capturing the interaction of the dynamic loads and the hysteretic response of the connections. Table 5.4 outlines the systematic

steps involved in the algorithm to perform the NLTHA, including initialization of parameters, iterative solution for the equations of motion, and evaluation of the forces and displacements at each time step. This method ensures an accurate representation of the dynamic response, accounting for the rate-dependent and rate-independent hysteretic effects of the springs.

To represent the dynamic behavior of the connections, VRM was implemented for each connection, allowing hold-downs to be simulated as axial springs and angle brackets as shear springs. In particular, the axial springs that model the hold-downs are constrained to avoid unrealistic positive displacements at the base. Thus, the model implements a condition in which downward movement at the base significantly increases spring stiffness, preventing the panel from lifting off the foundation. In the MATLAB code, this constraint is implemented by dynamically adjusting the axial spring stiffness based on the current displacement values, following the scheme in 5.7:

- if the vertical displacement at a base point ($u_1^{P_1}$ or $u_1^{P_2}$) is positive, the spring's stiffness, k_e, is set to a value 100 times its initial elastic stiffness, effectively preventing downward movement;
- if the displacement is negative, indicating tension, the spring stiffness returns to zero, activating the spring's hysteresis behavior in the tension direction.

.

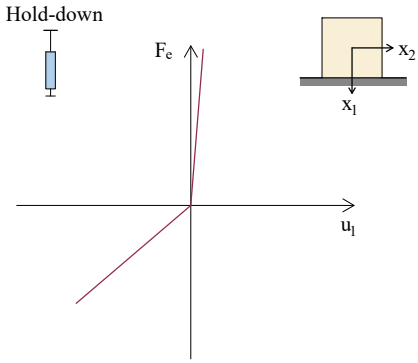


Figure 5.7. Scheme of elastic stiffness variation in hold-downs according to the displacement sign, where the elastic force is $F_e = k_e u_1$, with k_e elastic stiffness.

Step	Description
1. Initialization	Define system properties (dimensions, material properties, Mass, Mass Moment of inertia, etc) and time step Δt
2. System Matrices	Compute mass, damping, and stiffness matrices (M, C, K) using input parameters. Damping and stiffness are initialized with zeros and later updated dynamically.
3. Force Inputs	Define vertical and horizontal forces: • Vertical load: Constant value. • Horizontal load: Sinusoidal force with increasing amplitude.
4. Initial Conditions	Initialize displacements (u_0), velocities ($\dot{u}_0$), accelerations ($\ddot{u}_0$), stiffness and damping matrix (C_0, K_0).
5. CEM	Set $\alpha = 1/4$ and $\beta = 1/2$ and compute S_0 [5.9].
6. VRM	Define parameters for hold-downs and angle brackets based on experimental hysteresis loops.
7. Time-Step Loop	For each time step: • Compute displacements and velocities at each connection point. • Update stiffness matrix dynamically based on current displacement. • Compute hysteresis forces and work. • Update acceleration, velocity, and displacement using Chang's explicit method [5.10].
8. Finalization	Store results (e.g., displacements, forces, and work) for analysis and visualization.

Table 5.4. Flowchart with steps for implementing the NLTH of a CLT panel with hysteretic connections under combined vertical and horizontal loading.

This study employs the Chang explicit method (CEM) to solve the equations of motion for the CLT panel. The Chang method is an explicit time integration technique suitable for non-linear dynamic analysis due to its straightforward formulation and computational efficiency [19, 20, 38]. Using the extension range of validity formulated in [67], the CEM allows for accurate tracking of dynamic responses in systems with complex behaviors, such as those involving hysteretic damping and non-linear stiffness in timber connections. The Chang Explicit Method uses explicit time integration, which means that the solution for the system's state at the next time step depends only on the current state and does not involve solving large systems of simultaneous equations, as in implicit methods. This characteristic makes it highly efficient for large-scale problems where rapid computation of each time step is essential. Moreover, because it is an explicit method, it inherently maintains stability over small time steps, making it well-suited for the fine time discretization needed to capture the non-linear behavior of timber connections under dynamic loading.

The CEM approach formulates the system's dynamics using mass (M), damping (C), and stiffness (K) matrices alongside forces terms: rate-dependent f_{rdn}, rate-independent f_{ri}, elastic f_{en} and external p.

$$Ma_i + Cv_i + Kd_i + (f_{rdn})_i + (f_{ri})_i + (f_{en})_i = p_i \tag{5.8}$$

In this case of study, rate-dependent and elastic forces are null, whereas only rate-independent and external forces are present.

The integration starts with initial setup calculations, where the mass matrix M, damping matrix C, and stiffness matrix K are defined along with initial displacement d_0 and velocity v_0 vectors. From these, the initial acceleration vector a_0 is computed. Using two scalar parameters, which are related to the properties of stability and accuracy, $\alpha = 1/4$ and $\beta = 1/2$, the matrix S_0 is defined as:

$$S_0 = M + \beta \Delta t C_0 + \alpha (\Delta t)^2 K_0 \tag{5.9}$$

where S_0 simplifies the integration by remaining constant and only requiring inversion once at the beginning of the analysis time steps, which involve updating displacement, velocity, and acceleration at each i time step. They are computed as follows:

$$\begin{aligned} d_{i+1} &= d_i + \Delta t v_i + S_0^{-1} \left(M(\Delta t)^2 a_i + \alpha (\Delta t)^2 \left(p_{i+1} - p_i \right) \right) \\ v_{i+1} &= v_i + S_0^{-1} M (\Delta t) a_i \\ a_{i+1} &= M^{-1} [p_{i+1} - C v_{i+1} - K u_{i+1} - (f_{ri})_{i+1}] \end{aligned} \tag{5.10}$$

The method's accuracy allows us to find a solution result close enough to

the exact solution, and it depends on the size of the time step (Δt). A smaller time step improves accuracy by better capturing dynamic changes in the system. However, too small a step size increases computational cost without significant gains if (Δt) is already sufficiently small. Like most explicit methods, CEM is conditionally stable, meaning stability depends on the choice of the time step (Δt). If it is too large, the solution can diverge. To have a stable solution, the time step must be smaller than the critical time step (Δt_{cr}). It is related to the natural period of the j-th mode at the $(i+1)$-th time step and can be computed as follows:

$$(\Delta t)_{i+1} \leq (\Delta t_{cr})_{i+1}^{(j)} = \begin{cases} \infty & \text{if } \alpha \geq \frac{1}{4}\left(\beta + \frac{1}{2}\right)^2 \kappa_{i+1}^{(j)}, \\ \frac{T_0^{(j)}}{2\pi\sqrt{\frac{1}{4}\kappa_{i+1}^{(j)} - \alpha}} & \text{if } \alpha < \frac{1}{4}\left(\beta + \frac{1}{2}\right)^2 \kappa_{i+1}^{(j)}. \end{cases} \tag{5.11}$$

where $\kappa_{i+1}^{(j)}$ is the current degree of nonlinearity of the j-th mode at the $(i+1)$-th time step of a NLTHA, computed as:

$$\kappa_{i+1}^{(j)} = \left[\frac{T_0^{(j)}}{T_{i+1}^{(j)}}\right]^2 \tag{5.12}$$

in which T_0 is the initial natural period of the j-th mode, and T_{i+1} is the natural period of the j-th mode at the $(i+1)$-th time step of a NLTHA. In particular, $\kappa_{i+1}^{(j)}$ can take different values depending on the typology of the mechanical system:

- $\kappa_{i+1}^{(j)} < 1$ if the system is with non-stiffening hysteretic behavior;
- $\kappa_{i+1}^{(j)} = 1$ if the system is with linear elastic behavior;
- $\kappa_{i+1}^{(j)} > 1$ if the system is with stiffening hysteretic behavior.

Initial Setup of System Matrices

The mass matrix (M) represents the distribution of the panel's mass and accounts for the inertial forces when subjected to dynamic loads. Given that the panel is modeled as a rigid body, M is diagonal, with entries corresponding to translational and rotational inertial properties. In this case, M (5.13) contains the panel's mass (m)) and the moment of inertia (J_{x_3}) about its center of mass.

$$M = \begin{bmatrix} m & 0 & 0 \\ 0 & m & 0 \\ 0 & 0 & J_{x_3} \end{bmatrix} \tag{5.13}$$

The damping matrix (C) accounts for energy dissipation through the material's internal friction and the connections (angle brackets and hold-downs). Often, this matrix is proportional to M and K, typically set up as $C = a_0M + a_1K$ following the Rayleigh relation [22] to approximate realistic damping while simplifying computations. In this case, the elements of C, used in expressions 5.14 and 5.15, are determined based on damping coefficients, where c_{1P_1} and c_{1P_2} correspond to hold-downs at base points P_1 and P_2 in the vertical direction (x_1), while c_{2P_1} and c_{2P_2} correspond to angle brackets at the same points P_1 and P_2 in the horizontal direction (x_2). Additionally, x_{1P_1} and x_{1P_2} denote the vertical coordinates of the base points, whereas x_{2P_1} and x_{2P_2} refer to their horizontal coordinates. Moreover, damping coefficients c_1 and c_2 are null in this specific case.

$$C = \begin{bmatrix} C_{11} & C_{12} & C_{13} \\ C_{21} & C_{22} & C_{23} \\ C_{31} & C_{32} & C_{33} \end{bmatrix} \tag{5.14}$$

where:

$$\begin{aligned}
C_{11} &= 2c_{1P1} + 2c_{1P2} \\
C_{12} &= 0 \\
C_{13} &= -2c_{1P1}x_{2P1} - 2c_{1P2}x_{2P2} \\
C_{21} &= 0 \\
C_{22} &= 2c_{2P1} + 2c_{2P2} \\
C_{23} &= 2c_{2P1}x_{1P1} + 2c_{2P2}x_{1P2} \\
C_{31} &= -2c_{1P1}x_{2P1} - 2c_{1P2}x_{2P2} \\
C_{32} &= 2c_{2P1}x_{1P1} + 2c_{2P2}x_{1P2} \\
C_{33} &= 2c_{1P1}x_{2P1}^2 + 2c_{1P2}x_{2P2}^2 + 2c_{2P1}x_{1P1}^2 + 2c_{2P2}x_{1P2}^2
\end{aligned} \tag{5.15}$$

The stiffness matrix (K) defines the system's resistance to deformation under applied loads. For the timber panel, K reflects the connection stiffness, which depends on factors like the geometry and material properties of angle brackets and hold-downs. The elements of K, shown in expressions 5.16 and 5.17, are formulated using stiffness values. In particular, k_{e1P_1} and k_{e1P_2} represent the stiffness of hold-downs at base points P_1 and P_2 in the vertical direction, while k_{e2P_1} and k_{e2P_2} indicate the stiffness of angle brackets in the horizontal direction. Similar to the damping matrix, the vertical coordinates of the base points are denoted by x_1P_1 and x_1P_2, whereas their horizontal counterparts are represented by x_2P_1 and x_2P_2. Since the analysis involves non-linear behavior, the stiffness matrix is dynamically updated to account for variations due to the hysteretic response of the connections, ensuring that the model accurately reflects the me-

chanical behavior of the timber panel under dynamic loading. In this case, the parameters k_{e1} and k_{e2} are set as the secant stiffness of the CLT panel, defined in Paragraph 5.4.

$$K = \begin{bmatrix} K_{11} & K_{12} & K_{13} \\ K_{21} & K_{22} & K_{23} \\ K_{31} & K_{32} & K_{33} \end{bmatrix} \tag{5.16}$$

where:

$$\begin{aligned} K_{11} &= 2k_{e1P1} + 2k_{e1P2} \\ K_{12} &= 0 \\ K_{13} &= -2k_{e1P1}x_{2P1} - 2k_{e1P2}x_{2P2} \\ K_{21} &= 0 \\ K_{22} &= 2k_{e2P1} + 2k_{e2P2} \\ K_{23} &= 2k_{e2P1}x_{1P1} + 2k_{e2P2}x_{1P2} \\ K_{13} &= -2k_{e1P1}x_{2P1} - 2k_{e1P2}x_{2P2} \\ K_{23} &= 2k_{e2P1}x_{1P1} + 2k_{e2P2}x_{1P2} \\ K_{33} &= 2k_{e1P1}x_{2P1}^2 + 2k_{e1P2}x_{2P2}^2 + 2k_{e2P1}x_{1P1}^2 + 2k_{e2P2}x_{1P2}^2 \end{aligned} \tag{5.17}$$

Applied generalized external forces

The vector of external forces p comprises a vertical force along x_1 direction, a horizontal force along x_2 direction, and rotational freedom along θ_3. Two external forces are applied to the first two degrees of freedom to replicate the CLT panel's experimental conditions. As illustrated in Figure 5.8, the vertical force remains constant at 54.58 kN, simulating a static gravitational or equivalent vertical load acting on the panel. Meanwhile, the horizontal force is sinusoidal with linearly increasing amplitude, designed to reach up to 340 kN. This amplitude is approximately three times the maximum displacement recorded for the panel (as detailed in Table 5.1). The sinusoidal force has a pulsation of $\omega = 2\pi$ rad/s, corresponding to a frequency of 1 Hz, and the time duration of the numerical tests is $t_{max} = 10$s.

For this NTHA, the time step is selected as small, equal to 0.0001 seconds, to satisfy stability requirements, which are influenced by the CLT panel's natural frequency and the connections' stiffness. Using a small time increment ensures that the Chang method remains stable and accurately models the panel's dynamic response.

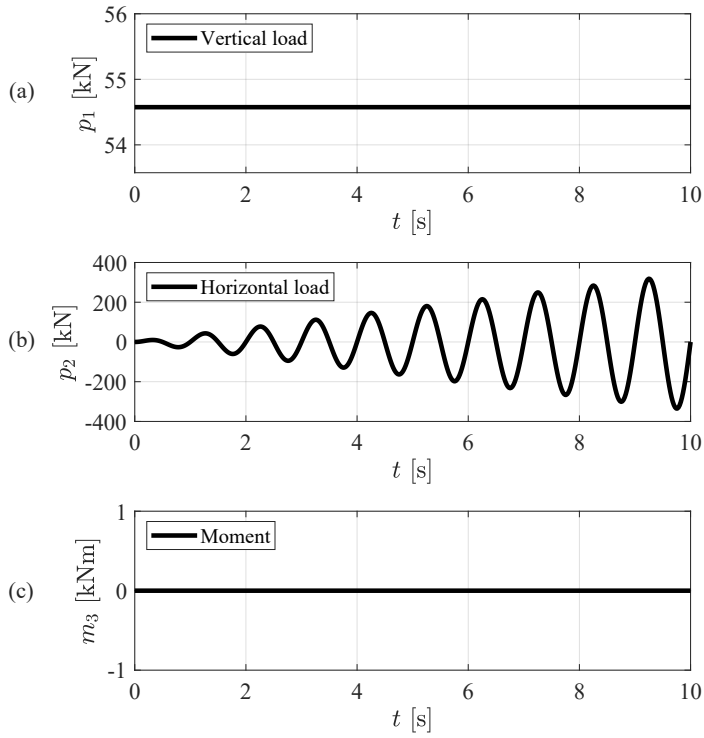


Figure 5.8. Applied generalized external forces for the three degrees of freedom: (a) constant load along x_1, (b) harmonic force with increasing amplitude along x_2, and (c) null rotation along θ_3.

Hysteretic Behavior of the Timber Panel

The dynamic response of the four angle brackets and two hold-downs is captured using the VRM as part of the non-linear dynamic analysis, with separate parameter sets characterizing the two connection types. The initial and final sets of model parameters used in the code were already tabled in Tables 4.1a and 4.2a for simulating angle brackets, and in Tables 5.2 and 5.3 for simulating the hold-downs. The graphs of hysteresis loops related to the springs located at the base points of the panel are illustrated in Figures 5.9. Comparing these simulations in the global dynamic analysis with the simulations related to the single connections (Figures 5.5- 4.2a), the loops show a slightly different shape, even though the total dissipated energy in the two cases is the same, and the

variation of model parameters follows the same linear relationships as functions of the dissipated energy.

These differences in loop shapes can be attributed to several factors, including the panel's displacement history, the multidirectional loading regime, and the combined response of multiple connections. In the global analysis, the displacement history reflects more complex loading patterns compared to isolated connection tests, influenced by the coexistence of vertical and horizontal forces. The multidirectional loading regime leads to intricate stress-strain paths in the connections, while the interaction of hold-downs and angle brackets creates more complex energy dissipation patterns than those observed in isolated scenarios. In fact, by comparing the dissipated energy W_{ri} in the springs at points P_1 and P_2 with the energy recorded in the isolated connection simulated test, as illustrated in Figure 5.10, it is evident that the energy reaches approximately the same values within ten seconds of the simulation. The energy trends show consistent growth over time, but the pathways differ slightly, reflecting the influence of the more complex loading conditions in the dynamic analysis. This observation underlines the importance of accounting for dynamic interactions between connections and the panel.

Despite these differences, the principal features of the loops are preserved:

- maximum forces and displacements are reached;
- the pinched shape characteristic of the hysteresis loops is maintained;
- inflection points in the loading and unloading curves shift particularly for angle brackets (Figures 5.9b).

The global hysteresis behavior of the timber panel is analyzed by considering the contributions of the four angle brackets and two hold-downs. The simulated hysteresis loops, derived using the VRM, are compared with the experimental loops under two conditions: axial displacement (governed by the hold-downs) and shear displacement (dominated by the angle brackets). The comparisons are illustrated in Figures 5.11. The objective of the simulation is to replicate the main features of the experimental hysteresis loop. In the reference study by Gavric et al. [30], the analytical simulation primarily focused on predicting the backbone curve rather than the full hysteresis loop. By contrast, the VRM-based simulation in this study aims to capture both the backbone curve and the detailed loop shape.

For the hold-downs (Figure 5.11a), the simulation achieves the predictions for the maximum displacement and force, as well as the overall trend of the secant stiffness during loading and unloading cycles. However, the detailed shape of the simulated loop does not match the experimental loop. This discrepancy may stem from neglected cross-contributions from the angle brackets. Research findings indicate that under axial loads, the four angle brackets contribute approximately

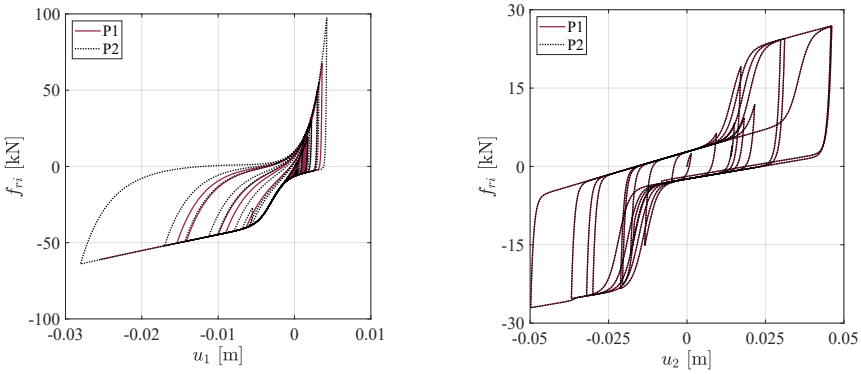


Figure 5.9. Hysteretic Forces at P_1 and P_2 base points: (a) in hold-downs (axial direction) and (b) angle brackets (shear direction).

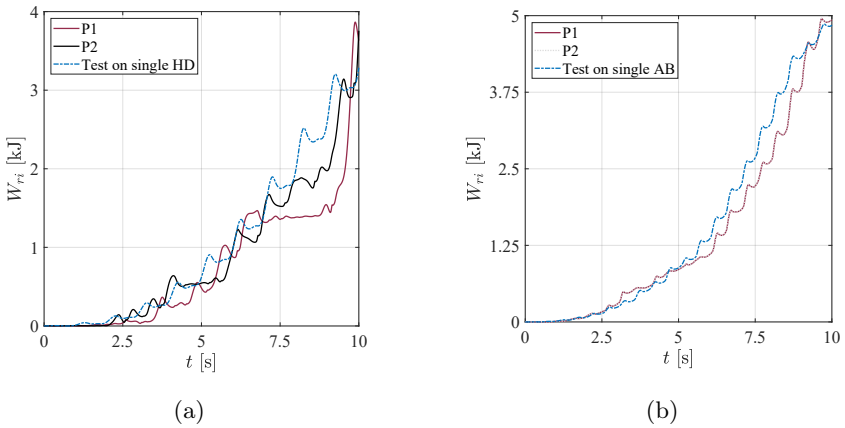


Figure 5.10. Comparison of dissipated energy in hysteresis springs in points P_1 and P_2, with tests on single connections: (a) the case of hold-downs (HD), and (b) the case of angle brackets (AB).

50% of the resistance compared to the two hold-downs. This significant contribution is not explicitly modeled in the current analysis, which may partially explain

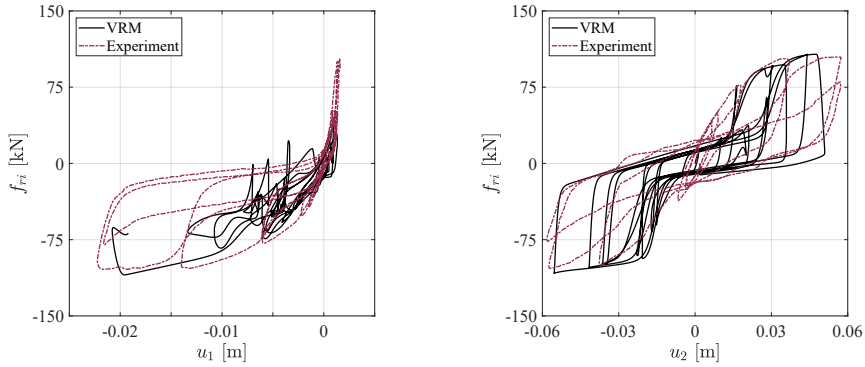


Figure 5.11. Total Hysteretic Force in the System: (a) axial direction (hold-downs), and (b) shear direction (angle brackets). Comparison between the experimental hysteresis loops and the analytical prediction using the VRM.

the mismatch in the loop shape.

Whereas, in the case of angle brackets (Figure 5.11b), the simulation more closely reproduces the global hysteresis loop shape observed in experiments. In particular, the key features captured include the pinched loop shape due to energy dissipation, the gradual shifting of the limiting curves during loading and unloading cycles, and the approximation to maximum displacement and force. However, the global loop shape is not as perfectly reproduced as in the isolated single-connection tests. This discrepancy may be influenced by the neglected contribution of hold-downs in resisting shear displacements. Research suggests that the angle brackets dominate the response under shear loads, contributing 93% of the resistance, with only 7% attributed to the hold-downs. The current model does not account for this distribution of load-sharing, which can impact the accuracy of the simulation.

In summary, the deviations between simulated and experimental loops can be attributed to several factors:

- the system complexity, in fact, the global behavior results from the combined action of multiple connections, which interact in non-linear ways that are challenging to capture in a simplified model;
- the simplified assumption made to model the panel; in fact, it is modeled as a rigid body with deformation limited to shifting and rigid rocking,

neglecting the shear and bending deformation;

- the simulation does not account for the contributions of angle brackets in resisting axial displacements or hold-downs in resisting shear displacements, which can influence the overall behavior.

5.5 Results of Numerical Analysis and Discussion

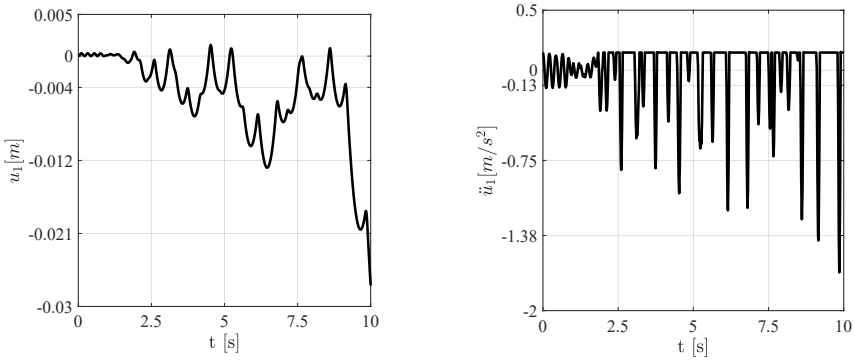
The results of the non-linear dynamic analysis of the timber panel are evaluated through displacement and acceleration responses, energy dissipation, deformation modes, numerical performance, and considerations for real-world implications.

Displacement and Acceleration Responses

The results of the non-linear dynamic analysis of the timber panel are evaluated through displacement and acceleration responses, energy dissipation, deformation modes, numerical performance, and considerations for real-world implications.

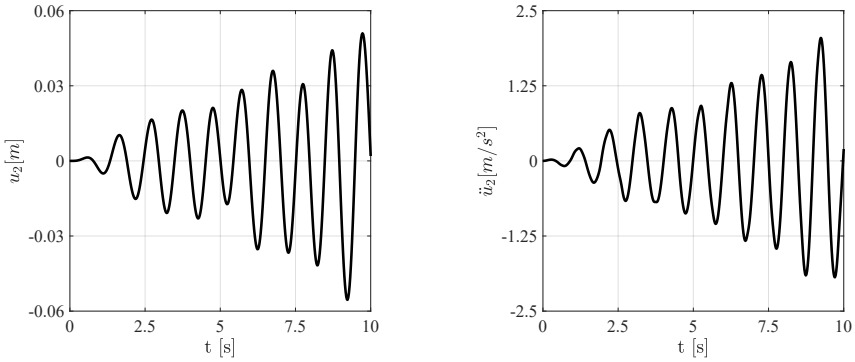
The displacement responses at the Center of Mass are presented in Figures 5.12-5.13-5.14. A predominant horizontal displacement u_2 along the x_2 direction (Figure 5.13b) is observed, with the panel reaching approximately 50 mm in the left and right directions. In comparison, the vertical displacement, u_1 (Figure 5.13a), is significantly smaller, reaching a maximum of only 1.5 mm, consistent with the panel's primary response to horizontal loads. The rotation θ_3 (Figure 5.14) reveals the rocking behavior of the panel. A distinct opposition between the peaks of θ_3 and u_1 is evident, attributed to the coupled translational and rotational dynamics of the rigid-body system. This opposition occurs because the rotation induces vertical displacements at the base points, constrained by the hold-downs. When the panel rotates, one side experiences an upward displacement that is resisted by the restoring force of the hold-downs, while the opposite side undergoes a downward displacement. This interaction blocks upward motion and enhances the restoring forces' overall contribution, ensuring system stability.

The displacement responses at the base points P_1 and P_2, illustrated in Figure 5.15, further corroborate the observations at the center of mass. For the horizontal displacements u_2 in Figures 5.15c-d, both points move synchronously in the same direction, reflecting the sinusoidal nature of the applied external force with increasing amplitude. The maximum horizontal displacement at the base points closely mirrors the sinusoidal input, demonstrating the consistency of the panel's overall rigid-body motion. In contrast, the vertical displacements u_1, shown in Figures 5.15a-b, exhibit distinct asymmetry between points P_1 and P_2. In fact,



(a) (b)

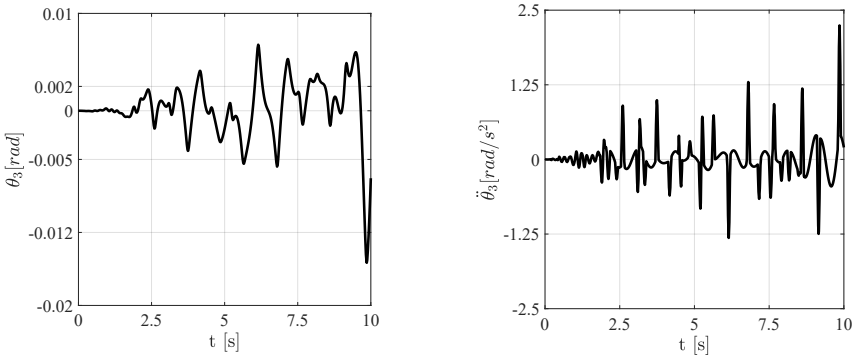
Figure 5.12. Time history of the (a) displacement u_1 and (b) acceleration $\ddot{u}_1$ related to the Center of Gravity along direction x_1.



(a) (b)

Figure 5.13. Time history of the (a) displacement u_2 and (b) acceleration $\ddot{u}_2$ related to the Center of Gravity along direction x_2.

point P_1 achieves the maximum downward displacement of approximately 42 mm, compared to 28 mm for P_2. However, positive vertical displacements (downward motion) remain small, generally staying below 4 mm. This behavior is indicative of localized effects caused by the interaction between the applied loads, the rota-



(a) (b)

Figure 5.14. Time history of the (a) rotation θ_3 and (b) rotational acceleration $\ddot{\theta}_3$ related to the Center of Gravity about x_3 axis.

tional dynamics, and the resistance provided by the connections at the base.

The acceleration responses are fundamental in understanding the dynamic performance and inertial forces experienced by the timber panel. The time histories of accelerations at the Center of Mass reveal key system behavior characteristics under non-linear dynamic loading. The horizontal acceleration component $\ddot{u}_2$ (Figure 5.13b) is observed to dominate, corresponding to the sinusoidal input force applied in the horizontal direction. The peaks in horizontal acceleration align with changes in the external force's amplitude and frequency, indicating a strong inertial response to the input excitation, with a maximum acceleration value of 2.05 m/s^2. In contrast, the vertical acceleration $\ddot{u}_1$ (Figure 5.12b) exhibits smaller amplitudes, with a maximum of 1.68 m/s^2, reflecting the limited vertical displacement responses due to the constraints imposed by the hold-downs and the predominant horizontal load. The rotational acceleration $\ddot{\theta}_3$ (Figure 5.14b) mirrors the rocking motion of the panel, with peaks occurring during transitions between the leftward and rightward motions.

The interplay between rotational and translational accelerations highlights the coupled nature of the system's dynamics. For example, as the rotational acceleration $\ddot{\theta}_3$ increases, the vertical acceleration $\ddot{u}_1$ at the base points increases due to the reaction forces from the hold-downs resisting upward motion.

The acceleration time histories provide insights into the system's stability. The absence of irregular or exponentially growing peaks confirms that the system remains dynamically stable under the imposed loading conditions. This is

particularly important for validating the effectiveness of the connections (hold-downs and angle brackets) in controlling the motion.

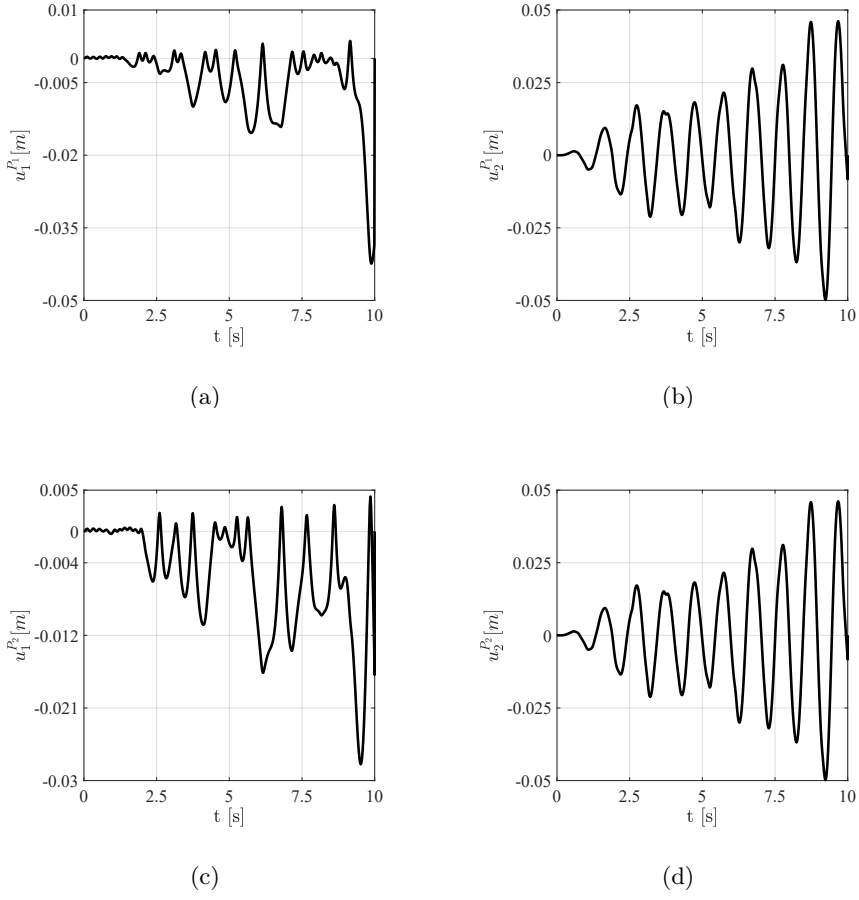


Figure 5.15. Time history of displacement at the base points P_1 and P_2: (a) $u_1^{P_1}$ displacement of point P_1 along x_1 direction, (b) $u_2^{P_1}$ displacement of point P_1 along x_2 direction, (c) $u_1^{P_2}$ displacement of point P_2 along x_1 direction, and (d) $u_2^{P_2}$ displacement of point P_2 along x_2 direction.

Numerical Accuracy of the Chang Explicit Method

To ensure the accuracy of the Chang Explicit Method in the conducted NLTHA, the time history of displacement u_1, u_2, and rotation θ_3 are computed considering different time steps Δt: 0.01 s, 0.001 s, and 0.0001 s. Figure 5.16 shows the results with different colors and highlights the different accuracy of the analysis. In fact:

- for larger time steps ($\Delta t = 0.01$ s), the displacement response in red deviates significantly from the smaller time steps, particularly during high dynamic activity, as evident after 7.5 seconds, reaching at the end of the analysis 150 mm of vertical displacement u_1, 120 mm of horizontal displacement u_2, and -0.06 rad of rotation θ_3. This deviation demonstrates reduced accuracy and potential numerical instability;
- at intermediate time steps ($\Delta t = 0.001$ s), the response in blue aligns more closely with the smallest time step, indicating reasonable accuracy;
- the smallest time step ($\Delta t = 0.0001$ s) provides the most accurate results, considered as the benchmark for stable dynamic behavior.

The choice of the time step (Δt) in the numerical analysis significantly impacts both the accuracy of the results and the computational resources required. A comparison of the global hysteresis loops for $\Delta t = 0.001$ s and $\Delta t = 0.0001$ s, as illustrated in Figure 5.17, highlights several effects. Using $\Delta t = 0.001$ s, the simulation results diverge noticeably from the experimental data, especially in the case of hysteresis loop representative of the axial displacement u_1 in Figure 5.17a, where the simulated loop deviates from the experimental secant stiffness trend. Moreover, the model underestimates the maximum displacement and force. Similarly, in the case of the hysteresis loop representative of lateral displacement u_2, the simulation does not accurately capture the maximum force and displacement, although the global shape is reproduced.

By contrast, adopting $\Delta t = 0.0001$ s enhances the accuracy of the simulation. The global hysteresis loops align much more closely with the experimental data, accurately reproducing the maximum force and displacement values, as well as the secant stiffness trend during the time history.

While smaller time steps improve the accuracy, they significantly increase computational demands, as shown in Table 5.5. In fact, the largest time step requires only 0.20 s of total computational time, but the results are highly inaccurate; the intermediate time step strikes a balance between accuracy and efficiency, taking 1.24 s but still falling short in reproducing the experimental loops accurately; finally, the smallest time step achieves the highest fidelity but at a computational cost of 11.10 s, approximately 55 times greater than $\Delta t = 0.01$ s. The trade-off between accuracy and efficiency becomes evident from these results.

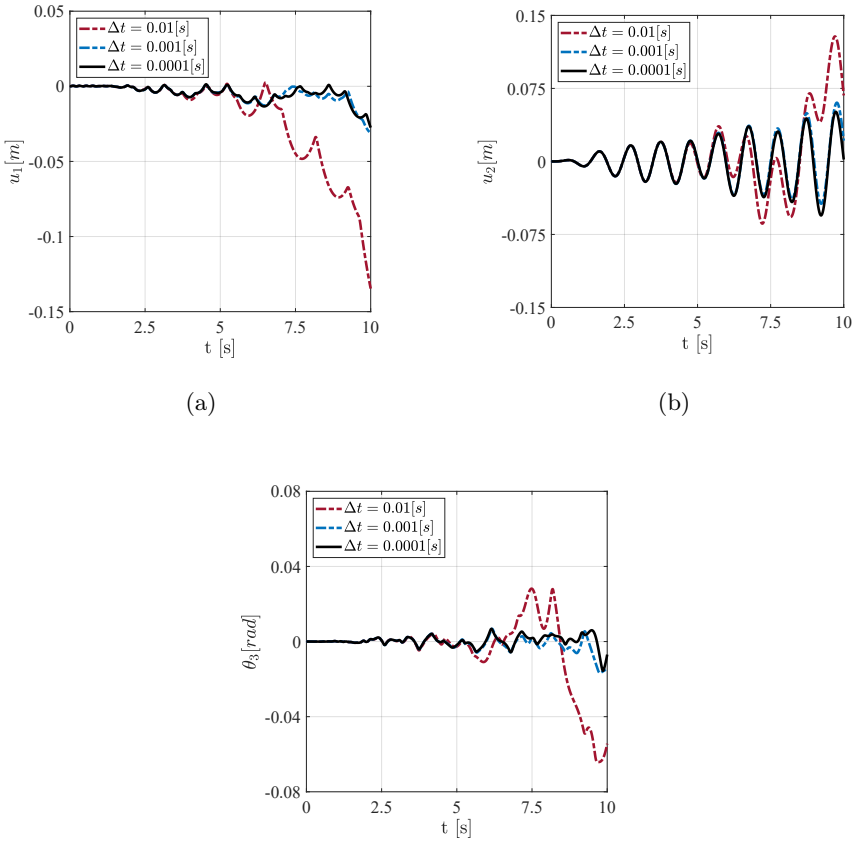
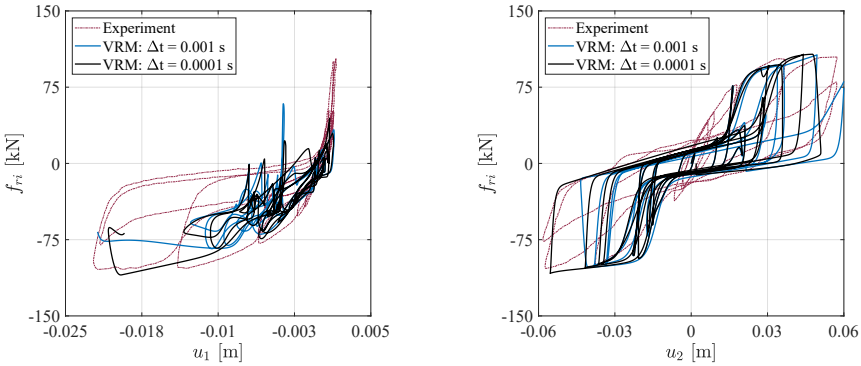


Figure 5.16. Accuracy of Chang explicit method as a function of the time step chosen: $\Delta t = 0.01 - 0.001 - 0.0001$ s in (a) displacement u_1, (b) displacement u_2, and (c) rotation θ_3 recorder at the center of mass G.

While smaller time steps are necessary for precision in dynamic systems with intricate non-linearities, they must be weighed against the increased computational cost. In this case, given the relatively moderate complexity of the algorithm, the smallest time step ($\Delta t = 0.0001$ s) is a practical choice that ensures high accuracy without prohibitive computational costs.



(a) (b)

Figure 5.17. Accuracy of Chang explicit method as a function of the time step chosen: $\Delta t = 0.001 - 0.0001s$ in computing the Hysteretic Force (a) with axial displacements u_1 (hold-downs), and (b) lateral displacements u_2 (angle brackets).

	$\Delta t = 0.01$ s	$\Delta t = 0.001$ s	$\Delta t = 0.0001$ s
Tot. computational time [s]	0.1987	1.2361	11.1040

Table 5.5. Computational time required to make the NLTHA with different time steps.

5.6 Practical Implications of the Study

The findings from this study have several practical implications, particularly for the design, analysis, and construction of timber structures subjected to dynamic loading, such as those in seismic-prone areas. The detailed investigation into the dynamic behavior of the timber panel highlights the critical role of connections, such as hold-downs and angle brackets, in governing the overall performance of timber structures. This study's results provide actionable insights for optimizing connection designs to improve energy dissipation and enhance the structural stability of timber buildings during earthquakes. Specifically, the calibrated hysteretic behavior of connections can be used to design safer and more resilient structures by focusing on parameters such as ductility, stiffness, and peak force capacity.

Developing and validating a robust non-linear dynamic model for timber panels offer significant advancements in seismic design codes. Engineers can better predict how timber structures behave under varying dynamic loads by incorporating detailed hysteresis behavior and realistic deformation modes. This helps bridge the gap between theoretical predictions and real-world performance, contributing to safer and more efficient building designs.

The trade-off analysis between accuracy and computational cost provides practical guidance for engineers using numerical simulations. For projects where high precision is critical, such as when designing structures in regions with high seismic risk, the use of smaller time steps ensures better agreement with experimental data. Conversely, for preliminary analyses or simpler systems, larger time steps may be acceptable to reduce computational time without significantly compromising accuracy. This flexibility allows engineers to balance computational demands with project-specific requirements.

The observed coupling between translational and rotational dynamics (rocking behavior) has implications for structural design. For example, understanding how vertical displacements u_1 and rotations θ_3 interact allows engineers to better anticipate and mitigate localized stress concentrations at connections. This is particularly important for tall or slender timber walls, where rocking can amplify loads on certain connections.

The calibration of numerical models against experimental data ensures the applicability of the findings to real-world structures. By achieving close alignment with experimental results, the model can be used for advanced simulations of larger or more complex timber systems, providing engineers with tools to evaluate performance under a variety of dynamic scenarios, including earthquakes, wind loads, and human-induced vibrations.

The hysteretic loops analyzed in this study demonstrate how timber connections dissipate energy during cyclic loading. This is particularly relevant for seismic design, as enhanced energy dissipation and ductility reduce the risk of catastrophic failure. The insights gained can inform design strategies to maximize energy absorption while preventing excessive deformation or damage to the structure.

The integration of experimental data with numerical modeling establishes a framework for future studies and practical applications. This study highlights the importance of validating numerical simulations against real-world tests to ensure reliability. Engineers can use similar validation techniques to evaluate novel connection designs, alternative timber materials, or hybrid structural systems.

Timber structures are increasingly valued for their sustainability. This study enhances the viability of timber as a material for dynamic applications by proving its ability to perform under seismic conditions. By optimizing connections and providing reliable models, the study supports the broader adoption of timber in

resilient, eco-friendly construction.

In summary, this research not only improves the theoretical understanding of timber panel behavior under dynamic loads but also provides practical tools and insights for structural engineers. It enhances the resilience of timber structures, reduces uncertainties in design, and supports sustainable building practices, making timber a more viable choice for modern construction in seismic regions.

5.7 Conclusions of Chapter 5

Chapter 5 examined the dynamic behavior of a CLT panel connected to the foundation using hold-downs and angle brackets. The analysis began with experimental tests on isolated connections obtained from the scientific literature. The panel was modeled as a rigid body, with axial and horizontal hysteresis springs governed by the VRM. A non-linear dynamic analysis was performed using the Chang explicit method, and the results were evaluated in terms of relative displacements, accelerations, and hysteretic forces, considering various levels of numerical accuracy.

The advantages and limitations of this approach were highlighted by comparing the experimental hysteresis loops with the simulated ones. While the simplified modeling of panel deformation modes and the absence of cross-collaboration effects between connections reduced the complexity of the hysteretic loops, the trend of the secant stiffness, along with the maximum displacement and force values, was effectively captured.

Due to a lack of experimental data, evaluating additional behaviors, such as the panel's response to different loading scenarios was impossible. Nevertheless, this study validates the use of the VRM in simulating non-linear dynamics, demonstrating its potential for predicting the behavior of complex systems. This approach provides a foundation for future research and practical applications in timber structures under dynamic loading.

Chapter 6

Conclusions

This thesis has conducted a comprehensive investigation into the dynamic behavior of timber structures, focusing on their performance under dynamic scenarios such as earthquakes. Addressing the complexities of timber connections advances analytical and numerical tools for designing and optimizing timber structures in seismic regions.

After reviewing the typologies of timber structures in the building industry, the study categorized common connection types and analyzed their hysteresis loops. Timber connections exhibit unique hysteretic behaviors characterized by significant pinching, force, and stiffness degradation. These features are critical for evaluating energy dissipation during dynamic events. As required by design standards [1, 5], these connections act as the weak link, ensuring energy dissipation while protecting the overall structure.

To simulate hysteresis loops and improve connection design, the thesis evaluated existing hysteretic models, including the Bouc-Wen [12, 13, 70, 10, 9, 11] and Dolan models [25], highlighting calibration challenges such as parameter complexity and difficulty reproducing asymmetric loops with pronounced pinching. The Vaiana-Rosati Model (VRM) [65, 67, 66, 68, 61] was adopted in analytical and differential forms to address these issues. With two sets of eight geometrically meaningful parameters, the VRM successfully simulated experimental hysteresis loops of angle brackets, hold-downs, beam-to-pillar connections, and shear wall connections. By varying parameters as a function of dissipated energy, the VRM captured the global connection behavior, though the need for intermediate cycles introduced discrepancies in energy dissipation counts.

Parameter calibration was enhanced using optimization techniques, comparing the local *fminsearch* algorithm and the global genetic algorithm. While *fminsearch* offered speed by focusing on local parameter spaces, the genetic algorithm provided more robust solutions at a higher computational cost. The latter was

ultimately preferred for improving VRM calibration and sensitivity analysis, enhancing the fidelity of simulations.

The study extended to a Cross-Laminated Timber (CLT) panel connected with angle brackets and hold-downs, referencing experimental data from Gavric et al. [30]. The panel was modeled as a rigid body with sliding and rocking deformation modes, excluding shear and bending effects based on findings in [17]. Dynamic analysis of the CLT panel using the Chang explicit method offered insights into coupled translational and rotational dynamics under lateral and vertical loads. The VRM effectively predicted maximum displacements and forces, demonstrating its utility in forecasting timber structure behavior.

Issues and Future Objectives

The findings of this thesis point to several challenges and opportunities for future research and development in modeling timber structures and their connections.

The current version of the VRM, while effective in capturing the hysteretic behavior of timber connections, faces limitations in addressing certain phenomena. Future improvements could include:

- force degradation modeling: introducing specific functions or terms to account explicitly for force and stiffness degradation. This would enable the model to simulate the gradual reduction in connection strength observed in real structures over repeated loading cycles;
- multi-variable parameter variation: developing an analytical formulation to simultaneously vary model parameters as a function of both work (energy dissipation) and displacement. This would allow the model to adapt dynamically to varying loading histories, such as those seen in real earthquakes or irregular dynamic events, improving robustness and applicability;
- parameter automatic identification: implementing algorithms to automatically adjust parameters for individual cycles and for entire hysteretic loops. This would account for loop shape and behavior changes without requiring manual recalibration, significantly improving efficiency and usability in practical design scenarios. Incorporating the capability to simulate automatically entire loading histories rather than focusing solely on single cycles would provide a more comprehensive understanding of connection behavior over prolonged dynamic events.

While this thesis focused on individual connections and simplified panel systems, future research could integrate these findings into larger-scale structural systems and investigate how the behavior of individual connections influences

the global dynamic response of multi-story timber buildings. Moreover, the analytical model could take into account the couple interactions between deformation modes (sliding, rocking, bending, shear) and resisting forces in connections, as well as the influence of moisture, temperature, and aging on their performance. Finally, real-time monitoring data and machine learning techniques should be incorporated into the VRM to enable adaptive simulations that provide immediate insights into the structure's performance under varying conditions.

One of the most critical challenges identified is the lack of sufficient experimental data on timber connections in the scientific literature. Conducting more experimental tests on connections under varying loading histories (e.g., cyclic loads with different amplitudes, frequencies, or directions, random forces, or earthquake accelerations) would provide richer datasets for better calibration of the VRM and improve its generalizability to real-world scenarios.

The current design methods and standards simplify or idealize the behavior of timber structures, which may lead to inaccuracies in predicting their performance. For instance, using a single parameter like the *q-factor* to represent ductility does not account for the detailed behavior of different connections and loading scenarios, potentially resulting in overly conservative or unsafe designs. Similarly, Johansen's theory [37], which assumes linear elastic behavior for timber, fails to capture its nonlinear, anisotropic nature and complex failure mechanisms. These oversimplifications may underestimate deformation capacity and energy dissipation in timber structures. To address these gaps, more accurate analytical methods are needed to reflect better the ductility, energy dissipation, and failure modes of timber structures. Such methods would enable safer and more efficient designs, reducing the risk of structural damage and enhancing occupant safety during extreme events like earthquakes.

By improving the VRM, refining optimization techniques, expanding experimental datasets, and integrating findings into larger structural systems, researchers and practitioners can design timber structures that are safer, more efficient, and more resilient to dynamic events. These advancements would position timber as a competitive and sustainable material in the modern construction industry, aligning with global goals for reducing environmental impact and improving seismic resilience.

Bibliography

[1] *Eurocode 5: Design of timber structures. Part 1-1: General - Common rules and rules for buildings.* CEN, European Committee for Standardization, 1995, 1995.

[2] *EN 1991-1-1:2002. Eurocode 1: Actions on structures - Part 1-1: General actions - Densities, self-weight, imposed loads for buildings.* CEN, European Committee for Standardization, Brussels, Belgium, 2002.

[3] *ISO16670:2003. Timber structures - Joints made with mechanical fasteners - Quasi-static reversed-cyclic test method.* ISO, International Organization for Standardization, 2003.

[4] *EN 12512:2001/A1:2005. Timber Structures - Test methods - Cyclic testing of joints made with mechanical fasteners.* CEN, European Committee for Standardization, Brussels, Belgium, 2005.

[5] *Norme Tecniche per le Costruzioni.* D.M. 17.01.2018, 2018.

[6] *ASTM (2019). ASTM E2126: Standard test methods for cyclic (reversed) load test for shear resistance of vertical elements of the lateral force resisting systems for buildings.* ASTM Int'l, PA, USA, 2019.

[7] N. Ajavakom, C.H. Ng, and F. Ma. Performance of nonlinear degrading structures: Identification, validation, and prediction. *Computers & Structures*, 86(7-8):652–662, 2008.

[8] A. Aloisio, M. M. Rosso, A. Iqbal, and M. Fragiacomo. Hysteresis modeling of timber-based structural systems using a combined data and model-driven approach. *Computers & Structures*, 269:106830, 2022.

[9] T. Baber and M.N. Noori. Random vibration of degrading pinching systems. *Journal of Engineering Mechanics, ASCE*, 111(8):1010–1026, 1985.

[10] T. Baber and Y. K. Wen. Random vibration of hysteretic, degrading systems. *Journal of the Engineering Mechanics Division*, 107(6):1069–1087, 1981.

[11] T. Baber and Y. K. Wen. Modeling general hysteresis behavior and random vibration application. *Journal of Vibration, Acoustics, Stress, and Reliability in Design, ASME*, 108:411–420, 1986.

[12] R. Bouc. Forced vibration of mechanical systems with hysteresis. In *Proceedings of the Fourth Conference on Nonlinear Oscillation*, page 315, Prague, Czechoslovakia, 1967.

[13] R. Bouc. Modèle mathématique d'hystérésis: application aux systèmes à un degré de liberté. *Acustica*, 24:16–25, 1971.

[14] D.E. Breyer, K. J. Fridley, K. E. Cooben, and D. G. Pollock. *Design of Wood Structures-ASD/LRFD*. McGraw-Hill New York, NY, 2007.

[15] A. H. Buchanan. *Timber design guide*. New Zealand Timber Industry Federation, 2007.

[16] J. Cao, H. Xiong, F.L. Zhangb, L. Chen, and C.R. Cazadora. Bayesian model selection for the nonlinear hysteretic model of clt connections. *Engineering Structures*, 223:111118, 2020.

[17] D. Casagrande, S. Rossi, T. Sartori, and R. Tomasi. Proposal of an analytical procedure and a simplified numerical model for elastic response of single-storey timber shear-walls. *Construction and Building Materials*, 102:1101–1112, 2016.

[18] A. Ceccotti. Connessioni nelle strutture di legno soggette ad azioni sismiche. *Manuale del legno strutturale, Mancosu Editore Press, Italy (Italian version)*, 1995.

[19] SY Chang. A new family of explicit methods for linear structural dynamics. *Computers & Structures*, 88(11-12):755–772, 2010.

[20] SY Chang. Family of structure-dependent explicit methods for structural dynamics. *Journal of Engineering Mechanics*, 140(6):06014005, 2014.

[21] United Nations. Climate Change. The paris agreement. what is the paris agreement? https://unfccc.int/process-and-meetings/the-paris-agreement, accessed 22 Nov. 2024.

[22] AK Chopra. *Dynamics of structures*. Pearson Prentice Hall, 2002.

[23] World Green Building Council. Bringing embodied carbon upfront. worldgbc.org/advancing-net-zero/embodied-carbon, Accessed 10 May 2024.

[24] D.M.D. da Silva, S.M. Avila, M.V.G de Morais, and A.A. Cavallini Jr. Comparing optimization algorithms for parameter identification of sigmoid model for mr damper. *Journal of the Brazilian Society of Mechanical Sciences and Engineering*, 46(3):134, 2024.

[25] J. D. Dolan. *The dynamic response of timber shear walls*. PhD thesis, University of British Columbia, 1989.

[26] H. Dong, M. He, X. Wang, C. Christopoulos, Z. Li, and Z. Shu. Development of a uniaxial hysteretic model for dowel-type timber joints in opensees. *Construction and Building Materials*, 288:123112, 2021.

[27] Commissione Europea. Il green deal europeo. ec.europa.eu/commission/presscorner/detail/it/ip$_1$9$_6$691, accessed 22 Nov. 2024.

[28] R. H. Fairweather. Beam column connections for multi-storey timber buildings. Master's thesis, University of Canterbury, 1992.

[29] PLP Folhento, M. Braz-César, and R. Barros. Cyclic response of a reinforced concrete frame: Comparison of experimental results with different hysteretic models. *AIMS Materials Science*, 8(6):917–931, 2021.

[30] I. Gavric, A. Ceccotti, and M. Fragiacomo. Experimental cyclic tests on cross-laminated timber panels and typical connections. 2011.

[31] I. Gavric, M. Fragiacomo, and A. Ceccotti. Cyclic behavior of clt wall systems: Experimental tests and analytical prediction models. *Journal of structural engineering*, 141(11):04015034, 2015.

[32] L. De Giovanni. *Metodi e Modelli per l'Ottimizzazione Combinatoria. Metodi euristici di ottimizzazione combinatoria*. Università di Padova, 2014.

[33] ZK Gurgi, AI Ismael, and RA Mejeed. The comparing between genetic algorithm and neural network to compute of three-basic solar cell parameters with wide range of measured temperature. *Journal of Operation and Automation in Power Engineering*, 12(2):134–141, 2024.

[34] V. Hassani, T. Tjahjowidodo, and T. Nho Do. A survey on hysteresis modeling, identification and control. *Mechanical Systems and Signal Processing*, 49(1):209–233, 2014.

[35] W. Hawkins, S. Cooper, S. Allen, J. Roynon, and T. Ibell. Embodied carbon assessment using a dynamic climate model: Case-study comparison of a concrete, steel and timber building structure. *Structures*, 33:90–98, 2021.

[36] K. Jiang, J. Wen, Q. Han, and X. Du. Identification of nonlinear hysteretic systems using sequence model-based optimization. *Structural Control and Health Monitoring*, 27(4):e2500, 2020.

[37] K.W. Johansen. Theory of timber connections. *International Assoc. of Bridge and Structural Engineering Publication*, 9:249–262, 1949.

[38] C. Kolay and JM Ricles. Assessment of explicit and semi-explicit classes of model-based algorithms for direct integration in structural dynamics. *International Journal for Numerical Methods in Engineering*, 107(1):49–73, 2016.

[39] B. Li, X. Yang, J. Yang, Y. Zhang, and Z. Ma. Optimization algorithm comparison for in-plane flexible ring tire model parameter identification. In *International Design Engineering Technical Conferences and Computers and Information in Engineering Conference*, volume 50138, page V003T01A024. American Society of Mechanical Engineers, 2016.

[40] Z. Li, X. Wang, and M. He. Experimental and analytical investigations into lateral performance of cross-laminated timber (clt) shear walls with different construction methods. *Journal of Earthquake Engineering*, 26(7):3724–3746, 2022.

[41] H. Lim. *Performance of strand-based wood composite post-and-beam shear wall system*. PhD thesis, University of British Columbia, 2016.

[42] N. Malleson. Calibration of simulation models. *Encyclopedia of Criminology & Criminal Justice*, 40:115–118, 2014.

[43] J.RRA Martins and A. Ning. *Engineering design optimization*. Cambridge University Press, 2021.

[44] J.A. Nelder and R. Mead. A simplex method for function minimization. *The computer journal*, 7(4):308–313, 1965.

[45] MP Newcombe, S. Pampanin, A. Buchanan, and A. Palermo. Section analysis and cyclic behavior of post-tensioned jointed ductile connections for

multi-story timber buildings. *Journal of Earthquake Engineering*, 12(S1):83–110, 2008.

[46] United Nations. Department of Economic and Social Affairs. Sustainable Development. The 17 goals, sustainable development. sdgs.un.org/goals, accessed 22 Nov. 2024.

[47] S. Pei, J.W. van De Lindt, M. Popovski, J.W. Berman, J.D. Dolan, J. Ricles, R. Sause, H. Blomgren, and D.R. Rammer. Cross-laminated timber for seismic regions: Progress and challenges for research and implementation. *Journal of Structural Engineering*, 142(4):E2514001, 2016.

[48] M. Pelliciari, B. Briseghella, F. Tondolo, L. Veneziano, C. Nuti, R. Greco, D. Lavorato, and AM Tarantino. A degrading bouc–wen model for the hysteresis of reinforced concrete structural elements. *Structure and Infrastructure Engineering*, 16(7):917–930, 2020.

[49] M. Pelliciari, GC Marano, T. Cuoghi, B. Briseghella, D. Lavorato, and AM Tarantino. Parameter identification of degrading and pinched hysteretic systems using a modified bouc–wen model. *Structure and Infrastructure Engineering*, 14(12):1573–1585, 2018.

[50] M. Piazza, R. Modena, and R. Tomasi. *Strutture in legno. Materiale, calcolo e progetto secondo le nuove normative europee.* Hoepli Editore, 2005.

[51] P. Pintos. In'cube danone research innovation center / arte charpentier. ArchDaily, 25 June 2023. www.archdaily.com/1002837/incube-danone-research-and-innovation-center-arte-charpentier, Accessed 18 Sept. 2024.

[52] A. Polastri. *Caratterizzazione del comportamento di giunti semirigidi per strutture lignee in zona sismica.* PhD thesis, Università degli studi di Trento, 2010.

[53] J. Porteous and A. Kermani. *Structural timber design to Eurocode 5.* John Wiley & Sons, 2008.

[54] C. Prieto. Primeiro arranha-céu de madeira da américa latina em construção na patagônia chilena. ArchDaily Brasil, 5 Dec. 2022. www.archdaily.com.br/br/992894/primeiro-arranha-ceu-de-madeira-na-america-latina-e-construido-na-patagonia-chilena, Accessed 15 Sept. 2024.

[55] RDocumentation. Fminsearch: Computation of the unconstrained minimum of given function with the nelder-mead algorithm. www.rdocumentation.org/packages/neldermead/versions/1.0-12/topics/fminsearch, Accessed 10 May 2024.

[56] G. Rinaldin, C. Amadio, and M. Fragiacomo. A component approach for the hysteretic behaviour of connections in cross-laminated wooden structures. *Earthquake engineering & structural dynamics*, 42(13):2023–2042, 2013.

[57] Leonard E Schwer. Guide for verification and validation in computational solid mechanics. In *20th International Conference on Structural Mechanics in Reactor Technology, SMiRT 20: Book of abstracts*, 2009.

[58] Tender. Building a log home – 4 important last steps, 9 May 2018. www.nordicloghome.com/log-house/, Accessed 15 Sept. 2024.

[59] T.G. Trucano, L.P. Swiler, T. Igusa, W.L. Oberkampf, and M. Pilch. Calibration, validation, and sensitivity analysis: What's what. *Reliability Engineering System Safety*, 91(10):1331–1357, 2006. The Fourth International Conference on Sensitivity Analysis of Model Output (SAMO 2004).

[60] N. Vaiana, R. Capuano, and L. Rosati. Evaluation of path-dependent work and internal energy change for hysteretic mechanical systems. *Mechanical Systems and Signal Processing*, 186:109862, 2023.

[61] N. Vaiana, R. Capuano, S. Sessa, F. Marmo, and L. Rosati. Nonlinear dynamic analysis of seismically base-isolated structures by a novel opensees hysteretic material model. *Applied Sciences*, 11(3):900, 2021.

[62] N. Vaiana and L. Rosati. Analytical and differential reformulations of the vaiana–rosati model for complex rate-independent mechanical hysteresis phenomena. *Mechanical Systems and Signal Processing*, 199:110448, 2023.

[63] N. Vaiana and L. Rosati. Classification and unified phenomenological modeling of complex uniaxial rate-independent hysteretic responses. *Mechanical Systems and Signal Processing*, 182:109539, 2023.

[64] N. Vaiana and L. Rosati. Nonlinear dynamic analysis of rigid bodies supported by rate-independent hysteretic elements. In *Proceedings of the 9th International Conference on Computational Methods in Structural Dynamics and Earthquake Engineering*, pages 2050–2061, 2023.

[65] N. Vaiana, S. Sessa, F. Marmo, and L. Rosati. A class of uniaxial phenomenological models for simulating hysteretic phenomena in rate-independent mechanical systems and materials. *Nonlinear Dynamics*, 93:1647–1669, 2018.

[66] N. Vaiana, S. Sessa, F. Marmo, and L. Rosati. An accurate and computationally efficient uniaxial phenomenological model for steel and fiber reinforced elastomeric bearings. *Composite Structures*, 211:196–212, 2019.

[67] N. Vaiana, S. Sessa, F. Marmo, and L. Rosati. Nonlinear dynamic analysis of hysteretic mechanical systems by combining a novel rate-independent model and an explicit time integration method. *Nonlinear Dynamics*, 98:2879–2901, 2019.

[68] N. Vaiana, S. Sessa, and L. Rosati. A generalized class of uniaxial rate-independent models for simulating asymmetric mechanical hysteresis phenomena. *Mechanical Systems and Signal Processing*, 146:106984, 2021.

[69] K. Wei and Z. Xu. Hysteretic model and parameter identification of rc bridge piers based on a new modified bouc-wen model. In *Structures*, volume 43, pages 1766–1777. Elsevier, 2022.

[70] Y. K. Wen. Method for random vibration of hysteretic systems. *Journal of Engineering Mechanics, American Society of Civil Engineers*, 102(2):249–263, 1976.

[71] Vermont Timber Works. Texas barn. www.vermonttimberworks.com/our-work/post-and-beam-barns/party-equipment-barn/, Accessed 28 Sept. 2024.

[72] J. Q. Yang, S. T. Smith, Z. Wang, P. Feng, and N. Sirach. Modelling of hysteresis behaviour of moment-resisting timber joints strengthened with frp composites. *International Journal of Mechanical Sciences*, 179:105593, 2020.

[73] G. Zhu, M. Zhou, J. Song, J. Wang, and X. Zhao. Parameter identification of hysteretic model of uhpc-connected precast segmental columns under cyclic loading. *Structures*, 58:105614, 2023.

Author's publications

1. A. Spedicato, N. Vaiana, and L. Rosati. Simulation of the hysteretic behavior of timber connections by the Vaiana-Rosati Model: Preliminary results, *Proceedings of the 9th International Conference on Computational Methods in Structural Dynamics and Earthquake Engineering*, 2062–2069, 2023, DOI: 10.7712/120123.10542.21131.

2. A. Spedicato, N. Vaiana, and L. Rosati. Preliminary Classification and Modeling of the Hysteretic Behavior of Connections in Timber Structures, *Computational Mechanics and Applied Mathematics: Perspectives from Young Scholars - GIMC SIMAI Young 2024* [Manuscript submitted for publication], 2025.